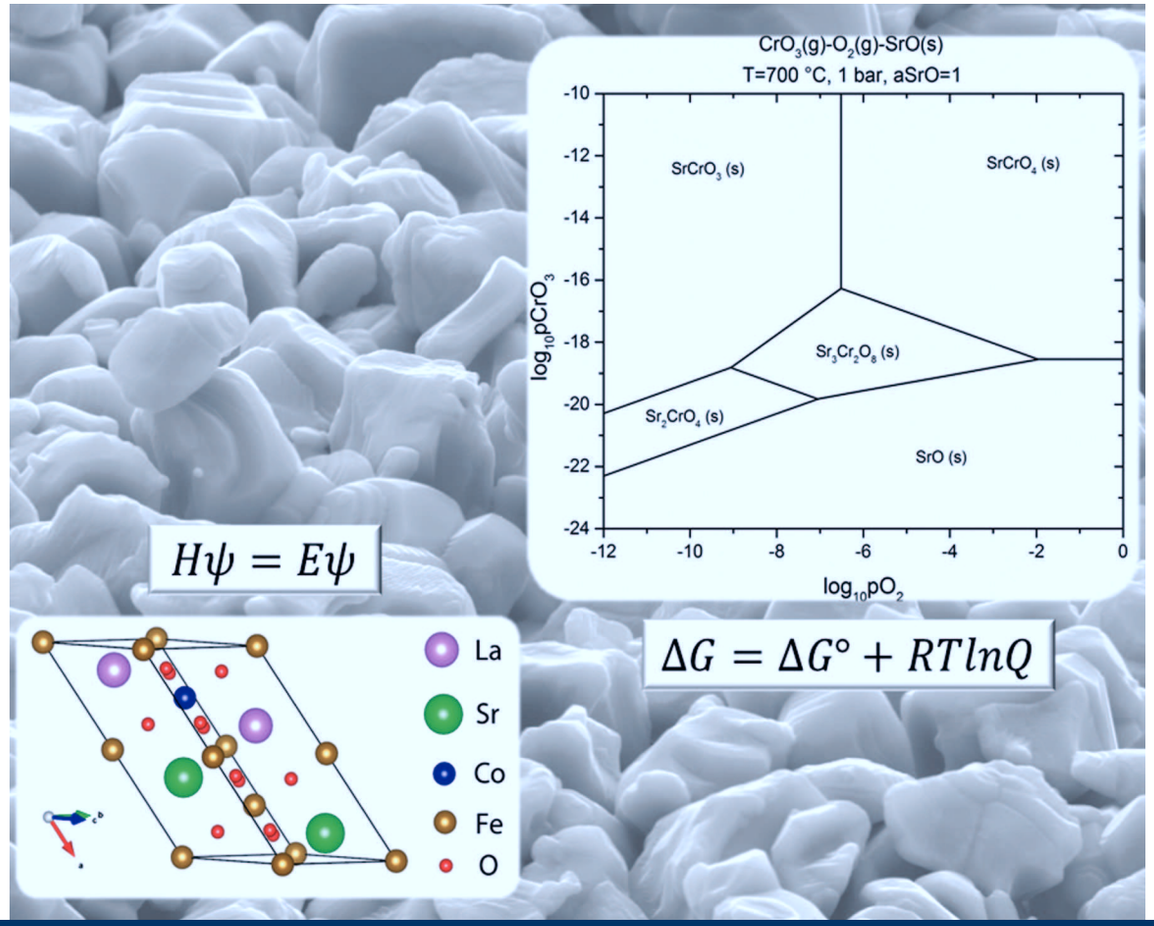

Aging and Degradation Behavior of Electrode Materials in Solid Oxide Fuel Cells (SOFCs)

Xiaoyan Yin

Energie & Umwelt / Energy & Environment
Band / Volume 446
ISBN 978-3-95806-374-7

Mitglied der Helmholtz-Gemeinschaft

JÜLICH
Forschungszentrum

Schriften des Forschungszentrums Jülich
Reihe Energie & Umwelt / Energy & Environment Band / Volume 446

Forschungszentrum Jülich GmbH
Institut für Energie- und Klimaforschung
Werkstoffstruktur und -eigenschaften (IEK-2)

Aging and Degradation Behavior of Electrode Materials in Solid Oxide Fuel Cells (SOFCs)

Xiaoyan Yin

Schriften des Forschungszentrums Jülich
Reihe Energie & Umwelt / Energy & Environment Band / Volume 446

ISSN 1866-1793 ISBN 978-3-95806-374-7

Bibliografische Information der Deutschen Nationalbibliothek.
Die Deutsche Nationalbibliothek verzeichnet diese Publikation in der Deutschen Nationalbibliografie; detaillierte Bibliografische Daten sind im Internet über http://dnb.d-nb.de abrufbar.

Herausgeber und Vertrieb:	Forschungszentrum Jülich GmbH Zentralbibliothek, Verlag 52425 Jülich Tel.: +49 2461 61-5368 Fax: +49 2461 61-6103 zb-publikation@fz-juelich.de www.fz-juelich.de/zb
Umschlaggestaltung:	Grafische Medien, Forschungszentrum Jülich GmbH
Druck:	Grafische Medien, Forschungszentrum Jülich GmbH
Copyright:	Forschungszentrum Jülich 2018

Schriften des Forschungszentrums Jülich
Reihe Energie & Umwelt / Energy & Environment, Band / Volume 446

D 82 (Diss., RWTH Aachen University, 2018)

ISSN 1866-1793
ISBN 978-3-95806-374-7

Vollständig frei verfügbar über das Publikationsportal des Forschungszentrums Jülich (JuSER) unter www.fz-juelich.de/zb/openaccess.

Abstract

(La,Sr)(Co,Fe)$O_{3-\delta}$ is one of the most potential cathode materials for solid oxide fuel cell (SOFC) applications. Sr in this type of cathode material is very reactive to form secondary phases with other oxides, which affect micro structures and properties of the cathode material, the GDC layer and the ZrO_2-based electrolyte. The Sr related degradation issues, Cr poisoning and volatile Sr species formation, are studied. As supplement to existing experimental knowledge on Cr poisoning, specific thermodynamic aspects for Cr poisoning are discussed. The thermodynamic calculations show that $pCrO_3$ has a stronger temperature dependence than $pCrO_2(OH)_2$, and when considering the reaction between SrO and CrO_3(g), dependent on different $pCrO_3$ and local pO_2 in the cathode, different Sr-Cr-O secondary phases $SrCrO_4$, $SrCrO_3$, $Sr_3Cr_2O_8$ or Sr_2CrO_4 could be formed. Additionally, thermodynamic calculations show that in the presence of water vapor, formation of volatile $Sr(OH)_2$ is possible as well. $pSr(OH)_2$ depends on temperature, pH_2O and SrO activity, and can be of the same order of magnitude as $pCrO_2(OH)_2$. Volatile $Sr(OH)_2$ diffuse through the porous GDC layer and react with ZrO_2-based electrolytes to form $SrZrO_3$ precipitates. The reaction between gaseous Sr species and an 8YSZ sheet is studied experimentally. The surface of the 8YSZ sheet is investigated by SEM coupled with EDS, confirming the deposition of Sr. Since the reaction between the gaseous Sr species and 8YSZ depends on the ZrO_2 activity in 8YSZ, the ZrO_2 activity in 8YSZ is measured by Knudsen Effusion Mass Spectrometry. The measured $aZrO_2$ shows no temperature dependence, which is around 0.85. A high ZrO_2 activity in 8YSZ facilitates the reaction between the gaseous Sr species and 8YSZ from a thermodynamic point of view.

In addition, first principles phonon calculations combined with quasi-harmonic approximation (QHA) are used to predict the thermal expansion of $La_{0.5}Sr_{0.5}Co_{0.25}Fe_{0.75}O_3$ (LSCF55). Within the framework of the QHA, the volumetric thermal expansion coefficient of LSCF55 is calculated as $\alpha_{V,GGA} = 50.34 * 10^{-6}\,K^{-1}$. For comparison, the lattice expansion and the volume expansion of LSCF55 grain are measured by in-situ high temperature X-ray diffractometer (HT-XRD). An anisotropic thermal expansion of rhombohedral LSCF55 with $\alpha_{a,hex} = 10.89 * 10^{-6}\,K^{-1}$ and $\alpha_{c,hex} = 21.18 * 10^{-6}\,K^{-1}$ is obtained. The volumetric thermal expansion coefficient is measured as $\alpha_{V,HT-XRD} = 43.17 * 10^{-6}\,K^{-1}$. Additionally, the effectively isotropic expansion coefficients of a polycrystalline LSCF55 bar specimen are measured using a vertical high-performance thermo-mechanical analyzer and yield $\alpha_{l,bar\ specimen} = 17.37 * 10^{-6}\,K^{-1}$ and $\alpha_{V,bar\ specimen} = 52.11 * 10^{-6}\,K^{-1}$. A Good agreement between the calculated and measured values of α_V is obtained.

Zusammenfassung

$(La,Sr)(Co,Fe)O_{3-\delta}$ ist eines der leistungsfähigsten Kathodenmaterialien für Festoxidbrennstoffzellen. In dieser Art von Kathodenmaterial ist Sr sehr reaktiv, und kann sekundäre Phasen mit anderen Oxiden bilden. Die gebildeten Sekundärphasen beeinflussen die Mikrostrukturen und Eigenschaften der Kathodenmaterialien, der GDC-Schichten und der ZrO_2-basierten Elektrolyte. Die Sr-bedingten Degradationsprobleme, die Cr-Vergiftung und die Bildung flüchtiger Sr-Spezies werden im Rahmen der vorliegenden Arbeit untersucht. Ergänzend zu den vorhandenen experimentellen Erkenntnissen zur Cr-Vergiftung werden spezifische thermodynamische Aspekte diskutiert. Die thermodynamischen Rechnungen zeigen, dass der Partialdruck $pCrO_3$ eine stärkere Temperaturabhängigkeit aufweist als $pCrO_2(OH)_2$. In Abhängigkeit von den Partialdrücken $pCrO_3$ und pO_2 in der Kathode können verschiedene Sr-Cr-O Sekundärphasen $SrCrO_4$, $SrCrO_3$, $Sr_3Cr_2O_8$ oder Sr_2CrO_4 gebildet werden. Darüber hinaus zeigen thermodynamische Rechnungen, dass in Gegenwart von Wasserdampf auch die Bildung von gasförmigen $Sr(OH)_2$ möglich ist. $pSr(OH)_2$ hängt von der Temperatur, dem Druck pH_2O und der SrO-Aktivität ab und kann in der gleichen Größenordnung liegen wie $pCrO_2(OH)_2$. Flüchtiges $Sr(OH)_2$ kann durch die poröse GDC-Schicht diffundieren und mit dem ZrO_2-basierten Elektrolyten reagieren und so $SrZrO_3$-Präzipitate bilden. Die Reaktion zwischen gasförmigen Sr-Spezies und einer 8YSZ-Scheibe wird experimentell untersucht. Die Oberfläche der 8YSZ-Scheibe wird mittels SEM in Verbindung mit EDS untersucht. Die Abscheidung von Sr wird dadurch bestätigt. Da die Reaktion zwischen der gasförmigen Sr-Spezies und 8YSZ von der ZrO_2-Aktivität in 8YSZ abhängt, wird zusätzlich die ZrO_2-Aktivität in 8YSZ durch Knudsen-Effusionsmassenspektrometrie bestimmt. Die gemessene

Aktivität aZrO_2 zeigt keine Temperaturabhängigkeit, und liegt bei etwa 0,85. Eine hohe ZrO_2-Aktivität in 8YSZ begünstigt somit die Reaktion zwischen der gasförmigen Sr-Spezies und 8YSZ aus thermodynamischer Sicht.

Ab initio Phononenrechungen in Kombination mit der quasi-harmonischen Approximation (QHA) werden zur Berechnung der thermischen Ausdehnung von $La_{0.5}Sr_{0.5}Co_{0.25}Fe_{0.75}O_3$ (LSCF55) eingesetzt. Basierend auf der QHA wird der volumetrische Wärmeausdehnungskoeffizient von LSCF55 berechnet als $\alpha_{V,GGA\_QHA} = 50.34 * 10^{-6}\, K^{-1}$. Zum Vergleich werden die Gitterausdehnungen und Volumenausdehnungen eines LSCF55-Korns mittels HT-XRD gemessen und die lineare Ausdehnung einer LSCF55-Probe mit einem thermomechanischen Analysator ermittelt. Die Ergebnisse der HT-XRD zeigen, dass die thermische Ausdehnung von rhomboedrischem LSCF55 ($\alpha_{a,hex} = 10.89 * 10^{-6}\, K^{-1}$ und $\alpha_{c,hex} = 21.18 * 10^{-6}\, K^{-1}$) anisotrop ist und der volumetrische Ausdehnungskoeffizient des rhomboedrischen LSCF55 $\alpha_{V,HT-XRD} = 43.17 * 10^{-6}\, K^{-1}$ beträgt. Der lineare Ausdehnungskoeffizient der LSCF55-Probe wird als $\alpha_{l,bar\ specimen} = 17.37 * 10^{-6}\, K^{-1}$ gemessen, die effektiv isotrope Volumndehnung beträgt $\alpha_{V,bar\ specimen} = 52.11 * 10^{-6}\, K^{-1}$. Somit wird eine gute Übereinstimmung zwischen den berechneten und gemessenen Werten α_V gefunden.

Acknowledgments

In the beginning, I would like to thank Prof. Dr. Lorenz Singheiser for giving me the chance to work in the Institute of Energy and Climate Research, Microstructure and Properties of Materials (IEK-2), Forschungszentrum Jülich GmbH. Then I would like to express my appreciation to all the people made this doctoral thesis possible. Especially, I would like to express my gratitude to Prof. Dr. Lorenz Singheiser and Prof. Dr. Robert Spatschek for the inspiring discussions, careful corrections, constant encouragements and continuous contribution to the activities within the project during my entire PhD period. Additionally, I would like to thank all the institute colleagues for introductions and consistent support of the experimental equipment: Dr. Egbert Wessel and Dr. Daniel Grüner for the comprehensive SEM studies, Mr. Mirko Ziegner for the high-quality XRD measurements, Mr. Ralf Küppers for the continuous vital support in the experiment set up. I would also like to say many thanks to my best colleagues who played an important role in the scientific everyday life.

Besides, I would like to acknowledge the support for ‘Bundesministerium für Bildung und Forschung’ (BMBF) within the frame work of the project ‘SOFC-Degradation: Analyse der Ursachen und Entwicklung von Gegenmaßnahmen’, grant ID 03SF0494. I would also like to gratefully acknowledge the supercomputing time granted on JURECA at Forschungszentrum Jülich GmbH.

Finally, I would like to explain my profound gratitude to my family and my friends, especially Ding Wang, for their constant caring, support and encouragement.

Contents

x

1. Introduction

Our climate is rapidly changing and the global warming becomes an increasingly urgent problem. One of the major contributors for the global warming is the emissions of greenhouse gases, e.g. CO_2 and NO_x, by power generation and manufacturing industries etc. The development of new, low-emissions power generation technologies becomes significantly important. One such technology is the solid oxide fuel cell (SOFC), which is one of the most efficient and environmental-friendly technologies available for generating power from hydrogen, natural gas, biogas and other renewable fuels. In the SOFC application, the SOFC single cells are connected by interconnects in series and constructed into a stack. The planar designed SOFC stack is currently the dominant concept due to manufacturing advantages. However, the performance degradation of SOFC stacks limits its commercialization. Therefore, a thorough understanding of the degradation issues of SOFC stacks is significant for stack designs as well as for lifetime and performance improvements.

The degradation of cathodes has been identified as a major issue limiting the lifetime and durability of the SOFC stacks. $(La,Sr)(Co,Fe)O_{3-\delta}$ (LSCF) is one of the potential cathode materials in SOFC applications. However, Sr in this type of cathode material is a very reactive element. As shown in Fig. 1.1, on one hand, the Sr tends to segregate out from the LSCF cathode in the form of SrO and becomes a reaction partner of volatile Cr species. During operation of a SOFC stack, a Cr_2O_3-containing scale forms on the surface of the ferritic interconnect, which results in the evaporation of Cr species. The segregated SrO reacts with the volatile Cr species, forming Sr-Cr-O secondary phases, and leads to poisoning of the LSCF cathode. On the other hand, the Sr may

diffuse to the ZrO_2-based electrolyte through grain boundaries of the GDC diffusion barrier layer or by gas phase transportation, and subsequently reacts with ZrO_2 in the electrolyte, forming $SrZrO_3$ at the GDC/electrolyte interface. The formed $SrZrO_3$ is an ionic insulator, which will block the path of oxygen ion diffusion. Meanwhile, the depletion of Sr in the LSCF cathode lowers the cathode performance.

Furthermore, thermal expansion mismatches between layers of an SOFC would result in thermomechanical stress that may not be tolerated during sintering, cooling and operation processes, potentially leading to e.g. crack formation, gas leakage, delamination and final performance degradation. The thermal expansion behavior of the LSCF cathode is one of the factors that influence the mechanical stability of SOFC stacks.

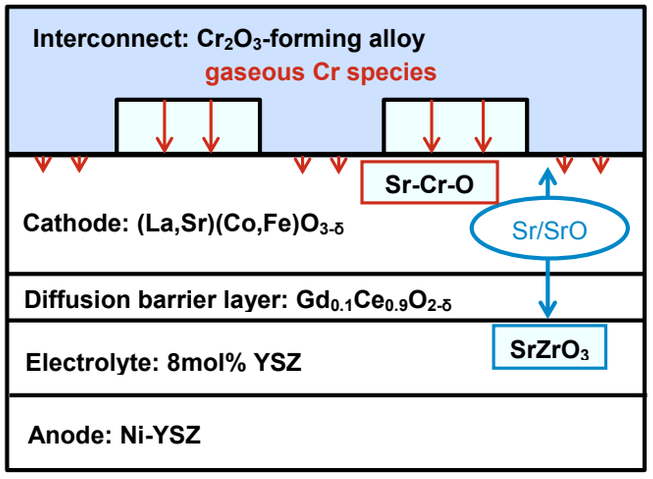

Figure 1.1: Reactivity of Sr in the LSCF cathode.

The present work is a part of a BMBF funded project, which is focused on identifying the degradation and failure issues of SOFCs for electricity generation and auxiliary plant concepts. In the framework of this thesis, the target is to study the degradation issues of the LSCF cathode and consists of two research topics:

i) Sr related degradation issues, Cr poisoning of the LSCF cathode and formation of volatile Sr species, are studied. Despite numerous experimental investigations on Cr poisoning reported in the literatures, thermodynamic aspects are widely considered and part of this thesis, in order to get a comprehensive understanding of the Cr poisoning process. Next, the volatile Sr species are analyzed by thermodynamic calculations. Then, experiments on the reaction between gaseous Sr species and the yttria stabilized zirconia electrolyte are performed. Additionally, since the thermodynamic activity of ZrO_2 ($aZrO_2$) in the yttria stabilized zirconia electrolyte is one of the decisive factors on the $SrZrO_3$ formation, $aZrO_2$ in 8mol-% Y_2O_3-ZrO_2 (8YSZ) is measured by Knudsen Effusion Mass Spectrometry (KEMS).

ii) The thermal expansion behavior of LSCF is significant for the SOFCs design and performance. Besides experimental investigations on the thermal expansion coefficients of LSCF, a careful understanding of the thermal expansion behavior of the LSCF cathode from a theoretical perspective is presently missing. First principles phonon calculations combined with the quasi-harmonic approximation (QHA) are used for predicting the thermal expansion coefficient of $La_{0.5}Sr_{0.5}Co_{0.25}Fe_{0.75}O_3$, and the results are compared to experimental investigations.

2. Literature reviews

2.1 Working principles of solid oxide fuel cell

A solid oxide fuel cell (SOFC) is a pollution-free power generation device that converts chemical energy into electrical energy with high efficiency. Basically, it is composed of a dense electrolyte that is sandwiched by a porous cathode and a porous anode (Fig. 2.1). It requires the fuel, such as hydrogen or natural gas, and oxidant reactants, such as oxygen or air to electrochemically react at high temperature and generate electrical energy.

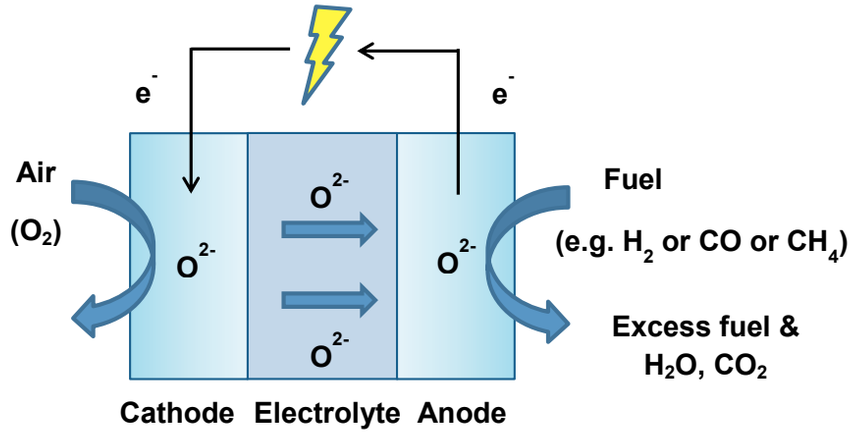

Figure 2.1: Working principle of SOFC.

The LSM cathode is a very good electronic conductor, but has negligible ionic conductivity. Therefore, the oxygen reduction take places at the three-phase boundary regions, where the oxygen meets both the cathode and electrolyte. Due to its low oxygen ion conductivity and high activation energy for oxygen dissociation, the performance of LSM cathode decreases rapidly as the operating temperature is lowered. Therefore, a mixed conductive cathode is desirable instead of LSM cathode, when the operation temperature of SOFCs is reduced. The mixed conductive cathode can be realized by mixing an ionic conductive material with LSM to create a composite cathode (e.g. LSM-YSZ [32]) or replacing the present material by another mixed conductive perovskite material (e.g. $(La,Sr)(Co,Fe)O_{3-\delta}$).

2.2.4.2 $(La,Sr)(Co,Fe)O_{3-\delta}$ cathode

$(La,Sr)(Co,Fe)O_{3-\delta}$ (LSCF) perovskite oxide has sufficient electronic conductivity, high oxygen ionic conductivity, and high catalytic activity for the O_2 reduction reaction in temperature range from 600 °C to 800 °C [33-36]. It is a promising cathode material for intermediate-temperature solid oxide fuel cells (IT-SOFC). By substituting Sr for La at A-sites in $La(Co,Fe)O_3$, in order to maintain electronic neutrality, the substitution of Sr ions must be compensated by one or both of the following ways: i) electronic compensation by oxidizing B^{3+} to B^{4+} and ii) ionic compensation by formation of oxygen vacancies. The ionic and electronic compensations occur simultaneously and compete with each other. The electro-neutrality condition is expressed as [37]:

$$3Sr'_{La} = B^{\cdot}_{B} + 2V^{\cdot\cdot}_{O} \tag{2.7}$$

Therefore, LSCF has mixed electronic and ionic conductivity. The oxygen reduction process therefore takes place, unlike the LSM cathode, at the LSCF cathode surface by producing oxygen ions and consuming electrons. The produced oxygen ions are then transported through the LSCF cathode to the electrolyte, while the electrons are supplied from the current-collector.

Similar to the LSM cathode, the LSCF cathode is also not chemically compatible with the ZrO_2-based electrolyte (e.g. 8YSZ). The ionic insulator $SrZrO_3$ forms at the interface

During the operation, oxygen is reduced at the cathode side into oxygen ions that subsequently diffuse through the electrolyte to the anode. The cathode reaction is:

$$O_2(g) + 4e^- \rightarrow 2O^{2-} \tag{2.1}$$

Fuel (e.g. H_2, CO or CH_4) is fed to the anode, where it is oxidized. Simultaneously, electrons are generated. The electricity is, thus, produced by the flow of electrons in the external circuit. As an example, if H_2 is fed to the anode, then the anode reaction is:

$$2H_2(g) + 2O^{2-} \rightarrow 2H_2O(g) + 4e^- \tag{2.2}$$

Thus, the overall reaction, like combustion, yields water vapor as reaction product:

$$2H_2(g) + O_2(g) = 2H_2O(g) \tag{2.3}$$

In this case, the reversible cell potential or the theoretical open circuit voltage, E_r, can be calculated by the Nernst equation:

$$E_r = E^\circ + \frac{RT}{nF} ln\left(\frac{(pH_2)^2 * pO_2}{(pH_2O)^2}\right) \tag{2.4}$$

Where n is the number of electrons (n=4 in this case) that transfers during the reaction (in mole), E° is the standard reversible cell potential which can be calculated from $E^\circ = -\frac{\Delta G^\circ}{nF}$, F is the Faraday constant (F=96485 C mol^{-1}), R is the ideal gas constant (R=8.314 J mol^{-1} K^{-1}), and T is the temperature in K. If the cathode gas is air (i.e. pO_2=0.21 bar) and anode gas is 3% H_2O humidified hydrogen (i.e. pH_2O=0.03 bar and pH_2=0.97 bar), then at 800 °C, when $H_2O(g)$ is the reaction product, the reversible cell potential of an SOFC single cell is about 1.1 V. The real potential of the cell is reduced when the current is drawn due to the different polarizations. In order to obtain higher voltage, an SOFC stack is required.

There are two main designs for an SOFC: the tubular design and the planar design. Fig. 2.2a-(i) is a possible tubular design that has been demonstrated by Siemens Westinghouse. In this design, the cell is built up in thin layers on the cathode tube, which fabricated by extrusion and sintering. An axial interconnector makes the cathode accessible and allows cells to be connected in series. Fig. 2.2a-(ii) shows the planar

design. In this design, the cell components are configured as thin, flat plates. The interconnector, which has gas channels on both sides, connects the anode and the cathode of adjoining cells. The tubular design guarantees long-term stability, while the planar design promises higher power densities [1]. As an example, the construction of planar SOFC stacks is shown in Fig. 2.2b. The planar cells are integrated into a steel frame and stacked with interconnects. A sealant is used to seal and join the individual components. The planar design is currently the dominant design due to manufacturing advantages and specially compatibility.

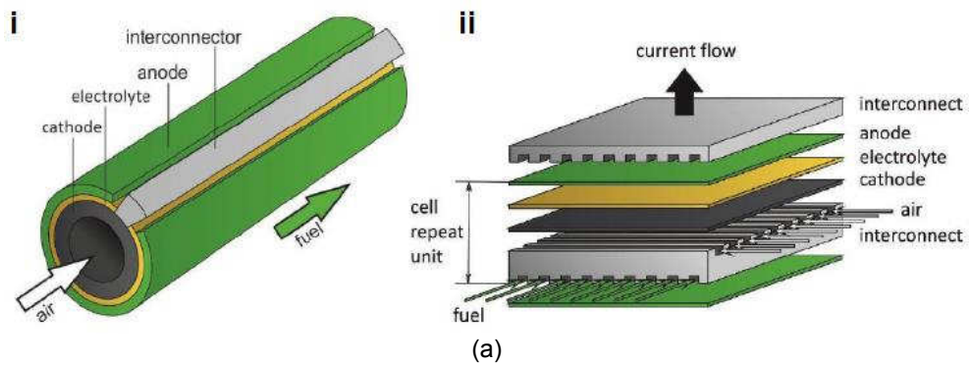

(a)

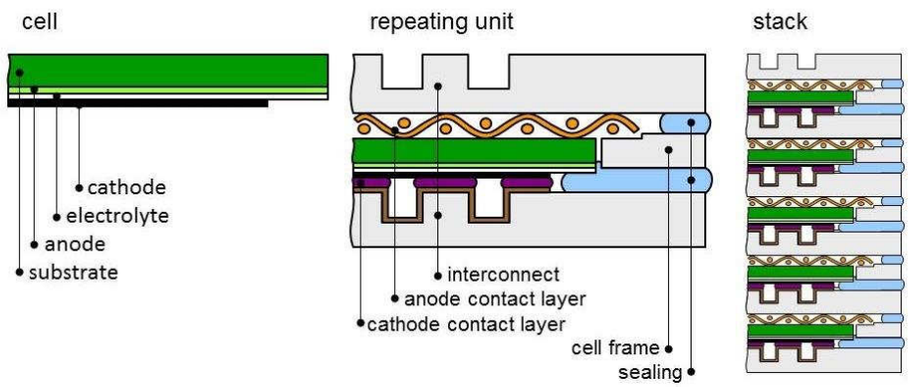

(b)

Figure 2.2: a) Tubular (i) and planar (ii) SOFC designs [2] and b) SOFC stacks with planar designs [3].

2.2 Components in planar SOFCs

2.2.1 Interconnect

The interconnect in SOFCs physically and electrically connects the anode of one cell to the cathode of the neighboring cell. It separates air at the cathode side from fuel at the anode side. Therefore, the interconnect should have high electronic conductivity, chemical stability under both oxidizing and reducing atmospheres, excellent impermeability, easy access for gas flow, good mechanical properties, and thermo-mechanical compatibility with other cell components [4]. Generally, the interconnects can be classified into two types: ceramic interconnects and metallic interconnects. Compared to ceramic interconnects, metallic interconnects have more reliable conductivity, cheaper and easier to manufacture. Most metallic interconnects are chromium-based alloys, since they have reasonable oxidation protection, satisfactory thermal expansion behavior and relatively high electronic conductivity [4]. However, the chromium-based alloys have an unacceptable high oxidation rate of Cr and produce volatile Cr species at the operation temperatures of SOFCs. The volatile Cr species leads to poisoning of the cathode and degradation of the SOFC performance. This aspect will be studied in detail in the framework of this thesis in Chap. 4.1.

The high-temperature ferritic stainless steel Crofer® 22 APU (Thyssen VDM, Germany) is a representative metallic interconnect candidate [5-7]. It fulfills all the requirements for the interconnect. Additionally, during the SOFCs operation, a $(Cr,Mn)_3O_4$ spinel oxidation layer is formed on the surface of Crofer® 22 APU [8-10]. Comparing to a pure Cr_2O_3 oxidation layer, lower chromium evaporation is realized by this $(Cr,Mn)_3O_4$ spinel oxidation layer. To get an additional reduction of chromium evaporation, a $(Co,Mn)_3O_4$ spinel protective coating is normally applied on the interconnect [11-13].

2.2.2 Electrolyte

The electrolyte is responsible for conducting ions between the electrodes, for separating of the reacting gases and for blocking the internal electronic conduction and forcing the

electrons to flow through the external circuit. The electrolyte should be stable under both oxidizing and reducing atmosphere and should not react with either electrode at the operation temperature. The electrolyte should have sufficiently high ionic conductivity but low electronic conductivity at operation temperature. The physical properties, such as thermal expansion and mechanical strength should be optimized with respect to cathode and anode materials. In addition, the electrolyte material must be able to be formed into a thin, strong film without gas leaks [14]. At present, ZrO_2-based electrolyte is considered as one of the promising candidates for SOFCs [15]. Pure ZrO_2 undergoes phase transitions from monoclinic to tetragonal at about 1173 °C and then to cubic at about 2370 °C. The phase transition is accompanying by volume changes which decreases the mechanical stability and thermal shock resistance of ZrO_2 [16]. By adding dopants, e.g. Y_2O_3 and Sc_2O_3, the cubic ZrO_2 phase, which is the only structure that shows considerable ionic conductivity, can be stabilized down to room temperature. Besides stabilizing the cubic structure, the dopants (M_2O_3, e.g. M=Y or Sc) can also increase the concentration of oxygen vacancies and thus leads to high oxygen ion conductivity:

$$M_2O_3 + 2Zr_{Zr}^{\times} + O_O^{\times} \rightarrow 2M'_{Zr} + V_O^{\cdot\cdot} + 2ZrO_2 \qquad (2.5)$$

8mol-%Y_2O_3 stabilized ZrO_2 (8YSZ) is widely applied as electrolyte in SOFCs. It fulfils the fundamental requirements for the electrolyte and possesses an adequate ionic conductivity which is about 0.13 S cm^{-1} at 1000 °C [17].

2.2.3 Anode

The role of the anode in an SOFC is to provide sites for the fuel gas to react with the oxygen ions that are delivered by the electrolyte. An ideal anode should be mechanically and chemically compatible with the other cell components such as the electrolyte and the interconnect. In addition, the anode should have sufficient porosity to provide paths for gas transportation and sufficient ionic and electronic conductivity [18]. The most common anode material is a porous Ni-YSZ cermet, in which Ni supplies high electronic conductivity and has in addition an excellent electro catalytic property for H_2 oxidation. YSZ supplies high ionic conductivity, acts as a framework for Ni dispersion,

and ensures a compatible thermal expansion with other components (e.g. YSZ electrolyte) [19]. The H_2 oxidation reaction takes place at the three phase boundary, where fuel gas, Ni and YSZ phases meet together. The general processing route for Ni-YSZ cermet anodes involves the following steps: i) homogeneous mixing of appropriately sized NiO and YSZ powder in an appropriate composition; ii) anode sintering at high temperature and iii) reducing NiO/YSZ into Ni/YSZ during the SOFC operation or externally reducing in N_2+H_2 atmosphere at SOFC operation temperature. The reduction of NiO into Ni is associated with the generation of pores as volume reduction of about 41% [20]. The electrical, electrochemical and mechanical properties of Ni/YSZ anodes are strongly influenced by the composition, microstructure and porosity of the composites. At least 30 vol.%-Ni is expected to ensure sufficient electronic conductivity [21].

2.2.4 Cathode

Similar to the other components in an SOFC, the cathode should be mechanically and chemically compatible with other cell components. Similar to the anode, the cathode should have sufficient porosity for rapid diffusion of molecular oxygen and sufficient electronic and ionic conductivity to minimize the ohmic losses. In addition, the cathode should possess good tolerance towards impurities in the surrounding atmosphere. Perovskite oxides are promising candidates for the cathode materials in SOFCs [22]. The chemical formula of a typical perovskite oxide is ABO_3, where A is the larger cation and B is the smaller cation. The ideal structure of perovskite oxide has a cubic symmetry. It can be viewed either as corner-sharing A-site cations with B-site cations at the center of cubic (Fig. 2.3a) or corner-sharing BO_6 octahedra with A-site cations located in twelve-coordinated interstices (Fig. 2.3b). For most of the perovskite oxides applied as cathode in SOFCs, the A-site cation is a mixture of rare earth and alkaline earth atoms (such as La and Sr, Ca or Ba), while the B-site cation is a reducible transition metal (such as Mn, Fe, Co, or Ni) [23]. Due to the tilts of BO_6 octahedras, many perovskite oxides are slightly distorted from the ideal cubic symmetry [24, 25]. For example, $La_{1-x}Sr_xCo_{1-y}Fe_yO_{3-\delta}$ perovskites have a rhombohedral symmetry at low

temperature, and transform at higher temperature to a cubic symmetry by a second order phase transition [26, 27].

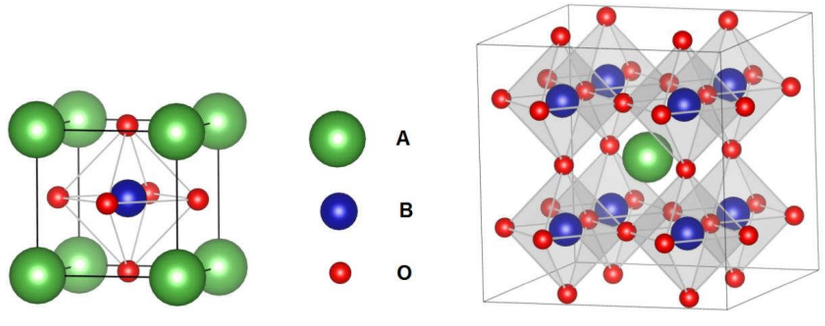

(a) (b)

Figure 2.3: The cubic perovskite ABO_3 with a) B cation at the center of the cell and b) corner-sharing BO_6 octahedral with A cation located in 12-coordinated interstices.

2.2.4.1 $La_{1-x}Sr_xMnO_{3\pm\delta}$ cathode

For many years, $La_{1-x}Sr_xMnO_{3\pm\delta}$ (LSM) perovskite has been the state-of-the-art cathode material for SOFC operations, since it possesses high stability and high electro-catalytic activity for oxygen reduction at high temperatures (T>1000°C) [28]. By substituting Sr for La in $LaMnO_3$, instead of forming oxygen vacancies, the manganese ion is oxidized according to Eq. 2.6 [29]:

$$Mn_{Mn}^{\times} + SrO \xrightarrow{LaMnO_3} Sr_{La}' + Mn_{Mn}^{\cdot} + O_O^{\times} \qquad (2.6)$$

Therefore, the electron-hole concentration is effectively increased and the electronic conductivity is improved. The electronic conductivity increases with the Sr concertation and reaches a maximum at about x=0.5 [30]. However, higher levels of Sr-substitution (x>0.3) will result in the formation of poorly electronic conducting $SrZrO_3$ at the cathode/electrolyte interface [31]. Thus, the Sr substitution is expected to be less than 30% to guarantee sufficient electronic conductivity without forming insulating secondary phases.

of LSCF cathode and ZrO_2-based electrolyte. Due to the high kinetic driving force for Sr ion diffusion at high temperatures, the $SrZrO_3$ formation is favorable during the cathode sintering process [38, 39]. A gadolinium doped cerium oxide (GDC) diffusion barrier layer is therefore introduced between the electrolyte and the cathode to suppress the formation of $SrZrO_3$ [40-42]. Additionally, the LSCF cathode is also sensitive to the volatile Cr species and poisoned by forming Sr-Cr-O secondary phases. Some degradation issues of LSCF cathode are introduced in Chap. 2.3.

An appropriate composition of LSCF should be chosen, to guarantee sufficient ionic and electronic conductivity and to have a matched thermal expansion coefficient (TEC) with the adjacent layers. A higher amount of Sr atoms instead of the trivalent La on A-sites increases the ionic and electronic conductivity and the surface change of oxygen, which can be explained by the larger number of oxygen vacancies and electronic holes [43]. Meanwhile, with increasing of Fe content at the B-sites, the TEC of LSCF is reduced that can be matched with the YSZ electrolyte or the gadolinium-doped ceria oxide diffusion barrier layer [26, 44, 45]. The composition $La_{0.6}Sr_{0.4}Co_{0.2}Fe_{0.8}O_{3-\delta}$ or the composition with slightly A-site deficiency $La_{0.56}Sr_{0.4}Co_{0.2}Fe_{0.8}O_{3-\delta}$ is preferentially applied as the cathode material in SOFCs. $La_{0.6}Sr_{0.4}Co_{0.2}Fe_{0.8}O_{3-\delta}$ has the highest electronic conductivity with the peak value of 330 S cm^{-1} at 550 °C [37]. The TEC of $La_{0.6}Sr_{0.4}Co_{0.2}Fe_{0.8}O_{3-\delta}$ in the temperature range from 100 °C to 600 °C is about $15.3*10^{-6}$ K^{-1} [37], which is thermally compatible with the $Gd_{0.9}Ce_{0.1}O_{2-\delta}$ diffusion barrier layer ($\alpha_l = 13.4*10^{-6}$ K^{-1} [46]). The stability and durability for LSCF cathode is one of the decisive factors for the SOFC performance. A better understanding of the degradations issues of LSCF cathode is the cornerstone for improving cathode performance.

2.3 Degradation issues of LSCF cathode

The degradation issues of cathode material in SOFCs is mostly caused by the following effects [47]: i) secondary phase formation (e.g. $SrZrO_3$ at the interface of LSCF/ZrO_2-based electrolyte); ii) poisoning of the cathode (e.g. Cr-poisoning); iii) decomposition of cathode material; iv) coarsening of the microstructure due to sintering and v) spallation of the cathode due to the thermal expansion mismatch. All of these effects are dependent on each other and influenced by the manufacturing parameters (e.g. layer deposition method and sintering temperature) and operation parameters (e.g. operation temperature, current density and properties of cathode gas) of the SOFCs. Generally, the degradation issues of an LSCF cathode can be classified into two main aspects: the Sr-related degradation issues and the thermal expansion related degradation issues.

2.3.1 Sr-related degradation issues

Sr is a reactive element in the LSCF cathode material that has significant influence on several degradation issues of SOFCs. Sr tends to diffuse out from the LSCF cathode, enriching at the surface of LSCF cathode and becomes a reaction partner for volatile Cr species. Besides, Sr ions diffuse from the LSCF cathode to the ZrO_2-based electrolyte and form $SrZrO_3$, which is an ionic insulator and blocks oxygen ion diffusion to the ZrO_2-based electrolyte. In addition, volatile Sr species may form under some conditions that will result in Sr depletion in the LSCF cathode and subsequent degradation of cathode performance. The volatile Sr species may also contribute to the $SrZrO_3$ formation.

2.3.1.1 Sr surface segregation and Cr poisoning

Sr tends to diffuse out from the LSCF cathode and becomes a reaction partner for volatile Cr species. Sr-surface segregation has been widely investigated. S. P. Simner et al. [48] utilized XPS analysis to study the surfaces of two porous $La_{0.6}Sr_{0.4}Co_{0.2}Fe_{0.8}O_{3-\delta}$ (LSCF6428) specimens: i) pre-tested: LSCF6428 cathode sintered onto cell at 1050 °C for 2 h (no additional processing), and ii) post-tested: cell operated at 750 °C and 0.7 V for 500 h. As a result, the surface compositions of the pre-

tested LSCF6428 were close to the desired values, i.e. Sr/(La+Sr) = 0.4 and Co/(Fe+Co) = 0.2, while, for the post-tested LSCF6428, Sr-enrichment occurred at the LSCF6428 surface, and the ratio of Sr/(La+Sr) became 0.85. Z. Pan et al. [49] employed XPS analysis to investigate the surface compositions of four LSCF samples: i) raw LSCF6428 powder, ii) freshly prepared LSCF6428 electrode (slurry coating and sintered at 900 °C for 2 h), iii) LSCF6428 electrode after 24 h annealing, and iv) nitric acid treated LSCF6428 electrode after annealing. The XPS results showed that Sr tends to enrich at the surface area of LSCF6428 particles, and an increasing Sr concentrations were detected on the freshly prepared LSCF6428 electrode and the annealed LSCF6428 electrode. In addition, after nitric acid treatment to remove possible surface components of annealed LSCF6428 electrode, the Sr concentration decreased to the value of the raw LSCF6428 powder. D. Oh et al. [50] performed heat treatments for dense LSCF bar samples in stagnant air between 600 °C and 900 °C for 50 h. SEM results showed that after heat treatment submicron precipitates formed on the surfaces, and these precipitates became more pronounced with increasing temperature from 600 °C to 900 °C. In their study, Auger Electron Spectroscopy (AES) analysis was then carried out to investigate the compositional change of the surface region after heat treatment. As a result, surface enrichment of Sr was detected. Chemical analysis of the precipitate was then conducted using TEM and EDS. The intensity of the Sr peak increased in the precipitate region compared with that of the bulk. They concluded that the precipitate was Sr-O based. Further, L. Zhao et al. [51, 52] investigated the surface of dense LSCF6428 bar specimens after heat treatment at 800°C for 96h in dry and humid air, respectively, by FIB-EDS mapping, atomic force microscopy and Raman spectroscopy. They proposed that SrO segregated on the LSCF6428 surface.

In SOFC stacks, chromium containing steels, e.g. Crofer® 22 APU, are representative candidates of interconnect materials [5-7]. During operation, a Cr_2O_3 containing scale forms on the metallic interconnect and leads to the evaporation of gaseous Cr species (e.g. CrO_3 or $CrO_2(OH)_2$) from this scale [5, 8, 9]. The segregated SrO is a Cr getter. It reacts with the evaporated Cr species, forming Sr-Cr-O secondary phases that can block the area for oxygen reduction, and subsequently leads to pronounced

performance degradation of the SOFC. C. C. Wang et al. [53] and L. Zhao et al. [51, 52] demonstrated the formation of $SrCrO_4$ at surface of the dense LSCF6428 bar specimens after heat treatment with gaseous Cr species. Under realistic SOFC operation condition, according to the work of N. H. Menzler et al. [54], a long-term steady-state SOFC stack operation was performed for 17000 h at 700 °C and with the constant current density 0.5 A cm^{-2}. After that $SrCrO_4$ was found on the top of the $La_{0.58}Sr_{0.4}Co_{0.2}Fe_{0.8}O_{3-\delta}$ cathode surface, where it was adjacent to the contact bar of the interconnect (Fig. 2.4). Sometimes Cr rich strontium oxide was also detected inside the LSCF cathode, e.g. at the LSCF/electrolyte interface. N. H. Menzler et al. [55] performed a stack test for anode-supported SOFCs with $La_{0.58}Sr_{0.4}Co_{0.2}Fe_{0.8}O_{3-\delta}$ cathode, dense thin-film GDC diffusion barrier layer and thin-film 8YSZ electrolyte for about 1300 h at 700 °C then subsequently for 1200 h at 600 °C. Besides observing $SrCrO_4$ on the top of cathode, a Sr-Cr-O precipitate was detected at the LSCF/GDC interface (Fig. 2.5). However, due to the small size of precipitates, it was difficult to analyze in detail the composition and the stoichiometry.

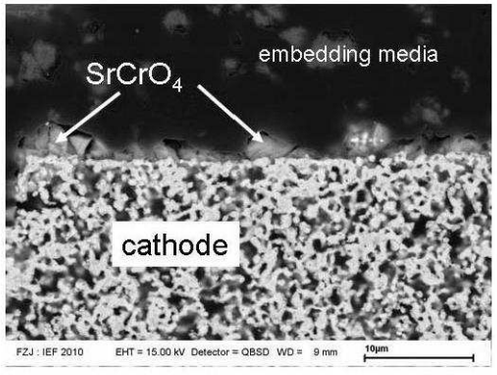

Figure 2.4: SEM cross-sectional micrograph of the LSCF cathode part adjacent to the contact bar [54].

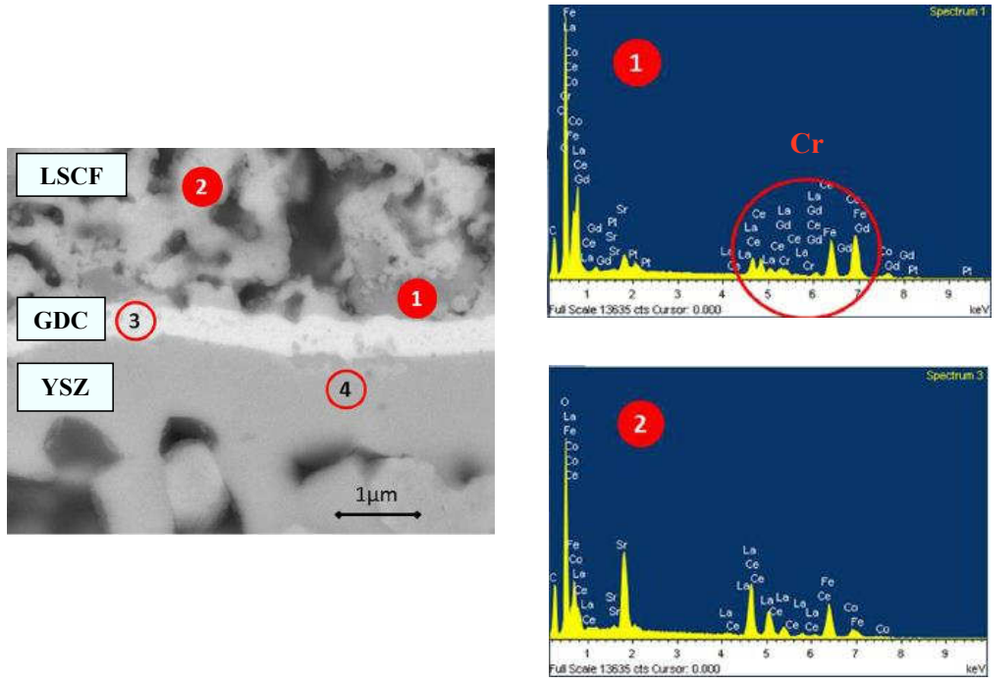

Figure 2.5: SEM cross-sectional micrograph and EDS spectra of point 1 and point 2: an example to show Cr deposition at the LSCF/GDC interface [55].

2.3.1.2 Diffusion of Sr ions and formation of $SrZrO_3$

Another Sr related degradation issue of SOFCs is diffusion of Sr ions from the LSCF cathode to the ZrO_2-based electrolyte and subsequent formation of the ionic insulator $SrZrO_3$ at the LSCF/ZrO_2-based electrolyte interface. To suppress the formation of $SrZrO_3$, a gadolinium doped cerium oxide (GDC) diffusion barrier layer is therefore applied between the electrolyte and the cathode. However, it is still difficult to completely prevent the $SrZrO_3$ formation especially during the cathode sintering process. A. Mai et al. [56] tested the performance of anode-supported SOFCs with $La_{0.58}Sr_{0.4}Co_{0.2}Fe_{0.8}O_{3-\delta}$ cathode, porous GDC layer and 8YSZ electrolyte. They found that $SrZrO_3$ formed at the GDC/8YSZ electrolyte interface during the cathode sintering process at 1080°C for 3 hours. S. Uhlenbruck et al. [57] implemented TEM+EDS

element mappings to investigate the cross sections of the cells with porous and dense GDC layer, respectively, after cathode sintering process. Islands of $SrZrO_3$ were only found at the porous GDC/8YSZ electrolyte interface. R. Knibbe et al. [58] studied anode-supported SOFCs with porous and dense GDC layer, respectively. The cell with a dense GDC layer was operated at 650 °C with current a density of 0.75 A cm^{-2} for 1500 h. The cell with porous GDC layer was only sintered at above 1300 °C without cell operation. As a result, $SrZrO_3$ grains were detected in the size of several hundred nanometers by TEM at the dense GDC/8YSZ interface before cell operation. After cell operation, the size of the $SrZrO_3$ remains similar, indicating no further $SrZrO_3$ growth during the operation. In contrary, for the cell with porous GDC layer, a thick $SrZrO_3$ layer was detected by BSE+EDS at the porous GDC/8YSZ interface after sintering. Therefore, the dense GDC layer had better Sr retention than the porous GDC layer and the grain boundaries of GDC layer provide pathways for Sr diffusion to the electrolyte. According to F. F. Wang et al. [59], the diffusion triplets, LSCF(porous)/GDC(dense)/8YSZ(dense), were annealed at 1100 °C and 1200 °C, respectively, for one week. After annealing, $SrZrO_3$ was detected both at the LSCF/GDC interface and the GDC/8YSZ interface. They proposed that the grain boundary diffusion of Sr and Zr across the GDC layer resulted in the $SrZrO_3$ formation along the interfaces at both sides of GDC layer and the evolving cracks in GDC layer additionally supplied a pathway for Sr surface diffusion. J. De Vero et al. [60] studied the effect of the LSCF microstructure on the stability of the GDC interlayer by performing cation diffusion experiments on LSCF/GDC/YSZ triplets. The porous and dense LSCF layer was deposited on the pre-annealed dense GDC/YSZ couples, respectively. The LSCF/GDC/YSZ triplets were annealed at temperatures ranging from 800 °C to 1000°C for 168 h to 731 h. Their results showed that porous LSCF enhanced Sr-diffusion from the grain of the LSCF to the GDC interlayer, resulting in the severe formation of $SrZrO_3$ at the LSCF/GDC interface, while Sr and Zr diffusion along the grains of the GDC interlayer dominates the formation of $SrZrO_3$ at the GDC/YSZ interface. According to N. Sakai et al. [61], the grain boundary diffusion coefficient of Sr in ceria was estimated to be 10^5 times larger than bulk diffusion.

2.3.1.3 Volatile Sr species

The volatile Sr species formation could be also one of the degradation issues in SOFCs. So far, only few research activities have been focused on volatile Sr species formation in SOFCs. Tietz et al. [62] investigated the Sr distribution around LSCF cathodes after long term operation of SOFCs by secondary ion mass spectrometry (SIMS). The Sr concentration was found to vary systematically along the gas flow direction. They proposed that Sr was transported by gas phase evaporation and deposition. The evaporation of Sr leads then to a Sr depletion in the LSCF cathode and subsequently lowers the cathode performance. In addition, a recent work of Z. Lu et al. [63] proposed that during the LSCF cathode sintering process volatile Sr species contributed to the $SrZrO_3$ formation at the Sm-doped ceria interlayer/YSZ electrolyte interface.

2.3.2 Thermal expansion mismatches

The planar designed SOFC has a configuration of layered morphological structure, and therefore the thermal expansion behaviors of different layers are significant for the structure design and long term operation. A thermal expansion mismatch between layers would result in thermomechanical stress that may not be tolerated during sintering, cooling and operation processes, potentially leading to e.g. crack formation, gas leakage, delamination and finally performance degradation. According to J. Malzbender et al. [64], the planar designed SOFC typically exhibit a curvature behavior and develop residual stresses originating from the thermal mismatch between the layers. The curvature degrades the SOFC performance and in addition, if the residual stresses exceed the strength of the involved materials, it will lead to mechanical failure of the SOFC. According to L. Blum [65], a further problem can occur that due to the different thermal expansion behaviors of different functional layers, micro-gaps may form between the electrodes and adjacent contact layers with changing the temperature. It will lead to contact loss at the mechanically weakest point and subsequent performance degradation. His study is focused on the standard stack design proposed by Forschungszentrum Jülich GmbH, the so-called F-design [6, 66], in which a rigid glass-ceramic sealing is used [67]. As shown in Fig. 2.6, at the anode side, the differences in

thermal expansion between the inner assembly (a glass ceramic sealing, anode substrate and nickel mesh) and the outer assembly (two layers of glass-ceramic sealing and a metal frame) are responsible for the gap formation on the anode side. At the cathode side, the micro gap (black circle) is preferentially created depending on the differences in thermal expansion between the glass-ceramic and the LSCF cathode with the cathode contact layer. The thermal expansion behavior of the LSCF cathode is one of the factors that influence the mechanical stability of SOFCs. Therefore, the thermal expansion coefficients of LSCF with regard to different compositions have been widely experimentally studied [44, 68-71]. Besides those experimental approaches, a careful understanding of the thermal expansion behavior of LSCF from a theoretical perspective is scientifically desirable and is a part of this thesis.

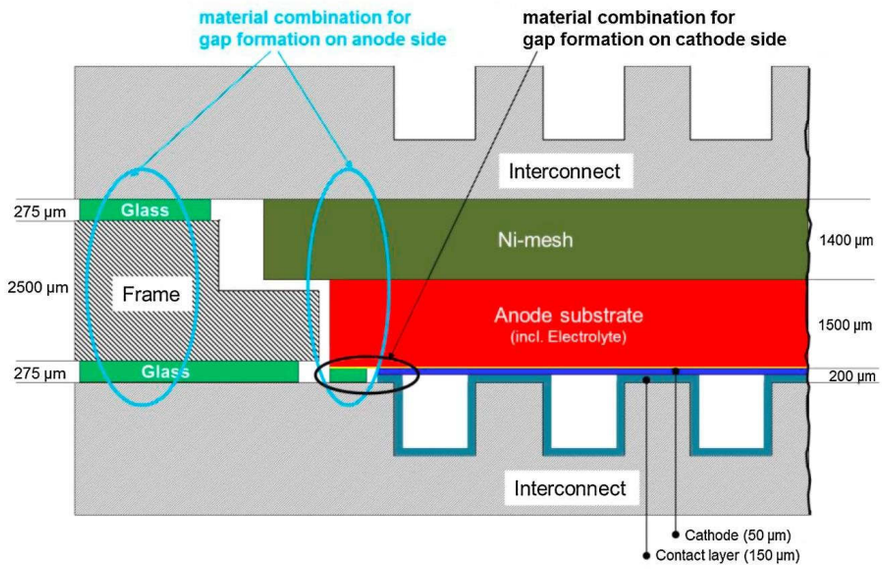

Figure 2.6: Simplified assembly sketch of F-design stacks with the thickness of different layers at T_{max} which is 50 K below the sealing temperature [65].

3. Theories and methods in this thesis

In the present thesis, thermodynamic calculations are performed to study Sr-related degradation issues of the LSCF cathode, Knudsen Effusion Mass Spectrometer (KEMS) is used to measure the ZrO_2 activity in yttia stabilized zirconia electrolyte, and first principles phonon calculations combined with quasi harmonic approximation (QHA) are used to predict the thermal expansion of the LSCF cathode. In this chapter, some theories related to thermodynamics, first principles based calculations and KEMS measurement are introduced.

3.1 Thermodynamic potential

A thermodynamic potential is a quantity used to represent the state of a system, and it can be described by its natural variables, e.g. temperature (T), entropy (S), pressure (p), volume (V) and number of particles (N_i). The natural variables are a set of appropriate variables that allow computing other state functions by partial differentiation of the thermodynamic potentials. There are general four different thermodynamic potentials: internal energy (U), enthalpy (H), Gibbs free energy (G) and Helmholtz free energy (F), in which the Gibbs free energy (G) and the Helmholtz free energy (F) are the most important potentials in the frame work of this thesis.

3.1.1 Internal energy

The internal energy is the energy associated with the random, disordered motion of molecules of the system. Based on the first law of thermodynamics, any differential change in the internal energy U of a system equals the net heat transfer into the system

Q, plus the net work done on the system and plus, in some cases, with any change due to the addition of new particles to the system:

$$dU = \delta Q + \delta W + \sum_i \mu_i dN_i, \tag{3.1}$$

where, δQ is the infinitesimal heat flow into the system, δW is the infinitesimal net work done on the system, μ_i is the chemical potential of particle i and N_i is the number of particles i. By considering a reversible process, in which the process-dependent heat and work can be both written in terms of changes in state variable. δQ to a system can be described by an infinitesimal increment in the entropy (dS) of the system times temperature T:

$$\delta Q = T * dS \tag{3.2}$$

If the work (δW) is done by the system on the environment, δW can be described by the internal pressure (p) of the system times the infinitesimal increment of the volume (dV) of the system:

$$\delta W = -p * dV \tag{3.3}$$

Therefore, any differential change in the internal energy (dU) of a system can be written as:

$$dU = TdS - pdV + \sum_i \mu_i dN_i \tag{3.4}$$

The internal energy U is a function of the natural variables S, V and N_i.

3.1.2 Enthalpy

The enthalpy describes the total heat content of a system and is defined as:

$$H = U + p * V \tag{3.5}$$

Performing the derivation of Eq. 3.5 yields:

$$dH = dU + pdV + Vdp \tag{3.6}$$

Substituting Eq. 3.4 into Eq. 3.5, yields:

$$dH = TdS + Vdp + \sum_i \mu_i dN_i \tag{3.7}$$

The enthalpy H is a function of the natural variables S, p and N_i.

3.1.3 Gibbs free energy

The Gibbs free energy is defined by the expression:

$$G = U + p * V - T * S \tag{3.8}$$

It can be used to calculate the maximum of reversible work that can be performed by a thermodynamic system at constant temperature and pressure. By calculating the derivative of Eq. 3.8 and substituting Eq. 3.4 into Eq. 3.8:

$$dG = Vdp - SdT + \sum_i \mu_i dN_i \tag{3.9}$$

The Gibbs free energy G is a function of p, T and N_i. By substituting Eq. 3.5 into Eq. 3.8, the Gibbs free energy can also be written as:

$$G = H - T * S \tag{3.10}$$

The Gibbs free energy is widely used in studying chemical reactions. If a chemical reaction is run at constant temperature, the change in the Gibbs free energy (ΔG) of the system that is therefore given as:

$$\Delta G = \Delta H - T * \Delta S \tag{3.11}$$

ΔG is a critical parameter in determining whether the chemical reaction will take place in the given direction. For a reversible chemical reaction:

$$aA(s) + bB(g) \leftrightharpoons cC(s) + dD(g) \tag{3.12}$$

ΔG can be found by:

$$\Delta G = \left(\sum_i^n \upsilon_i G_{fi}\right)_{products} - \left(\sum_i^n \upsilon_i G_{fi}\right)_{reactants} \tag{3.13}$$

Where, υ_i are the stoichiometric coefficients (a, b, c, d in Eq. 3.12) for species i and G_{fi} is the Gibbs energy formation per mole of species i. If $\Delta G < 0$, the reaction can take place spontaneously in the given direction. If $\Delta G > 0$, the reaction can take place

spontaneously in the opposite direction. If $\Delta G = 0$, the reaction is at equilibrium, when there is no tendency for the quantities of reactants and products to change.

As another expression, ΔG at any moment of the given reaction can be calculated from:

$$\Delta G = \Delta G° + RTlnQ \tag{3.14}$$

Here, $\Delta G°$ is the change of the standard Gibbs free energy; R is the ideal gas constant that equal to 8.314 J mol^{-1} K^{-1}; T is the absolute temperature and Q is the reaction quotient that measured the relative quantities of the products and reactants at a point in time during the reaction:

$$Q = \frac{[C]^c \times [D]^d}{[A]^a \times [B]^b} \tag{3.15}$$

To define the Q, molar concentrations of the substances in the reaction are used and symbolized using square brackets. At equilibrium, $\Delta G = 0$ and Q is equal to the equilibrium constant of the reaction (K), hence:

$$\Delta G° = -RTlnK \tag{3.16}$$

For the given reaction (Eq. 3.12), the activities of a pure solid (A and C) are equal to 1 and can be eliminated from the equation. Therefore, the equilibrium constant (K_p) can be given by using the partial pressure of the gas phases as:

$$K_p = \frac{(pD_{eq})^d}{(pB_{eq})^b} \tag{3.17}$$

If the equilibrium partial pressure of B is known, then the equilibrium partial pressure of D can be calculated as:

$$pD_{eq} = \sqrt[d]{K_p \times (pB_{eq})^b} \tag{3.18}$$

3.1.4 Helmholtz free energy

The Helmholtz free energy (F) indicates the maximum amount of 'useful' work that can be extracted from the system at constant volume and temperature. It is defined as:

$$F = U - T * S \tag{3.19}$$

By calculating the derivative of Eq. 3.19 and substituting Eq. 3.4 into Eq. 3.19:

$$dF = -SdT - pdV + \sum_i \mu_i dN_i \tag{3.20}$$

The Helmholtz free energy F is a function of T, V, and N_i. It is preferentially used when deriving thermodynamic and mechanical properties from first principles based calculations. If the Helmholtz free energy F of a system is known, then thermodynamic properties, e.g. entropy (S), internal energy (U) and heat capacity at constant volume (C_V) of the system can be derived:

$$S = -\left(\frac{\partial F}{\partial T}\right)_{V,N_i} \tag{3.21}$$

$$U = F - T\left(\frac{\partial F}{\partial T}\right)_{V,N_i} \tag{3.22}$$

$$C_V = \left(\frac{\partial U}{\partial T}\right)_{V,N_i} = -T\left(\frac{\partial^2 F}{\partial T^2}\right)_{V,N_i} \tag{3.23}$$

3.2 Thermodynamic activity

The thermodynamic activity (a) is a measure of the 'effective concentration' of a species in a mixture. Since every substance, whichever the physical state it is (gaseous, liquid, or solid), does possess a fugacity, the activity a_i of the species i in a given thermodynamic state can be defined as being equal to the ratio of its fugacity f_i in this state and of its fugacity f_i° in the standard state [72]:

$$a_i = \frac{f_i}{f_i^\circ} \tag{3.24}$$

The value of a_i is dependent on the choice of standard state condition, or the condition that result in unit activity. By convention, the standard state condition is often chosen as the pure species i at standard T and p.

The thermodynamic activity is an important parameter for chemical reactions. For example, the SrO activity in the LSCF cathode influences the Cr poisoning of the LSCF cathode. The ZrO_2 activity in the ZrO_2-based electrolyte influences the formation of $SrZrO_3$ at the cathode/electrolyte interface. Knudsen Effusion Mass Spectrometry (KEMS) is one of the methods that can measure the activity of a certain species in a compound. The details are presented in Chap. 3.4.

3.3 FactSage

In the present thesis, the Sr related degradation issues of LSCF cathode are studied by thermodynamic calculations based on the pure substance database in FactSage. The FactSage package was introduced in 2001 and consists of a series of information, calculation and manipulation modules that enable one to access and manipulate the databases. [73] The thermodynamic databases integrated in FactSage are based on CalPhaD (Calculation of Phase Diagrams) assessments. There are two types of thermochemical databases: compound (pure substances) databases and solution databases. The compound databases contain the properties of stoichiometric compounds, either obtained from published experimental data and phase diagram optimizations or taken from standard compilations. The solutions databases contain optimized model parameters for the Gibbs energy of solution phases as functions of composition and temperature. [73]

The selection of proper databases for a given system is a prerequisite for accurate thermodynamic calculations. Based on the chosen database, one can perform a wide variety of thermochemical calculations: e.g. calculating the ΔG value of different reactions at given T, p, etc.; Calculating the conditions for multiphase or multicomponent equilibria under a large range of possible constraints through Gibbs

energy minimization scheme; Calculating, plotting and editing unary, binary, ternary and multicomponent phases diagrams in which the axes can be various combinations of T, p, V, composition, activity, chemical potential, etc..

3.4 Knudsen Effusion Mass Spectrometry

Knudsen Effusion Mass Spectrometry (KEMS) is used to identify gaseous species present above a condensed phase and to determine their vapor partial pressures up to 10 Pa with measuring temperature up 3000 K [74]. Based on the measured vapor partial pressures, the thermodynamic data of the gas phase and the condensed phase can be calculated. A simple sketch of KEMS is shown in Fig. 3.1. The working principle of KEMS is shown in Fig. 3.2.

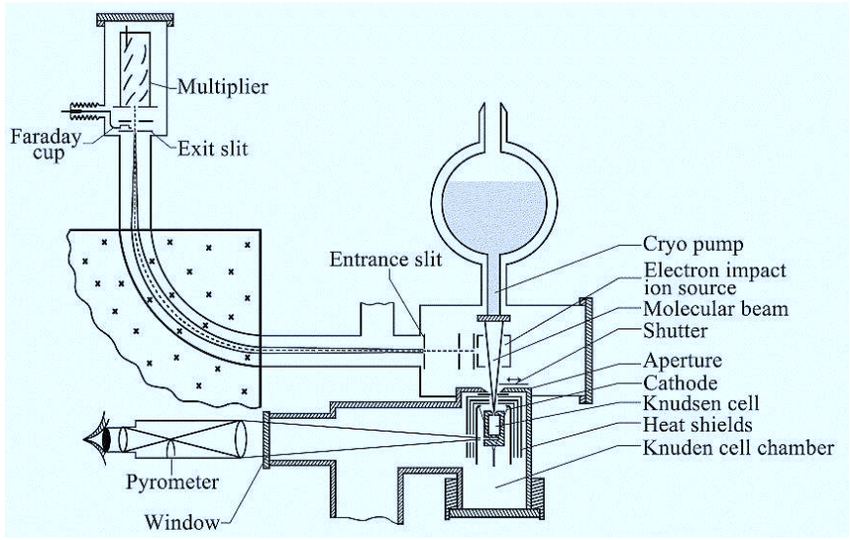

Figure 3.1: Simple sketch of KEMS [74].

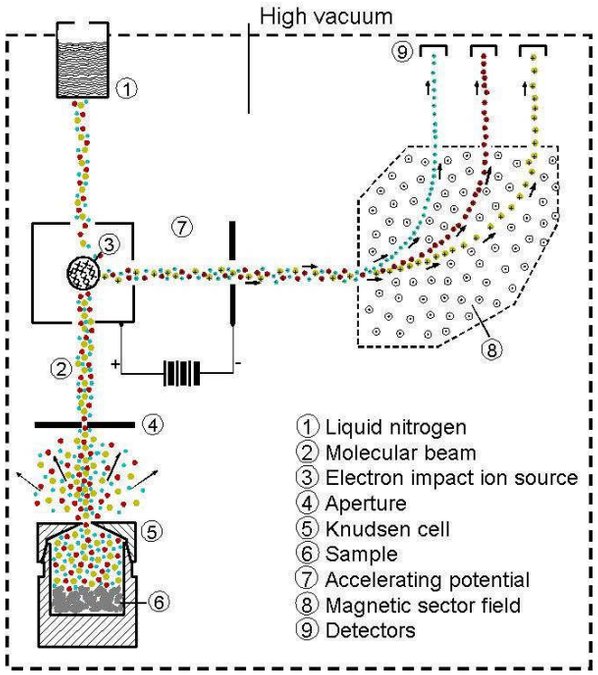

Figure 3.2: The working principle of KEMS [75].

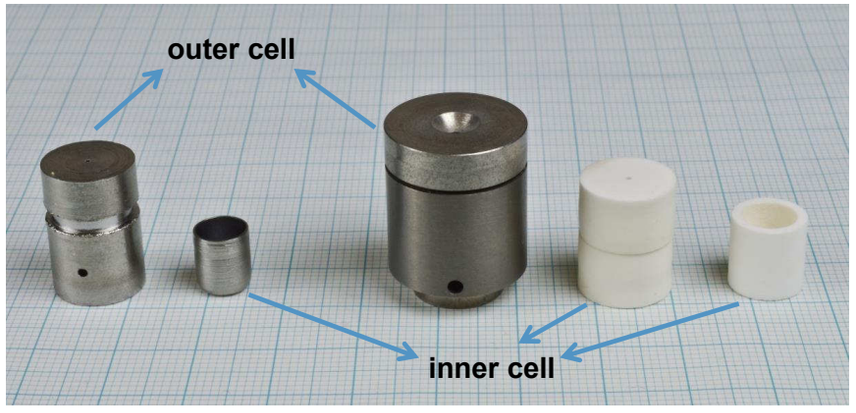

Figure 3.3: Knudsen cells.

In a KEMS measurement, the sample is located the Knudsen cells, which normally consist of an inner cell and an outer cell (Fig. 3.3). The sample will be heated by radiation or electron bombardment under vacuum to ultrahigh-vacuum conditions. The oxygen partial pressure pO_2 in the Knudsen cell is about 10^{-10} to 10^{-11} bar. The Knudsen cell has an effusion orifice (a typical diameter of 0.1 to 1 mm), which comparing to the surface of vaporizing substance, is so small that, therefore, during heating a small fraction of the molecules which evaporate from the sample will effuse through the orifice without disturbing the equilibrium in the cell. Generally, the orifice dimension must be kept to less than one tenth of the mean free path of the vapor species, over all experimental conditions. The effused molecule beams cross the shutter valve and enter the electron ionization source. The formed ions are accelerated by an electric field and then separated in the magnetic field by their mass-to-charge ratio. A secondary electron multiplier or a Faraday cup is used for measuring the intensity ion current. The temperature inside the Knudsen cell is detected by an optical pyrometer or a thermocouple. The partial pressure p_i of species i at the temperature T can be obtained from:

$$p_i = k * \frac{1}{\sigma_i} * (\sum I_i) * T \tag{3.25}$$

Where, k is the machine constant, σ_i is the ionization cross-section of the species i, $\sum I_i$ is the intensities of the ions originating from the same molecule i. T is the absolute temperature. As we are dealing with high temperatures and low pressures (10^{-11}~10^{-4} bar), the vapor can be assumed to behave as the ideal gas. Additionally, if the measurements of species i are carried out at the same condition, e.g. the same Knudsen cells, the same ion source arrangement, k/σ_i of each measurement can be treated as the same. Therefore, the thermodynamic activity of species i in a compound can be calculated by comparing the ion intensity of species i from the compound ($I_{i,compound}(T)$) with the ion intensity of species i from pure substance i ($I^{\circ}_{i,pure}(T)$):

$$a_i = \frac{p_{i,compound}}{p^{\circ}_{i,pure}} = \frac{I_{i,compound}(T)}{I^{\circ}_{i,pure}(T)} \tag{3.26}$$

For example, the thermodynamic activity of ZrO_2 (a_{ZrO_2}) in 8mol-%Y_2O_3-ZrO_2 (8YSZ) can be measured by comparing the ion intensity of ZrO_2^+ from 8YSZ with that from pure ZrO_2:

$$a_{ZrO_2}(T) = \frac{I_{ZrO_2^+}(T)}{I^\circ_{ZrO_2^+}(T)} \tag{3.27}$$

Here, $I_{ZrO_2^+}(T)$ is the ZrO_2^+ intensity from 8YSZ powder; $I^\circ_{ZrO_2^+}(T)$ is the ZrO_2^+ intensity from pure ZrO_2 powder.

3.5 First Principles Phonon Calculations

First principles phonon calculations combined with the quasi harmonic approximation (QHA) are a promising method for predicting the thermodynamic and mechanical properties of various materials at finite temperatures. Within the framework of the QHA, the Helmholtz free energy F of a system at volume V and temperature T can be described as:

$$F(T,V) = E_0(V) + F_{phonon}(T,V) + F_{el}(V,T), \tag{3.28}$$

where $E_0(V)$ is the ground state energy at T = 0 K and given volume, V, and it can be obtained through first principle calculation based on density functional theory (DFT) (the details are shown in Chap. 3.5.1). Vienna Ab initio Simulation Package (VASP) [76] is one of the codes for performing the first principle DFT calculations. $F_{phonon}(T,V)$ is the phonon contribution to the Helmholtz free energy or lattice vibration energy and it can be obtained from the phonon calculation (the details are shown in Chap. 3.5.2); $F_{el}(V,T)$ is the free energy from the electronic excitations, which are vanishingly smaller and can be neglected, as well as other contributions, provided that the temperatures are low enough [77, 78]. The Helmholtz free energy of a system $F(T,V)$ is obtained as a function of volume at specified temperatures. For each temperature, an equation of state (EOS) is fitted as function of volume, to determine the minimum values. From the curve interconnecting these minima, the equilibrium volume at each temperature can be

obtained. The volumetric thermal expansion coefficient is then calculated from the temperature dependent equilibrium volumes $V(T)$ as:

$$\beta(T) = \frac{1}{V(T)} \frac{\partial V(T)}{\partial (T)} \tag{3.29}$$

The QHA is implemented in the Phonopy [79] code. Once the Helmholtz free energy of a system $F(T,V)$ is obtained, then the Gibbs free energy of the system $G(T,p)$ at given temperature T and pressure p can also be obtained through:

$$G(T,p) = min_V[F(T,V) + pV] \tag{3.30}$$

Here, the right-hand of the equation means that, for each pair of T and p variables, the function inside the square brackets is minimized with respect to the volume V. Then the heat capacity at constant pressure can be derived through:

$$C_p(T,p) = -T \frac{\partial^2 G(T,p)}{\partial T^2} \tag{3.31}$$

3.5.1 First principles DFT calculations

First principle DFT calculations for many-body systems provide information on the electronic structure, ground state energy, stress of the system and also the force on each atom. In quantum mechanics, a wave function (ψ), which provides information about the probability amplitude of position, momentum and other physical properties of a particle, is used to describe the state of a system. For example, the wave function of a N_n-nuclei and N_e-electrons system is a function of time and the position of every particle:

$$\Psi_{total} = \Psi(\vec{r}_1, \dots, \vec{r}_n, \vec{R}_1, \dots, \vec{R}_n, t) \tag{3.32}$$

Here, $\vec{r}_i$ is the electron coordinates and $\vec{R}_i$ is the nuclei coordinates. According to the Born-Oppenheimer approximation [80], the nuclei motion and the electron motion in a molecule can be separated, i.e.:

$$\Psi_{total} = \Psi_{nucleus} \times \Psi_{electrons} \tag{3.33}$$

Since the nuclei motion is much slower than the electrons motion, the nuclei are considered to be fixed. The electron wave function depends on the nuclear positions but not on their velocities. The electrons 'feel' the Coulomb potential of the nuclei clamped at certain positions in space. The quantum mechanical problem is reduced to consider only the electrons. For this, the time-independent Schrödinger equation of electrons needs to be solved:

$$\hat{H}\Psi(\vec{r}) = E\Psi(\vec{r}) \tag{3.34}$$

Here, E is the energy eigenvalue of the system. $\hat{H}$ is the Hamiltonian and expressed as the sum of operators corresponding to the kinetic and potential energies of a system. As an example, for a single particle system, $\hat{H}$ is defined as the sum of the kinetic energy part $-\frac{\hbar^2}{2m}\nabla^2$ and the potential energy functional $V(\vec{r})$, i.e. $\hat{H} = -\frac{\hbar^2}{2m}\nabla^2 + V(\vec{r})$, where ∇^2 is the Laplacian operator, $\hbar$ is the reduced Planck constant and m is the particle's mass. Consequently, the electronic structure and the ground state energy of the system can be obtained. In first principles calculations, the main work is to solve the time-independent Schrödinger equation of electrons and to get the ground state information of the system.

Generally, there are two methods to solve the time-independent Schrödinger equation of electrons: the wave function methods and the density functional theory (DFT) methods. The wave function methods are targeting to get the wave functions of electrons, while the DFT methods are interested in the electron density. The DFT methods are computationally cheaper than the wave function methods. For example, for an N-body system, according to the wave function methods, a 3N-variable wave function is needed to be solved and is incredible computationally expensive. While in the DFT methods, the electron density is only a function of 3 coordinates. Therefore, the DFT methods are widely used in first principles calculations to investigate the ground state electronic structure of many-body systems.

3.5.1.1 Some fundamentals about Density Functional Theory

The Density Functional Theory (DFT) starts from the two Hohenberg and Kohn (H-K) theorems [81]. The first H–K theorem states that the ground state properties of a n-electron system are uniquely determined by an electronic density distribution. The second H–K theorem states that the energy of the system is a functional of the electron density; by minimizing the energy functional, the system will converge to the ground state, and subsequently the ground state energy and the ground state electron density distribution can be obtained. The H-K theorems are further developed by Walter Kohn and Lu Jeu Sham [82], who converted the problem of n interacting electrons in a static external potential into a problem of n non-interacting electrons moving in an effective potential. The effective potential (V_{eff}) is defined as a sum of the external potential (V_{ext}, e.g. the interaction with nuclei), the electron-electron repulsive potential (so called Hartree term, V_H) and the exchange-correlation potential (V_{xc}):

$$V_{eff}(\vec{r}) = V_{ext}(\vec{r}) + V_H(\vec{r}) + V_{xc}(\vec{r}) \tag{3.35}$$

For each single-electron orbital, ψ_i, which has orbital energy ϵ_i, the Eq. 3.36 is valid:

$$\left(-\frac{\hbar^2}{2m}\nabla^2 + V_{eff}(\vec{r})\right)\psi_i(\vec{r}) = \epsilon_i\psi_i(\vec{r}) \tag{3.36}$$

Eq. 3.36 is named as the Kohn-Sham equation, which is similar as the one-electron *Schrödinger equation and* must be solved with certain approximations. The density functional of the original n-electron system is then calculated by summing the fictitious density functional of each one-electron system:

$$\rho(\vec{r}) = \sum_i^n |\psi_i(\vec{r})|^2 \tag{3.37}$$

The electron density $\rho(\vec{r})$ of the original n-electron system can only be obtained by an iterative self-consistent way. It starts with an initial guess of the $\rho(\vec{r})$, then the effective potential is calculated. Afterwards, according to Eq. 3.36, a set of orbitals ψ_i and orbital energies ϵ_i are derived. Subsequently, a new electron density $\rho'(\vec{r})$ can be calculated. The process is iterated until convergence is reached, i.e. the difference between the

energy of two subsequent iterations ($|E[\rho(\vec{r})] - E[\rho'(\vec{r})]|$) drops below a specific threshold.

3.5.1.2 Exchange-correlation potential (V_{xc})

The Exchange-correlation potential (V_{xc}) in Eq. 3.35 is unknown and it is the product of the derivative of the exchange-correlation energy ($E_{xc}[\rho(\vec{r})]$) with respect to $\rho(\vec{r})$. Some approximation functional are introduced to describe $E_{xc}[\rho(\vec{r})]$. Generally, there are two classes of approximation in use: the local density approximation (LDA) and the general gradient approximation (GGA). The LDA assumes that a general inhomogeneous electron system is locally homogeneous and only the local electron density affects the $E_{xc}[\rho(\vec{r})]$. Therefore, $E_{xc}[\rho(\vec{r})]$ is calculated by integrating the locally homogeneous density function $\rho(\vec{r})$ multiplied with the homogeneous energy density $\epsilon_{xc}^{LDA}[\rho(\vec{r})]$ over the whole volume:

$$E_{xc}^{LDA}[\rho(\vec{r})] = \int \rho(\vec{r})\epsilon_{xc}^{LDA}[\rho(\vec{r})]dr \tag{3.38}$$

The LDA method can be improved as the generalized gradient approximation (GGA) which attempts to incorporate the effects of inhomogeneity by including the electron density gradient:

$$E_{xc}^{GGA}[\rho(\vec{r})] = \int \rho(\vec{r})\epsilon_{xc}^{GGA}[\rho(\vec{r}), \nabla\rho(\vec{r})]dr \tag{3.39}$$

$\epsilon_{xc}^{GGA}[\rho(\vec{r}), \nabla\rho(\vec{r})]$ is the inhomogeneous energy density and one of the mostly used forms for it is proposed by Perdew, Burke, and Enzerhof (PBE) [83], which is available in the VASP code and is known for its general applicability and gives rather accurate results for a wide range of systems.

3.5.1.3 Electrons in a periodic solid

In a perfect crystal, the ions are arranged in a periodic array that is describe by Bravais lattice vectors $\vec{R}$. As a simplification, the independent electrons can be treated as experiencing a periodic potential $V(\vec{r})$ imposed by nuclei. The time-independent Schrödinger equation for a single independent electron can be written as:

$$\hat{H}\psi(\vec{r}) = \left(-\frac{\hbar^2}{2m}\nabla^2 + V(\vec{r})\right)\psi(\vec{r}) = \epsilon\psi(\vec{r}) \tag{3.40}$$

with $V(\vec{r}) = V(\vec{r} + \vec{R})$. The independent electrons which obey the one electron Schrödinger equation for a periodic potential are called Bloch electrons and obey Bloch's theorem:

$$\psi_{n\vec{k}}(\vec{r}) = e^{i\vec{k}\vec{r}}u_{n\vec{k}}(\vec{r}) \tag{3.41}$$

Here, $\psi_{n\vec{k}}(\vec{r})$ is the wave function of the independent electron and $\psi_{n\vec{k}}(\vec{r})$ is the product of a plane wave $e^{ik\vec{r}}$ multiplying a periodic function $u_{n\vec{k}}(\vec{r})$, and $u_{n\vec{k}}(\vec{r}) = u_{n\vec{k}}(\vec{r} + \vec{R})$. $\vec{\mathrm{k}}$ is arbitrary wave vector for the electron that is obtained for a constant potential. n is the band index and corresponds to the appearance of independent eigenstates of different energies with the same $\vec{k}$. The Bloch's theorem can also be expressed as:

$$\psi_{n\vec{k}}(\vec{r} + \vec{R}) = e^{ik\vec{R}}\psi_{n\vec{k}}(\vec{r}) \tag{3.42}$$

This means that any function $\psi_{n\vec{k}}(\vec{r})$ that is a solution to the Schrödinger equation of the problem, differs only by a phase factor $e^{ik\vec{R}}$ between equivalent positions in the lattice. The probability of finding an electron is the same at any equivalent position in the lattice, i.e. $\left|\psi_{n\vec{k}}(\vec{r} + \vec{R})\right|^2 = \left|\psi_{n\vec{k}}(\vec{r})\right|^2$. By considering the reciprocal space, a reciprocal lattice vector is defined as:

$$\vec{G} \cdot \vec{R} = 2\pi m \tag{3.43}$$

with m is an integer. If Eq. 3.41 is a Bloch wave solving the Schrödinger equation of the problem, then the following function is also a solution.

$$\psi_{n,\vec{k}+\vec{G}}(\vec{r}) = e^{i(\vec{k}+\vec{G})\vec{r}}u_{n,\vec{k}+\vec{G}}(\vec{r}) \tag{3.44}$$

Since $\psi_{n\vec{k}}(\vec{r})$ is identical with $\psi_{n,\vec{k}+\vec{G}}(\vec{r})$, any value of $\vec{k}$ that is outside the first Brillouin zone can be reduced to the first Brillouin zone, i.e. $\vec{k}$ can be restricted to the first Brillouin zone. In addition:

$$E(\vec{k}) = E(\vec{k} + \vec{G}) \tag{3.45}$$

which means any reciprocal lattice point can serve as the origin of the $E(\vec{k})$ function. The Bloch theorem transfers the problem of an infinite number of electrons in a solid into a problem of a finite number of electrons in the unit cell (or half of this number if the electrons are spin degenerate) at a finite number of k-points chosen as to appropriately sampling the first Brillouin zone.

3.5.1.4 Brillouin zone sampling

The first Brillouin zone can be mapped out by a continuous set of k-points, throughout that region of reciprocal space. The occupied states at each k-point contribute to the ground state properties, such as ground state energy, of the many-body system. Since the set of k-points is dense, there are an infinite number of k-points in the Brillouin zone at which the wave functions must be calculated. However, the electron wave functions at k-points are very close together that will be almost identical. Hence, it is possible to represent them by a single k-point over a region of k space. [84] Therefore, to obtain accurate ground state properties, efficient methods should be used to carefully choose a finite set of k-points to characterize the shape of the reciprocal space of the cell. The Monkhorst and Pack scheme [85] is one of the common methods that is implemented in the VASP code. According to the Monkhorst and Pack method, a uniform mesh of k-points is generated along the three reciprocal lattice vectors. When generating the k-points mesh, it is necessary to consider the crystal shape, i.e. the shape of the first Brillouin zone. If the first Brillouin zone has a larger dimension in one direction, more k-points should be placed along that direction to maintain the same k-points density in all locations of the first Brillouin zone. Before the calculation, it is crucial to test the convergence of the results with respect to the number of k-points.

3.5.1.5 Energy cut off

According to the Bloch's theorem (Eq. 3.41), $u_{n\vec{k}}(\vec{r})$ is a periodic function, by expanding it in terms of a Fourier series in reciprocal space yields:

$$u_{n\vec{k}}(\vec{r}) = \sum_{\vec{G}}^{|\vec{G}|<G_{max}} c_{i,\vec{G}} * e^{i\vec{G}\vec{r}} \quad (3.46)$$

Here, $\vec{G}$ is a reciprocal lattice vectors and $c_{i,\vec{G}}$ are the Fourier coefficients. The electron wave function can therefore be written as:

$$\psi_{n\vec{k}}(\vec{r}) = \sum_{\vec{G}}^{|\vec{G}|<G_{max}} c_{i,\vec{G}+\vec{k}} * e^{i(\vec{G}+\vec{k})\vec{r}} \quad (3.47)$$

The electron wave function $\psi_{n\vec{k}}(\vec{r})$ at each k-point is now expressed in terms of a discrete plane wave basis set. In principle, this Fourier series is infinite. However, on one hand, the Fourier coefficient $c_{i,\vec{G}+\vec{k}}$ becomes smaller and smaller and on the other hand the kinetic energy of the plane wave is proportional to $\left|\vec{G}+\vec{k}\right|^2$. Therefore, there is a specific limit that the $\left|\vec{G}+\vec{k}\right|^2$ becomes so large that the Fourier coefficients are negligible and the Fourier series is thus truncated. An energy cut-off is therefore introduced as $E_{cut} = \frac{1}{2}{G_{max}}^2$, so that only the plane waves with energies less than this cut-off are included in the DFT calculation. The energy cut-off should be large enough to give accurate results. Therefore, in the calculations, first, a series of increasing energy cut-offs should be tried until the properties we are interested in have converged.

3.5.1.6 Pseudopotential

The atomic nucleus induces a strong Coulomb potential that causes the electron wave function to oscillate rapidly close to the atomic nucleus, which means that a very large energy cut-off is needed. Additionally, in solid, chemical bonds between atoms are formed by sharing the valence electrons. When the bond is formed, wave function of valence electrons change significantly, while wave function of core electrons change only slightly. Therefore, pseudopotential is introduced to describe the complicated effects of the core electrons and its nucleus that act on the valence electrons. Hence, in the Hamiltonian the Coulombic potential term ($V_{ext}(\vec{r})$) is replaced by a modified effective potential term, which is the pseudopotential (Fig. 3.4).

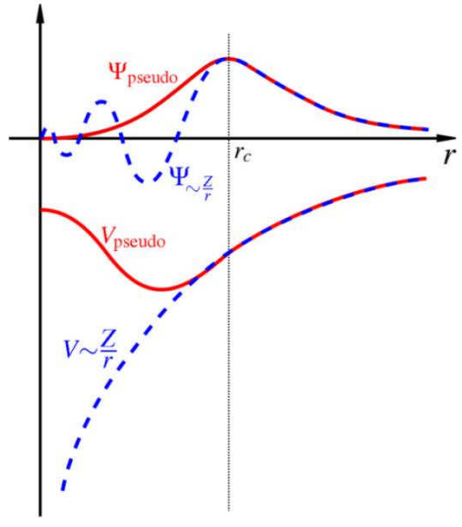

Figure 3.4: Illustration of the all-electrons potential (dash line) and the pseudopotential (solid line) and their corresponding wave functions. [86]

The pseudopotential removes the strong oscillation of the wave function near the core and, meanwhile, reduces the number of electrons that need to be treated, thus less plain waves are required. Under the concept of the pseudopotential, the largest contribution to the total energy is fixed and comes from the core electrons, so it does not contribute to bonding but affects numerical convergence and accuracy. The projector-augmented wave (PAW) method [87] is one of the forms of pseudopotential used in the first principle DFT calculations and implemented in the VASP code.

3.5.2 Phonon calculation

In the first principle DFT calculations, the nuclei are fixed. Therefore, the energy obtained for a system is the ground state energy with respect to 0 K. If we want to get the energy of a system at finite temperatures, the lattice vibration, i.e. phonons, should be incorporated. Knowledge of phonon characteristics (e.g. phonon frequencies and eigenvectors) is necessary to describe mechanical and thermodynamic properties of a

system at finite temperatures. From the first principle DFT calculation, besides electronic structure information, ground state energy and the stress of the system, we can also get the force on each atom. If an atom in a crystal is displaced from its equilibrium position, the forces on all atoms raise. Analysis of the forces associated with a systematic set of displacements provides a series of phonon frequencies. This is the so called finite displacement method in phonon calculation and implemented in the PHONOPY [79] code.

3.4.2.1 Finite displacement method

In the finite displacement method, a fully relaxed structure is required as input to generate supercells with symmetry distinct atomic displacements. The generated supercells are acting as inputs for the first principle DFT calculations in VASP code to calculate the atomic forces as a response to the displacements. The force constants $\Phi_{\alpha\beta}(jl, j'l')$ are estimated by:

$$\Phi_{\alpha\beta}(jl, j'l') \cong -\frac{F_\beta\left(j'l', \Delta r_\alpha(jl)\right) - F_\beta(j'l')}{\Delta r_\alpha(jl)} \tag{3.48}$$

where, α, β ,…, are the Cartesian indices; j, j',…, are the indices of atoms in a unit cell; and l, l', …, are the indices of unit cells. Therefore, $\Delta r_\alpha(jl)$ means a finite displacement of j atom in l unit cell with the direction α. $F_\beta\left(j'l', \Delta r_\alpha(jl)\right)$ are the forces on atoms with the finite displacement $\Delta r_\alpha(jl)$ and usually $F_\beta(j'l') \equiv 0$. Within the model of treating the atoms as harmonic oscillators ($\omega^2 = \frac{k}{m}$, with k is the force constant of the spring and m is the mass of the oscillator), the calculated force constants are used to calculate the eigen frequencies of each atomic oscillator and the corresponding eigenvectors. Since calculations on condensed matter often use periodic boundary conditions, the supercell must be large enough to reach the convergence with respect to the supercell size which is due to interactions with atoms/ions from the neighboring cell.

3.5.2.2 Thermal properties of phonons

Each phonon mode is characterized by the wave vector $\vec{k}$, frequency $\omega_{\vec{k}}$ and energy $E_{n,\vec{k}} = \hbar\omega_{\vec{k}}\left(n+\frac{1}{2}\right), n = 1, 2, \dots, n$. The probability to find the mode $\vec{k}$ having n phonons is:

$$P_{\vec{k}}(n) = \frac{1}{Z_{\vec{k}}} exp\left(-\frac{E_{n,\vec{k}}}{k_B T}\right) \tag{3.49}$$

Here, $Z_{\vec{k}}$ is partition function; k_B is the Boltzmann constant; T is the absolute temperature. Since the total probability to find mode $\vec{k}$ having n phonons is equal to unit, i.e.:

$$1 = \sum_{n=0}^{\infty} P_{\vec{k}}(n) \ , \tag{3.50}$$

the partition function can be calculated as:

$$Z_{\vec{k}} = \sum_n exp\left(-\frac{\hbar\omega_{\vec{k}}\left(\frac{1}{2}+n\right)}{k_B T}\right) = \frac{\exp\left(-\hbar\omega_{\vec{k}}/2k_B T\right)}{1-exp\left(-\hbar\omega_{\vec{k}}/k_B T\right)} \tag{3.51}$$

The average phonon number for mode $\vec{k}$ can be then calculated as:

$$\langle n_{\vec{k}} \rangle = \sum_{n=0}^{\infty} n P_{\vec{k}}(n) = \frac{1}{exp\left(\hbar\omega_{\vec{k}}/k_B T\right)-1} \tag{3.52}$$

The Helmholtz free energy of mode $\vec{k}$ is:

$$F_{\vec{k}} = -k_B T ln Z_{\vec{k}} = \frac{1}{2}\hbar\omega_{\vec{k}} + k_B T ln\left[1 - exp\left(-\hbar\omega_{\vec{k}}/k_B T\right)\right] \tag{3.53}$$

The phonon contribution to the Helmholtz free energy of the system is the sum of the free energy of all modes:

$$F_{phonon} = \sum_{\vec{k}} F_{\vec{k}} \tag{3.54}$$

Then the entropy of the system can be calculated according to Eq. 3.21. The total internal energy of the system is:

$$E_n = \sum_{\vec{k}} E_{n,\vec{k}} = \sum_{\vec{k}} \hbar\omega_{\vec{k}} \left(\frac{1}{exp\left(\hbar\omega_{\vec{k}}/k_B T\right)-1} + \frac{1}{2}\right) \tag{3.55}$$

Then, the heat capacity of the system at constant volume is given by:

$$C_V = \left(\frac{\partial E_n}{\partial T}\right)_V = \sum_{\vec{k}} k_B \left(\frac{\hbar\omega_{\vec{k}}}{k_B T}\right)^2 \frac{exp\left(\hbar\omega_{\vec{k}}/k_B T\right)}{\left[exp\left(\hbar\omega_{\vec{k}}/k_B T\right)-1\right]^2} \quad (3.56)$$

3.5.2.3 Quasi harmonic approximation

By changing volume, phonon properties vary since the crystal potential is an anharmonic function of volume. The ‘quasi harmonic approximation’ means this volume dependence of phonon properties, but the harmonic approximation is simply applied at each volume [79]. The ‘quasi harmonic approximation’ is used to calculate the thermal expansion of the crystal, and the details have been shown at the beginning of Chap. 3.5.

4. Sr-related degradation issues of the LSCF cathode [1]

4.1 Thermodynamic aspects of Cr poisoning of the LSCF cathode

Cr poisoning of the LSCF cathode is considered as a two-step process: First, Cr species evaporation and, second, Cr species deposition. Thermodynamic aspects of Cr poisoning of the LSCF cathode are studied by means of FactSage [73] calculations. The calculation consists of two parts. First, the equilibrium partial pressures of possible gaseous Cr species over Cr_2O_3(s) are calculated and the influencing factors are discussed. Second, the deposition of CrO_3(g), i.e. the reaction between CrO_3(g) and SrO, is analyzed and discussed.

4.1.1 Cr species evaporation

4.1.1.1 Thermodynamic calculation

Hexavalent chromium species CrO_3 and $CrO_2(OH)_2$ are the dominating gaseous Cr species in air without and with humidity, respectively [10]. The corresponding chemical reactions are:

$$Cr_2O_3\,(s) + \frac{3}{2}O_2\,(g) \leftrightharpoons 2CrO_3\,(g) \qquad (4.1)$$

[1] Section content (Chap.4.1 & Chap.4.2) published. X. Yin et al., Int. J. Appl. Ceram. Technol., 15:380-390, 2018. https://doi.org/10.1111/ijac.12809

$$Cr_2O_3(s) + \frac{3}{2}O_2\,(g) + 2H_2O\,(g) \leftrightharpoons 2CrO_2(OH)_2\,(g) \quad (4.2)$$

The equilibrium partial pressures $pCrO_3$ and $pCrO_2(OH)_2$ over pure Cr_2O_3(s) are calculated. The calculation parameters are listed in Table 4.1. Two different oxygen partial pressures are considered: normal air condition: pO_2=0.21 bar and oxygen deficient condition: pO_2=10^{-3} bar. Low H_2O contents can be expected, if dry air is used as the cathode gas for SOFC stack operation. Typical temperatures for relevant SOFC operation are assumed to be in the range from 600 °C to 1000 °C.

Table 4.1: Calculation parameters for the $pCrO_3$ and $pCrO_2(OH)_2$.

Activity of Cr_2O_3	a = 1 (pure Cr_2O_3)
pO_2 / bar	0.21 and 10^{-3}
pH_2O / bar	0.03, 10^{-3} and 10^{-5}
T / °C	600 to 1000

The thermodynamic data for CrO_3(g) and $CrO_2(OH)_2$(g) are available in two pure substances databases, SGPS and FactPS, in FactSage [73]. For CrO_3(g), the two databases are consistent, such that the difference between the calculated partial pressures $pCrO_3$ can be neglected (Fig. 4.1a). According to the work of C. Gindorf et al. [88, 89], the calculated $pCrO_3$ is comparable with experimental measurements. However, for the calculated $pCrO_2(OH)_2$ (Fig. 4.1b) there is about three order of magnitude difference between the SGPS database and the FactPS database (based on B. B. Ebbinghaus [90]). According to M. Stanislowski [91] and C. Gindorf et al. [88, 89], who measured $pCrO_2(OH)_2$ at equilibrium conditions by the transpiration method, the measured $pCrO_2(OH)_2$ values are within 1 to 1.5 orders of magnitude less than the calculated $pCrO_2(OH)_2$ data which is based on the FactPS database. As an estimate, a modification for $pCrO_2(OH)_2$ is performed by multiplying the calculated $pCrO_2(OH)_2$ which is based on the FactPS database with the factor 0.1:

$$pCrO_2(OH)_{2\_modi} = 0.1 * pCrO_2(OH)_{2\_FactPS} \quad (4.3)$$

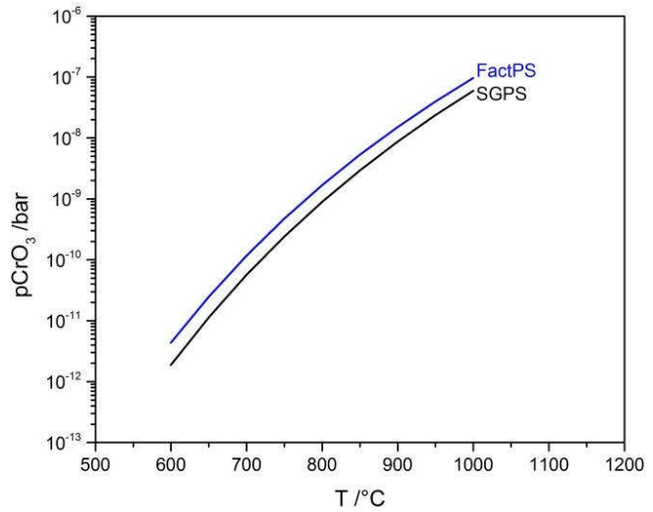

(a) $pCrO_3$ above pure Cr_2O_3(s) when pO_2=0.21 bar.

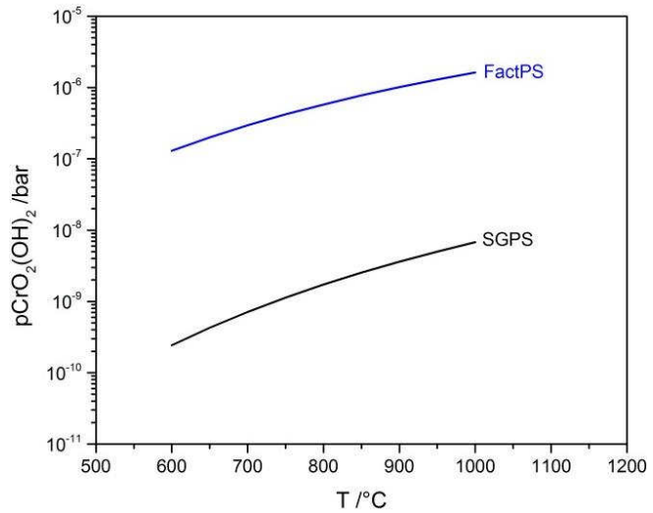

(b) $pCrO_2(OH)_2$ above pure Cr_2O_3(s) when pO_2=0.21 bar and pH_2O=0.03 bar.

Figure 4.1: Comparison of $pCrO_3$ and $pCrO_2(OH)_2$ between the SGPS database and the FactPS database.

4.1.1.2 Results and discussion

The obtained values $pCrO_2(OH)_2$_modi (dashed line) are compared with the calculated $pCrO_3$ (solid line) at three different pH_2O conditions: 0.03 bar (Fig. 4.2a), 10^{-3} bar (Fig. 4.2b) and 10^{-5} bar (Fig. 4.2c). Although uncertainty exists on the precise value of $pCrO_2(OH)_2$, this is not critical, as the idea here is not to predict the absolute value of $pCrO_2(OH)_2$ by thermodynamic calculation, but to understand the influencing factors of $pCrO_3$ and $pCrO_2(OH)_2$. When pH_2O=0.03 bar at SOFC operation temperature (e.g. 700°C) $CrO_2(OH)_2$ is the dominant gaseous Cr species. With decreasing pH_2O, $pCrO_2(OH)_2$ drops as well. If the humidity of the cathode gas is below a certain level, CrO_3 becomes the dominant gaseous Cr species. $pCrO_3$ has a stronger temperature dependence than $pCrO_2(OH)_2$. Therefore, to minimize the Cr species evaporation, dry air is optimal as the cathode gas and lower operation temperatures of SOFCs are beneficial from a thermodynamic point of view.

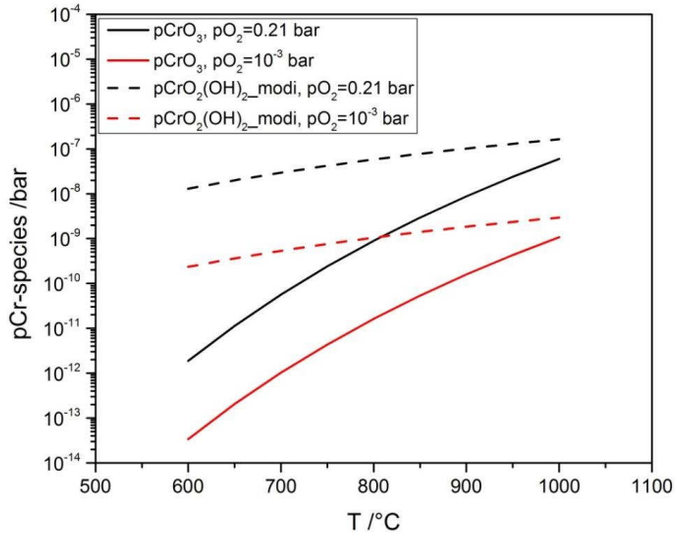

(a) pH_2O=0.03 bar

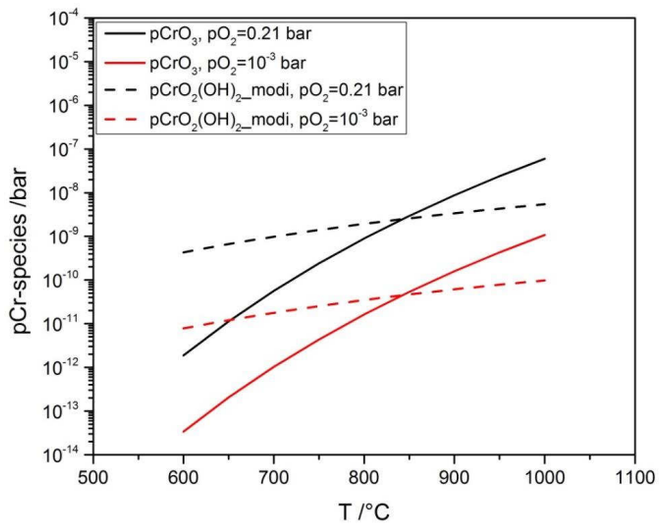

(b) $pH_2O=10^{-3}$ bar

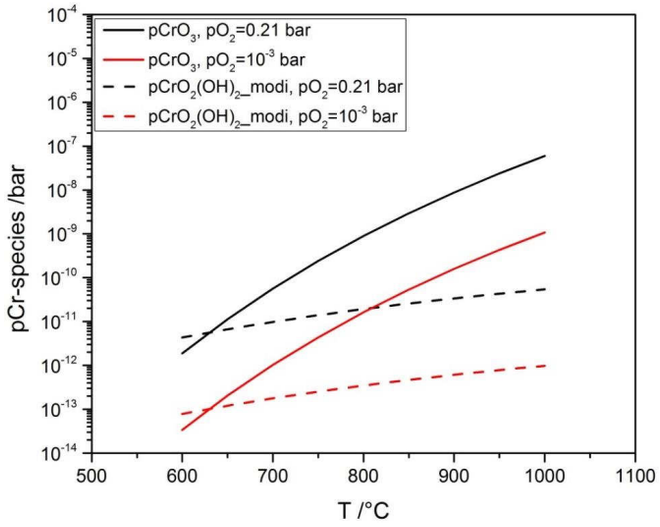

(c) $pH_2O=10^{-5}$ bar

Figure 4.2: Equilibrium partial pressures of CrO_3 and $CrO_2(OH)_2$ above pure Cr_2O_3(s) at three different pH_2O.

4.1.2 Cr species deposition

4.1.2.1 Thermodynamic calculation

SrO from the LSCF cathode is a preferential reaction partner for the evaporated Cr species. It takes Cr from the gas phase and forms Sr-Cr-O secondary phases preferentially at the cathode surface. According to the SGPS database in FactSage [73], there are four different Sr-Cr-O compounds. As an example, dry air condition is considered, which means that CrO_3(g) is the dominant gaseous Cr species. The possible reactions between SrO and CrO_3(g) are:

$$SrO(s) + CrO_3(g) \leftrightharpoons SrCrO_4(s) \tag{4.4}$$

$$SrO(s) + CrO_3(g) \leftrightharpoons SrCrO_3(s) + \frac{1}{2}O_2(g) \tag{4.5}$$

$$SrO(s) + \frac{2}{3}CrO_3(g) \leftrightharpoons \frac{1}{3}Sr_3Cr_2O_8(s) + \frac{1}{6}O_2(g) \tag{4.6}$$

$$SrO(s) + \frac{1}{2}CrO_3(g) \leftrightharpoons \frac{1}{2}Sr_2CrO_4(s) + \frac{1}{4}O_2(g) \tag{4.7}$$

By comparing the Gibbs energy change (ΔG value) of each reaction, the Sr-Cr-O compound with the most negative formation enthalpy ΔG is the most stable phase. An isothermal phase stability diagram, which indicates the most stable Sr-Cr-O compound as function of the oxygen partial pressure (pO_2) and CrO_3 partial pressure ($pCrO_3$) can be obtained. The thermodynamic data of all the compounds are based on the SGPS database. The calculation parameters are listed in Table 4.2.

Table 4.2: Calculation parameters for phase stability diagrams of Sr-Cr-O.

Activity of SrO	1 and 10^{-5}
pO_2 /bar	10^{-12} to 1
$pCrO_3$ /bar	10^{-24} to 10^{-10}
T /°C	700 and 800

In the calculation, pO_2 is considered from the extreme deficient situation 10^{-12} bar to 1 bar. Although in a real SOFC stack the extreme situations is hardly reached, the idea

here is to understand how pO_2 influences the reaction between $CrO_3(g)$ and SrO, and to understand the formation of Sr-Cr-O at the interface between LSCF and the electrolyte. $pCrO_3$ is assumed to range from 10^{-24} to 10^{-10} bar. At 700°C and pO_2=0.21 bar the equilibrium partial pressure of CrO_3 over pure Cr_2O_3 (aCr_2O_3=1) is about 10^{-10} bar. However, in a SOFC stack, the source which supplies gaseous Cr species is not pure Cr_2O_3, which means aCr_2O_3<1. Meanwhile, protective coatings are preferential applied on the interconnect [11-13]. $pCrO_3$ should therefore be lower than the calculated equilibrium value. Hence, it is assumed to be in a range from 10^{-24} to 10^{-10} bar, depending of the gas tightness of the protective layers. Two different activities of SrO are considered. If SrO segregates from the LSCF cathode, which is a frequent phenomenon that occurs at the LSCF cathode, the thermodynamic activity of SrO is equal to 1 (aSrO=1). If there is no SrO segregation, according to W. W. Zhang [92] at 700°C, aSrO is about 10^{-5} and at 800°C, aSrO is about $5*10^{-5}$.

4.1.2.2 Results and discussion

The isothermal phase stability diagram for the reaction between SrO and $CrO_3(g)$ at 700°C with aSrO=1 (solid line) and aSrO=10^{-5} (dashed line) is shown in Fig. 4.3. If SrO segregates from the LSCF cathode (aSrO=1), four different Sr-Cr-O compounds, $SrCrO_4$, $SrCrO_3$, $Sr_3Cr_2O_8$ and Sr_2CrO_4, may form depending on different values of pO_2 and $pCrO_3$. If there is no SrO segregation (aSrO=10^{-5}), depending on different values of pO_2 and $pCrO_3$, hence only $SrCrO_3$ and $SrCrO_4$ can be formed. The reaction between SrO and $CrO_3(g)$ depends on pO_2, $pCrO_3$, temperature and aSrO. If a humid cathode gas is considered, then $CrO_2(OH)_2(g)$ will be the dominating Cr species. Therefore, the reaction between SrO and $CrO_2(OH)_2(g)$ additionally depends on pH_2O.

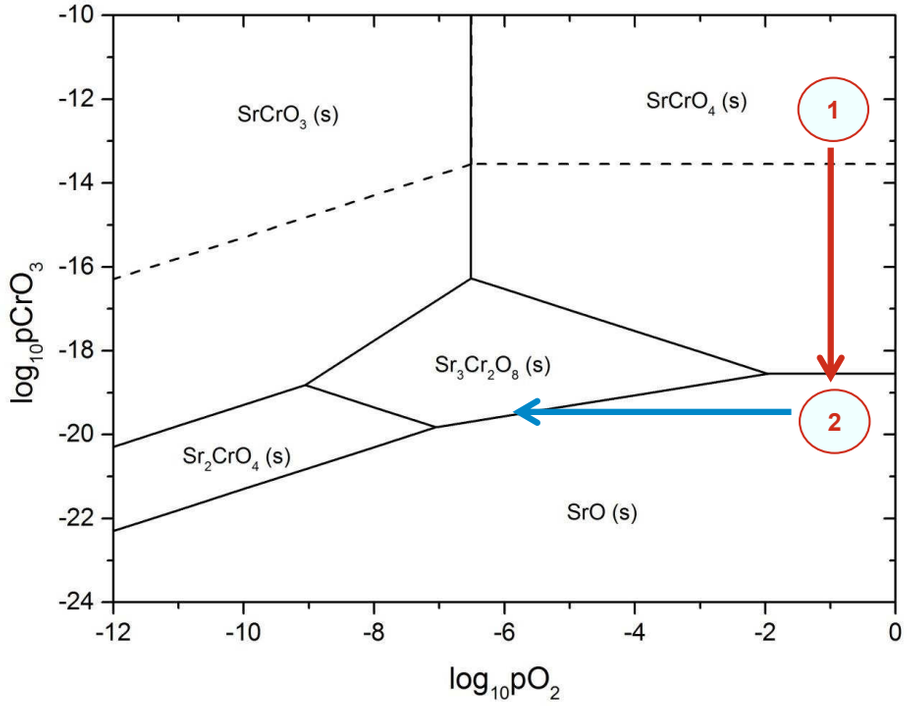

Figure 4.3: Isothermal phase stability diagram for the reaction between SrO and CrO_3(g) at T=700°C as a function of pO_2 and $pCrO_3$. The solid line indicates the case that aSrO=1. The dashed line indicates the case that aSrO=10^{-5}.

At the cathode surface, there is enough oxygen supply from the cathode gas, and if there is sufficient CrO_3(g) evaporating from the interconnect, $SrCrO_4$ is the most stable Sr-Cr-O compound, which is consistent with previous observations [7, 54]. However, in the bulk cathode or at the cathode/electrolyte interface the local value of pO_2 drops due to the oxygen reduction. If aSrO is high enough the formation of $SrCrO_3$ or $Sr_3Cr_2O_8$ or Sr_2CrO_4 may become possible. This isothermal phase stability diagram (the case aSrO=1) was applied to explain Cr species deposition under real stack operation conditions in the co-work with A. Beez [93]. The SOFC stack, which had porous protective coating on the interconnect (Crofer® 22 APU), LCC10 cathode contact layer, $La_{0.58}Sr_{0.4}Co_{0.2}Fe_{0.8}O_{3-\delta}$ cathode, porous GDC layer and 8YSZ electrolyte, was operated

at 700 °C for 1240 h with dry, synthetic air as cathode gas. The current density was raised sequentially from 0.5 A cm^{-2} during the first 240 h of operation to 0.75 A cm^{-2} for a further 1000 h of operation. After operation, deterioration was detected in the LSCF cathode, where approximately the last 10 µm facing to the GDC barrier layer. Cr was detected at the LSCF cathode surface and additionally at the LSCF/GDC interface (Fig. 4.4).

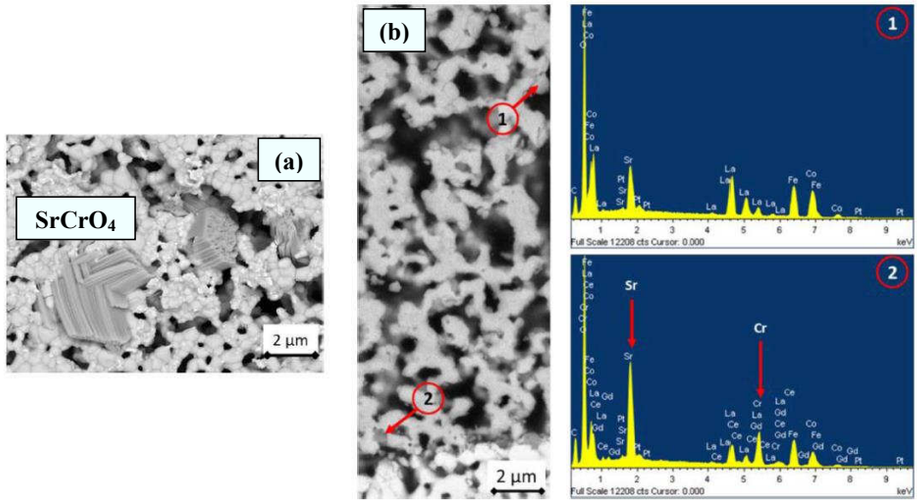

Figure 4.4: Cr depostions in the co-work of A. Beez [93]: a) at top surface of LSCF cathode and b) at LSCF/GDC interface.

As a reference, a stack with the same design was operated at 700 °C for 1700 h with constant current density 0.5 A cm^{-2}. In the reference stack, no cathode deterioration was overserved and there was no Cr-deposition at LSCF/GDC interface. Back to Fig. 4.3, since SrO prefers to segregate on the surface of the LSCF cathode [48-52], the case aSrO=1 (soild line) is considered. At the LSCF cathode surface, there is sufficient O_2 from the cathode gas. The evaporated CrO_3 will react with SrO and form $SrCrO_4$ (e.g. at point 1). Due to this reaction, the CrO_3 content in the air that enters the bulk cathode decreases, i.e. $pCrO_3$ drops. When $pCrO_3$ drops below a critical value, the reaction between SrO and CrO_3 becomes unfavorable (e.g. at point 2). It is expected to be the

situation in the bulk cathode. Due to the reduction of oxygen, this may originate from the increase of current density, the local pO_2 in the cathode decreases. Since some deterioration was detected in the LSCF cathode, according to Kuhn et al. [94], $La_{0.6}Sr_{0.4}Co_{0.2}Fe_{0.8}O_{3-\delta}$ starts to decompose at pO_2 of about 10^{-8} bar, the local pO_2 in the deterioration area should be much lower. As shown by the blue arrow in Fig. 4.3, by dropping of the local pO_2, the reaction between CrO_3 and SrO takes place again. Sr_2CrO_4 or $Sr_3Cr_2O_8$ may be the reaction products.

According to N. H. Menzler et al. [55], they performed a stack test for anode-supported solid oxide fuel cells with Crofer® 22 APU as interconnect, $La_{0.58}Sr_{0.4}Co_{0.2}Fe_{0.8}O_{3-\delta}$ cathode, dense GDC diffusion barrier layer, special thin-film 8YSZ electrolyte (~1 µm). After operation at 700 °C for 1300 h and subsequent at 600 °C for 1200 h under a constant current density 0.5 A cm^{-2}, Cr was detected both at the top surface of LSCF cathode and at the LSCF/GDC interface (Fig. 2.5). Similar to the work in [93], the Cr-deposition at the LSCF/GDC interface in the work [55] might also be explained by dropping of local pO_2 at the LSCF/GDC interface and subsequently facilitating the reaction between gaseous Cr species and the segregated SrO. In the work [55], protons might diffuse from the anode side to the cathode side through the thin-film 8YSZ electrolyte. The protons take the oxygen at the LSCF/GDC interface and result in the drop of the local pO_2 at the LSCF/GDC interface. Subsequently, the reaction between SrO and Cr species becomes favorable. The proton conductivity of YSZ has been reported elsewhere [95-97]. The proton diffusion in this type of thin-film 8YSZ electrolyte is just a hypothesis and will need further research.

The reaction between SrO and Cr species is also influenced by temperature. The isothermal phase stability diagrams for the reaction between SrO (aSrO=1) and CrO_3(g) are compared at 700 °C (black line) and 800 °C (red line). As shown in Fig. 4.5, four different Sr-Cr-O compounds may form depending on different values of pO_2 and $pCrO_3$. The reactions between SrO(s) and CrO_3(g) are favorable at low temperature. As an example, if pO_2=0.21 bar and $pCrO_3=10^{-17}$ bar, at 700 °C SrO reacts with CrO_3(g) and

forms $SrCrO_4$, while, at 800 °C there is no reaction between SrO(s) and CrO_3(g), SrO is the most stable phase.

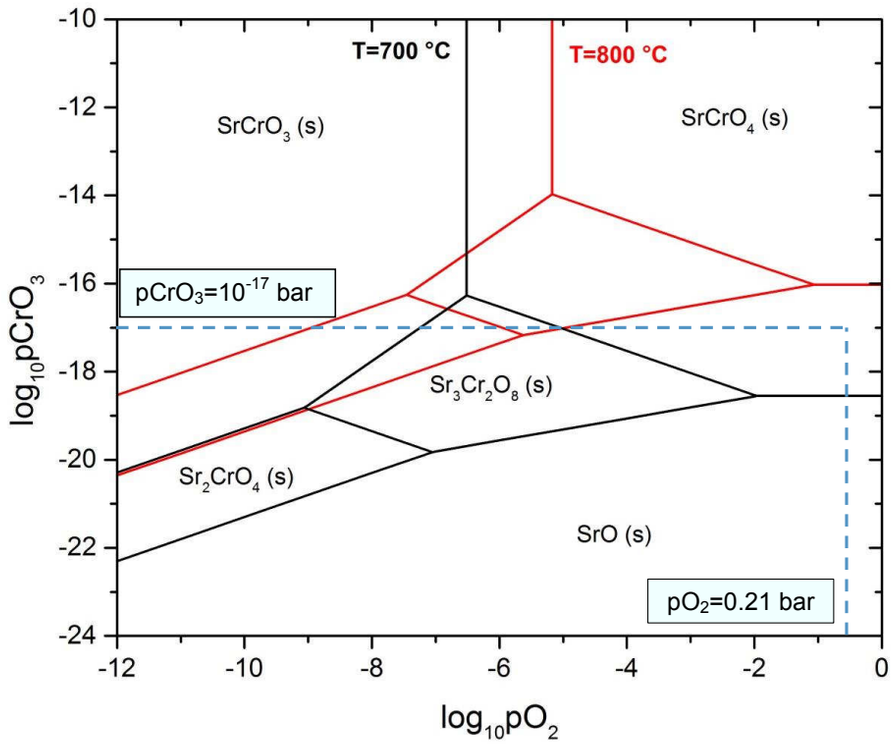

Figure 4.5: Isothermal phase stability diagrams for the reaction between SrO and CrO_3(g) at 700 °C (black) and 800 °C (red) as a function of pO_2 and $pCrO_3$ with aSrO=1.

4.2 Formation of volatile Sr species

Besides being a Cr getter, the segregated SrO may react with water vapor in the cathode gas, which results in the formation of volatile Sr species. These volatile Sr species diffuse in the porous cathode material and become a possible source for $SrZrO_3$ formation at the cathode/electrolyte interface. A hint volatile Sr species comes from the post analysis results of two commercial SOFC samples. One was a reference sample after manufacturing. The other was from a stack operated at 850 °C for 2000 h. The cross sections of these two samples were investigated by scanning electron microscopy (SEM) and energy dispersive spectroscopy (EDS). The constitution of the cathode side from top to bottom was: a $(La,Sr)(Co,Mn)O_{3-\delta}$ cathode contact layer, a $(La,Sr)(Co,Fe)O_{3-\delta}$ cathode layer, a porous GDC diffusion barrier layer and a ZrO_2-based electrolyte. The interesting result was the Sr distribution after stack operation. Fig. 4.6 shows the EDS mapping of Sr at the cathode side of the cell, both in the reference state (Fig. 4.6a) and after operation at 850 °C for 2000 h (Fig. 4.6b). After operation Sr enrichment was detected in the bulk LSCF cathode, indicating SrO precipitation within the LSCF cathode. A potential reason may be the quality of the commercial LSCF powder used for the cathode manufacturing. Zooming into the porous GDC layer (Fig. 4.7), Sr was enriched at the GDC/electrolyte interface in both the reference cell (Fig. 4.7a) and the cell after 2000 hours of operation (Fig. 4.7b). This indicated that Sr started to diffuse to the electrolyte during the cathode sintering process. During operation SrO deposited in the pores of the GDC layer (Fig. 4.7b), which gave evidence for the presence of gaseous Sr species.

In this stack, during the cathode sintering process, the Sr diffusion occurred mainly through the grain boundaries of the GDC layer, while during the operation the Sr diffusion took place by gas phase transport (e.g. $Sr(OH)_2(g)$). During the cathode sintering process the higher temperature kinetically facilitated Sr diffusion through the GDC grain boundaries. In addition, there was no Sr segregation in the cathode material. Therefore, the SrO activity was less than unity, so that the influence from gaseous Sr species could be neglected. However, during operation, Sr segregation in the bulk

cathode (in form of SrO) increased the SrO activity up to aSrO = 1. As a result, a pronounced amount of gaseous Sr species was produced in humid air compared to the cathode sintering process. The evaporated gaseous Sr species diffused through the pores of the GDC layer and subsequently deposited there. In addition, the gaseous Sr species could also react with the ZrO_2-based electrolyte during long-time stack operation. To further shed light on this issue, the volatile Sr species are studied by both thermodynamic calculations using FactSage [73] and experimental investigations.

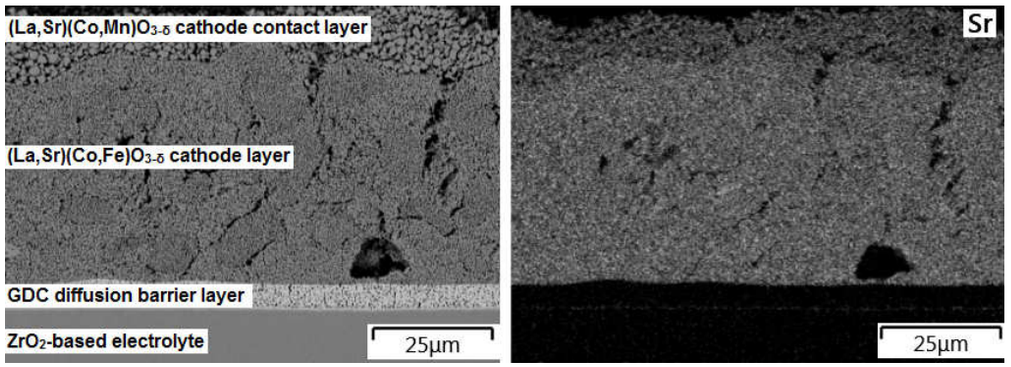

(a) The reference cell

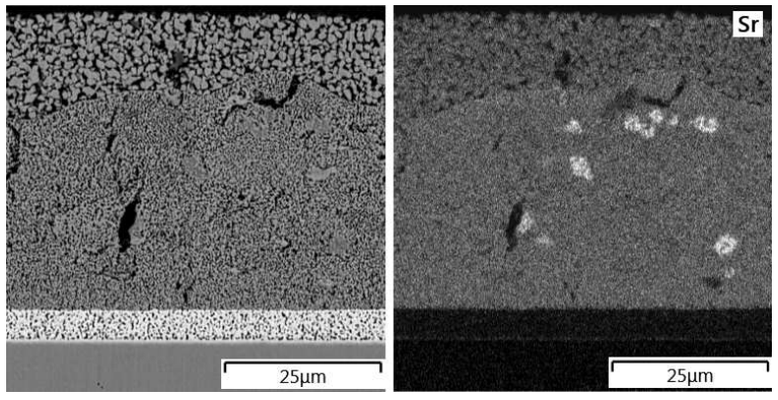

(b) The cell after operation at 850°C for 2000h

Figure 4.6: EDS maping of Sr at the cathode side.

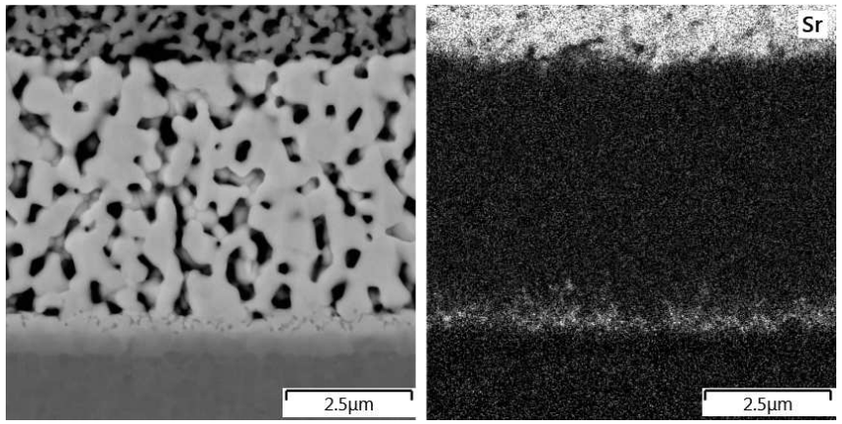

(a) The reference cell

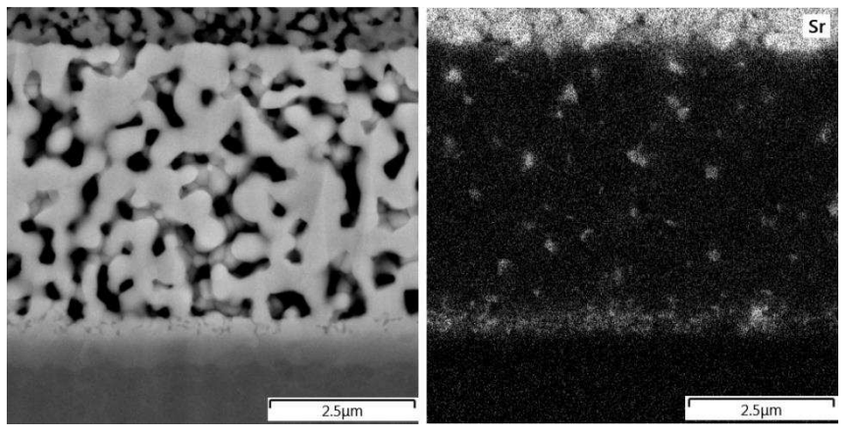

(b) The cell after operation at 850°C for 2000h

Figure 4.7: EDS mapping of Sr in the porous GDC layer.

4.2.1 Thermodynamic calculation on Sr species evaporation

4.2.1.1 Calculation parameters

Based on the SGPS database, the equilibrium partial pressures of possible gaseous Sr species over pure SrO (aSrO=1) at pH_2O=0.03 bar are calculated and compared in the temperature range from 600 °C to 1000 °C. Since the partial pressures of SrOH additionally depends on pO_2, two different pO_2 are considered, normal air condition (pO_2=0.21 bar) and oxygen deficiency condition (pO_2=10^{-5} bar). The corresponding chemical reactions are as follows:

$$SrO(s) + H_2O(g) \leftrightharpoons Sr(OH)_2(g) \tag{4.8}$$

$$SrO(s) + \frac{1}{2}H_2O(g) \leftrightharpoons SrOH(g) + \frac{1}{4}O_2(g) \tag{4.9}$$

$$SrO(s) \leftrightharpoons SrO(g) \tag{4.10}$$

4.2.1.2 Results and discussion

The equilibrium partial pressures of possible gaseous Sr species over pure SrO are compared in Fig. 4.8. In humid air, $Sr(OH)_2$ is the dominant gaseous Sr species. $pSr(OH)_2$ depends on temperature, pH_2O and aSrO. Fig. 4.9 shows a comparison of the equilibrium partial pressure of $Sr(OH)_2$ over pure SrO and the equilibrium partial pressures of $CrO_2(OH)_2$ and CrO_3 over pure Cr_2O_3. pH_2O and pO_2 is considered as 0.03 bar and 0.21 bar, respectively. Apparently, $pSr(OH)_2$ shows a stronger temperature dependence than $pCrO_2(OH)_2$. In SOFC stacks, the Cr_2O_3 containing scale formed on the interconnect surface is not pure Cr_2O_3 (e.g. Cr-Mn spinel) [8, 9], resulting in lower $CrO_2(OH)_2$ evaporation. Meanwhile, the applications of interconnect protective coatings [11-13] and cathode contact layers [8] prevent additional $CrO_2(OH)_2$ evaporation. Therefore, during stack operation $pCrO_2(OH)_2$ should be lower than the calculated equilibrium value. Moreover, SrO segregation from the LSCF cathode [48-52] contributes to the volatile $Sr(OH)_2$ formation. Hence, it is reasonable to consider that during the operation of SOFC stacks $pSr(OH)_2$ is comparable with $pCrO_2(OH)_2$.

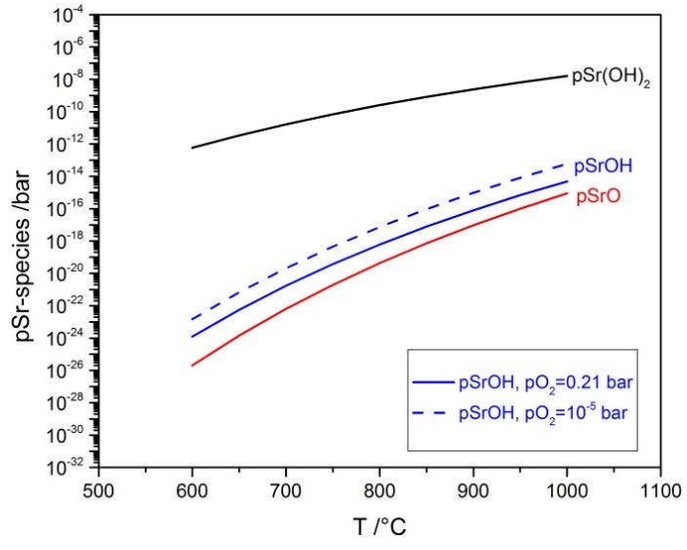

Figure 4.8: Comparison of equilibrium partial pressures of possible gaseous Sr species over pure SrO (aSrO=1) when pH_2O=0.03 bar.

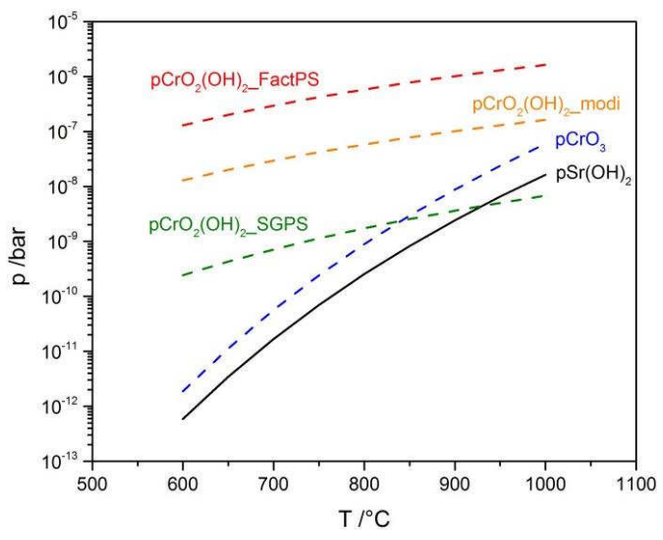

Figure 4.9 Comparison of equilibrium partial pressure of $Sr(OH)_2$ over pure SrO with equilibrium partial pressures of $CrO_2(OH)_2$ and CrO_3 over pure Cr_2O_3. pH_2O=0.03 bar and pO_2=0.21 bar.

4.2.2 Experiments on Sr species evaporation

4.2.2.1 Experimental setup

To further substantiate the above thermodynamic predictions and to apply them to SOFC systems, a set of dedicated transpiration experiments were performed. The purpose of them is two-fold: First, to get further insights into the Sr species evaporation from LSCF, and, second, to understand the influence of segregated SrO on the Sr species evaporation and the subsequent reaction with the ZrO_2-based electrolyte. In detail, the reaction between gaseous Sr species (mainly $Sr(OH)_2(g)$) and 8mol-%Y_2O_3-ZrO_2 (8YSZ) was studied. A sketch of the experimental setup is shown in Fig. 4.10. An Al_2O_3 boat (the basal area is about 3.1 cm^2) is used as a container for SrO or LSCF powder. A certain amount SrO or LSCF powder is loaded such that the basal area of the Al_2O_3 boat is covered by SrO powder or LSCF powder both before and after the heat treatment. It is notable that powders have a higher specific surface area than bulk materials used in SOFC stacks. However, powders do not affect the thermodynamics but can accelerate the kinetics in the experiments. The 8YSZ sheet (2 cm × 2 cm, produced by Kerafol) is put on the top of the Al_2O_3 boat as a Sr getter. There is no direct contact between the SrO or the LSCF powder and the 8YSZ sheet. The setup ensures easy diffusion of evaporated Sr species to the 8YSZ sheet. SrO powder (produced by Alfa Aesar) and LSCF powder (composition: $La_{0.58}Sr_{0.4}Co_{0.2}Fe_{0.8}O_{3-\delta,}$ in-house produced by IEK-1, Forschungszentrum Jülich GmbH, after calcination and ready for cathode printing processes) was used, respectively, as a source to supply gaseous Sr species. The experiments were carried out in stagnant air at 800 °C and 1000 °C, respectively. This temperature range is comparable to the operating conditions of IT-SOFC and higher temperatures can accelerate the kinetics. During the heat treatments, two different holding time, 200 h and 400 h, were chosen. A summary of experimental conditions is shown in Table 4.3. After the experiments, the surface of each 8YSZ sheet facing the Sr source was investigated by SEM and EDS.

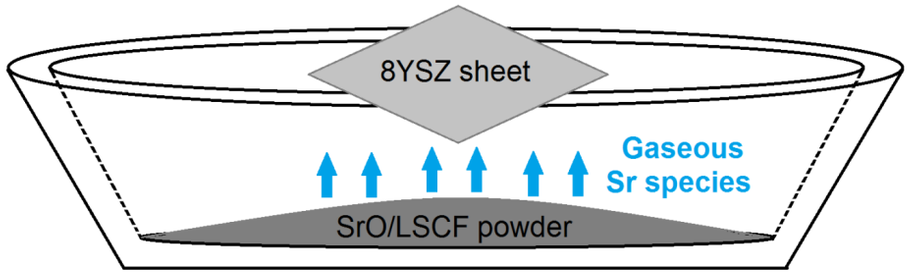

Figure 4.10: Experimental setup for the reaction between gaseous Sr species and the 8YSZ electrolyte.

Table 4.3: Summary of the heat treatment conditions for five 8YSZ sheet samples.

Temperature /°C (in stagnant air)	The source to supply gaseous Sr species	
	SrO powder	LSCF powder
800 (200 h)	**sample 1**	**sample 2**
1000 (200 h)	**sample 3**	**sample 4**
800 (400 h)	**sample 5**	

4.2.2.2 Results and discussion

Fig. 4.11a is the SEM micrograph of the surface of the as-received 8YSZ sheet. Fig. 4.11b-f are the SEM micrographs of the surfaces of sample 1, sample 2, sample 3 and sample 4, respectively. For sample 3, which was heated at 1000°C for 200h with SrO powder being a source to supply gaseous Sr species, uniformly distributed small particles were detected on its surface (Fig. 4.11d). EDS spectra of three representative points of sample 3 are shown in Fig. 4.12. Point 1 and point 2 are on the 8YSZ grain with different brightness. Point 3 is on the deposited particle. As results, Sr is detected at all the three points. In contrast, the surfaces of sample 1 (Fig. 4.11b), sample 2 (Fig. 4.11c) and sample 4 (Fig. 4.11d) are clean and as smooth as the as-received one (Fig. 4.11a), which indicates that there is no Sr deposition.

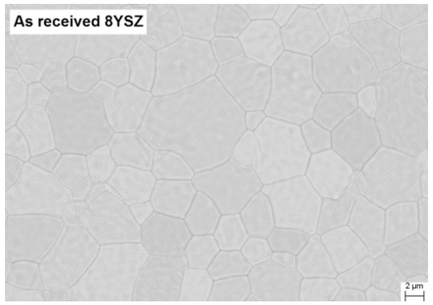

(a)

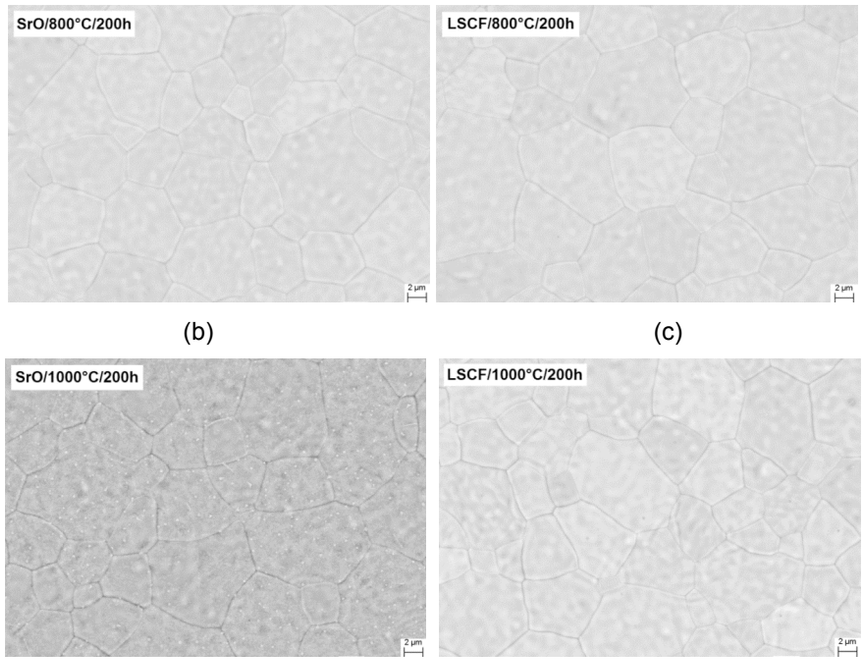

(b) (c)

(d) (e)

Figure 4.11: SEM micrographs of the surface of a) as-received 8YSZ disc; b) Sample 1: after heat treatment at 800 °C for 200 h with SrO powder as Sr source, no Sr-deposition; c) Sample 2: after heat treatment at 800 °C for 200 h with LSCF powder as Sr source, no Sr-deposition; d) Sample 3: after heat treatment at 1000 °C for 200 h with SrO powder as Sr source, Sr was detected; e) Sample 4: after heat treatment at 1000 °C for 200 h with LSCF powder as Sr source, no Sr-deposition.

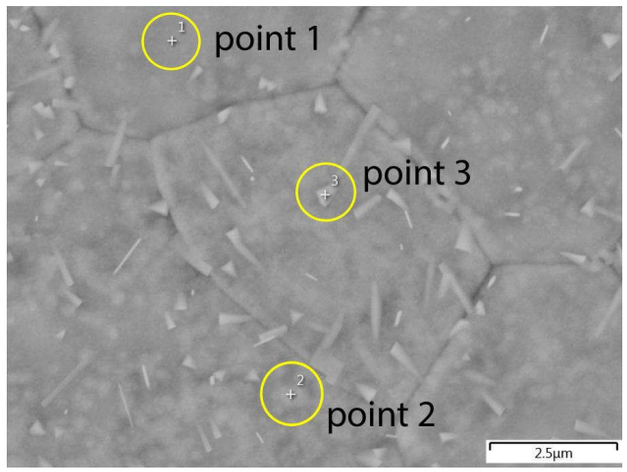

(a)

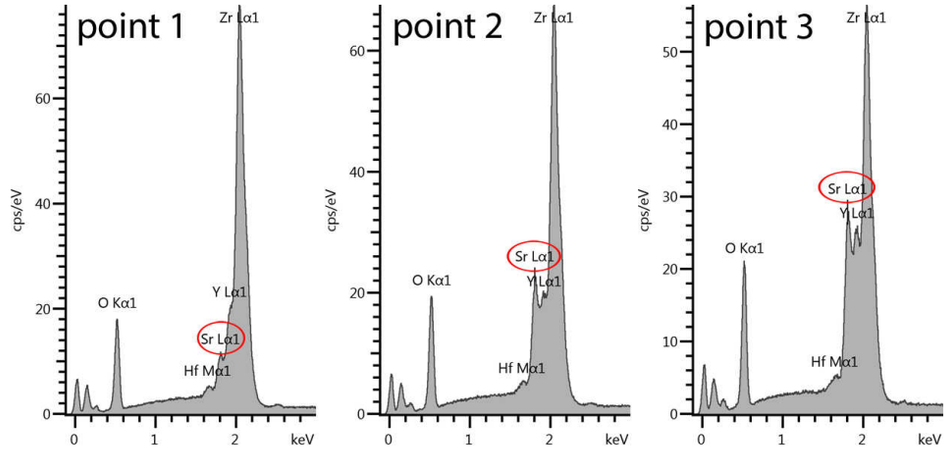

(b)

Figure 4.12: EDS spectra of three representative points on sample 3 after heat treatment at 1000 °C for 200 h with SrO powder being as Sr source.

According to the thermodynamic calculations, in the presence of humidity the dominant gaseous Sr species is $Sr(OH)_2$. $pSr(OH)_2$ depends strongly on temperature and SrO activity. If the temperature increases from 800 °C to 1000 °C, $pSr(OH)_2$ increases by two orders of magnitude. Regarding the Sr source, the SrO activity is about 10^{-4} for LSCF powder at 1000 °C [92], while for pure SrO powder the SrO activity is 1. As a result, $pSr(OH)_2$ over pure SrO powder is significantly higher than it is over LSCF powder. Additionally, high temperatures kinetically facilitate the reaction between $Sr(OH)_2(g)$ and the 8YSZ sheet. Therefore, experimentally, after 200 h heat treatment Sr deposition was only detected on the 8YSZ sheet which was heated at 1000 °C with SrO being the source to supply gaseous Sr species (sample 3). Fig. 4.13 is an EDS mappings of Zr, Y and Sr of the surface of sample 3. For some 8YSZ grains, Sr deposits along the grain boundaries only, whereas for some 8YSZ grains, Sr deposits directly on top of them. It looks like that Sr deposition depends on the orientation of the 8YSZ grains.

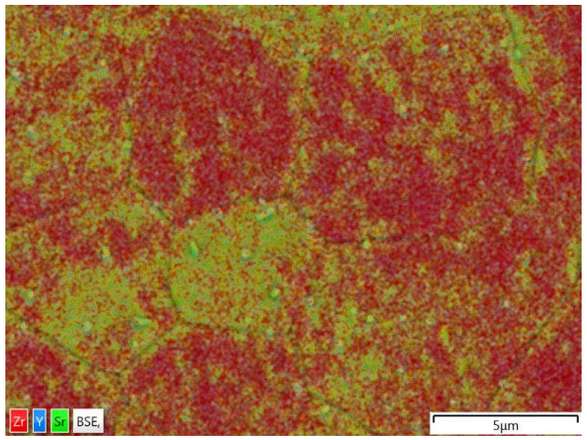

(a)

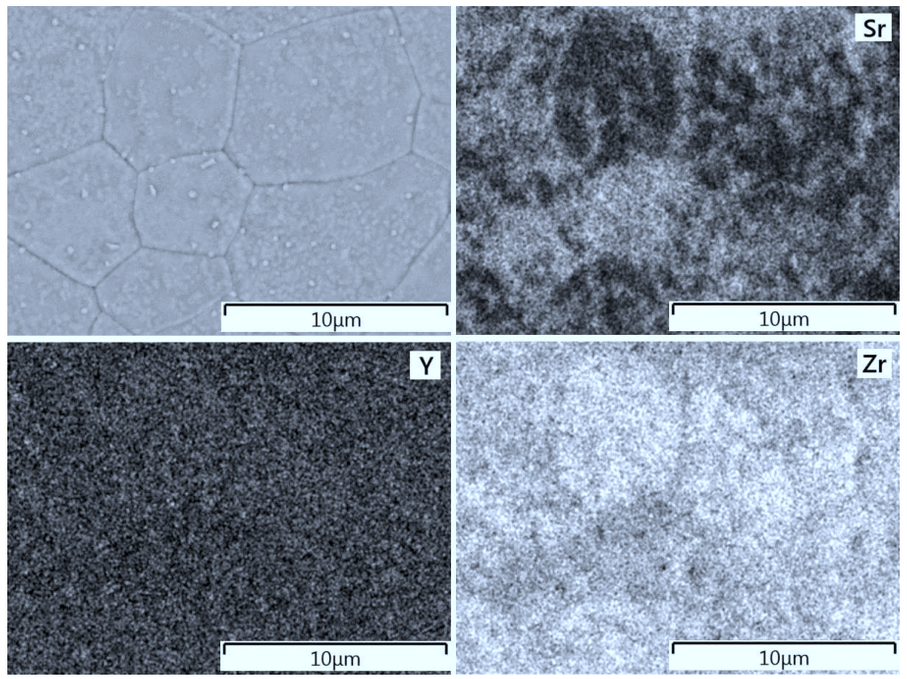

(b)

Figure 4.13: EDS mappings of Zr, Y and Sr of sample 3.

Compared to Sample 1 (SrO/800 °C/200 h), by increasing the holding time to 400 h, as shown in Fig. 4.14, some particles were detected on sample 5, which was heated at 800 °C with SrO being the source to supply gaseous Sr species. EDS spectra of five representative points of sample 5 are shown in Fig. 4.15. Sr is found at point 3 and point 5. However, at point 3 Mg and Si are detected together. Mg and Si may come from the refractory linings of the furnace. Point 5 is on a big isolated particle, where besides Sr, Mo and Ba are detected. The Mo and Ba are expected from the heating elements of the furnace. Fig. 4.16 is the EDS mappings of Sr, Mo, Mg, Si, Y, Zr and O for a selected area on the sample 5. The big isolated particles (~1 μm) could be the Sr-Mo-O compond. Besides these big isolated particles, there are several submicron particles (as examples, marked by yellow circle) which are Sr-rich. By increasing the holding time from 200 h to 400 h, Sr deposition was detected on the 8YSZ sheet which was heated at 800 °C with SrO being the source to supply gaseous Sr species. Compared to sample 3, due to the lower exposure temperature, the Sr depositions on sample 5 were sporadic. It is reasonable to believe that after sufficiently long exposure, Sr deposition should also be found on sample 2 and sample 4, for which LSCF powder was the Sr source.

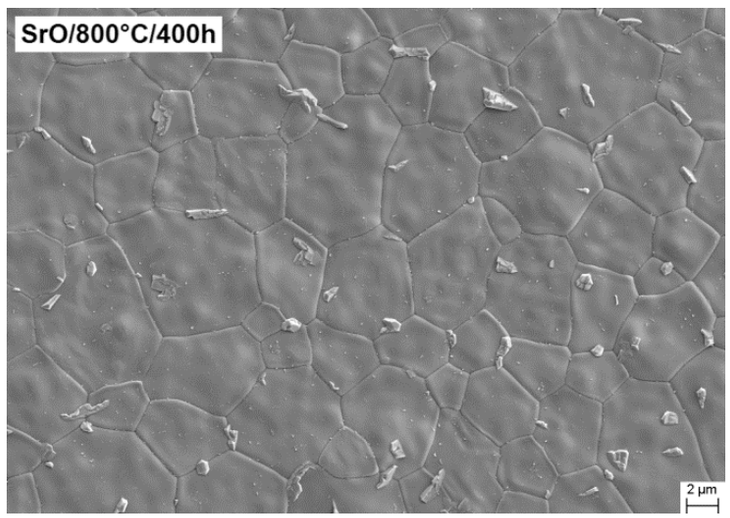

Figure 4.14: Surface of sample 5 (after heat treatment at 800 °C for 400 h with SrO powder as Sr source).

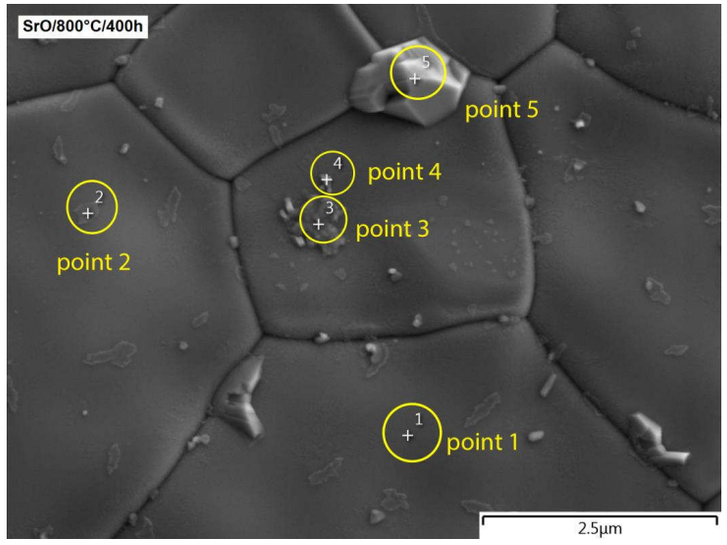

(a)

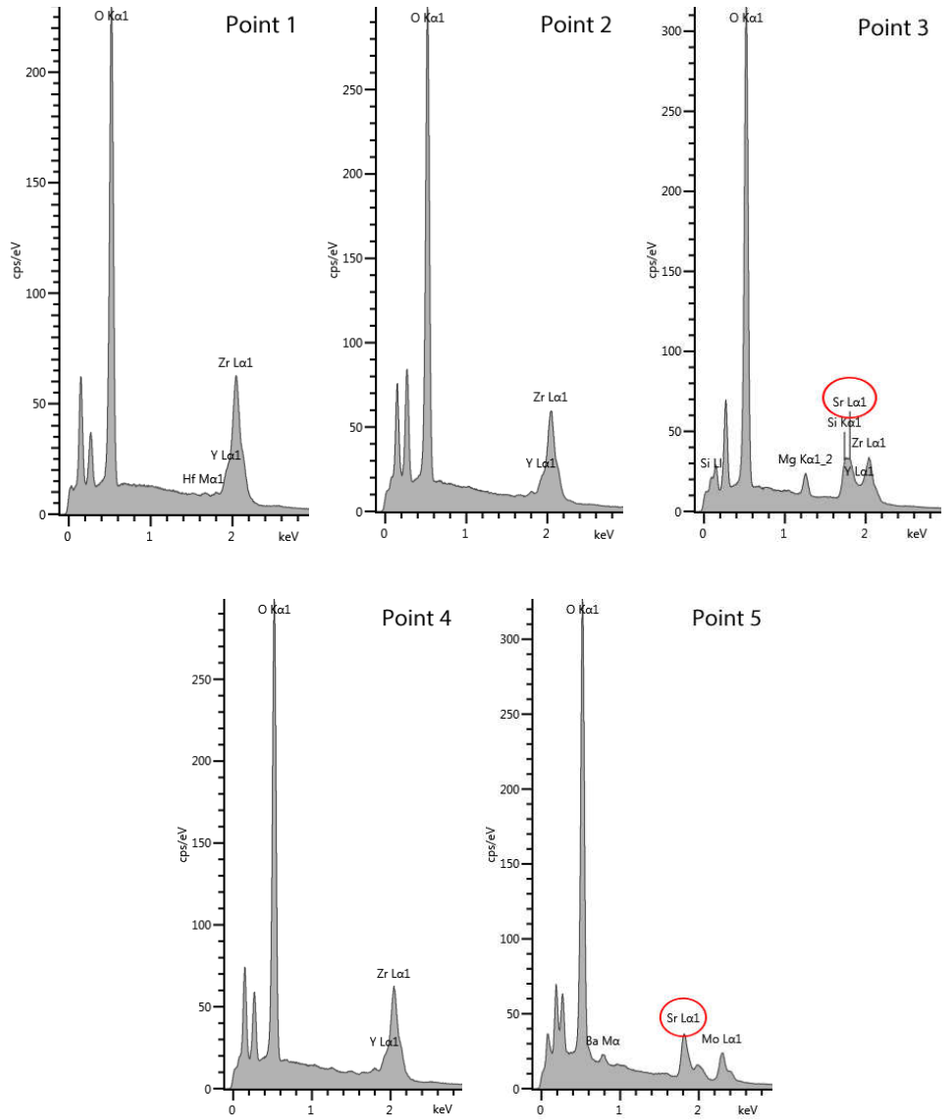

(b)

Figure 4.15: EDS spectra of five representative points of sample 5.

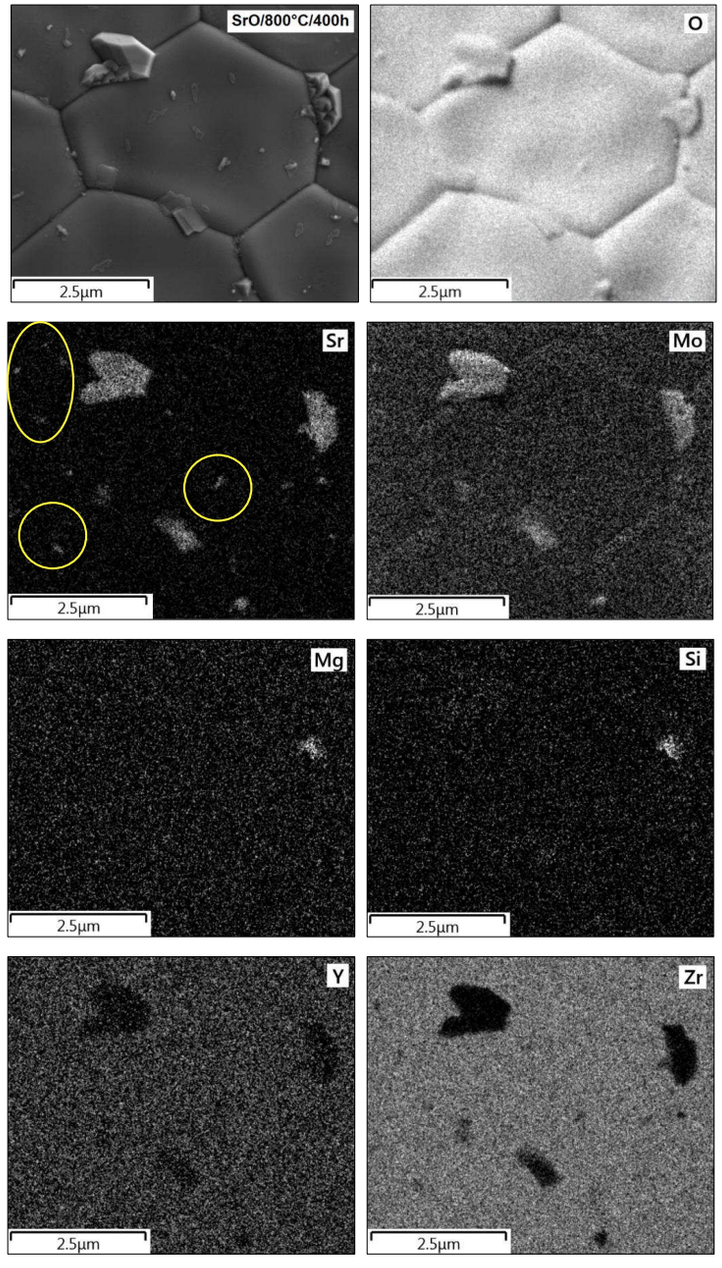

Figure 4.16: EDS mappings of O, Sr, Mo, Mg, Si, Y and Zr of sample 5.

In addition, some experiments were carried out by using Al-doped YSZ sheet as the Sr-getter. The same experiment set up was used (Fig. 4.10). In these groups of experiments, Sr deposition was detected on the surface of Al-doped YSZ sheet that after heat treatment at 800 °C for 200h when SrO powder was the Sr source. As shown in Fig. 4.17, expecially for the Al-free area (area 3). Compared to sample 1 (Fig. 4.11b, 8YSZ sheet), which had the same heat treatment condition but no Sr depositon was found, the Sr depositon on Al-doped YSZ sheet might due to the much smaller grain size. The smaller YSZ grain size facilitates the reaction between the gaseous Sr species and YSZ grains.

SrO segregation from LSCF cathode facilitates pronounced evaporation of volatile Sr species, which is a reaction partner for ZrO_2-based electrolytes and resulting in subsequent formation of the ionic insulating $SrZrO_3$ precipitates at the GDC/ZrO_2-based electrolyte interface. The reaction between the volatile Sr species and ZrO_2-based electrolyte depends on temperature, the Sr source, exposure time and the grain size of ZrO_2. To minimize the influence of volatile Sr species on the performance of SOFC stacks, dry air is optimal as cathode gas. A dense GDC diffusion barrier layer is preferred, as it can block volatile Sr species diffusion. However, the formation of pores or cracks in dense GDC layers [55, 59] during operation may provide paths for volatile Sr species diffusion. Additionally, an appropriate grain size of ZrO_2-based electrolyte could also contribute to hindering the reaction with gaseous Sr species.

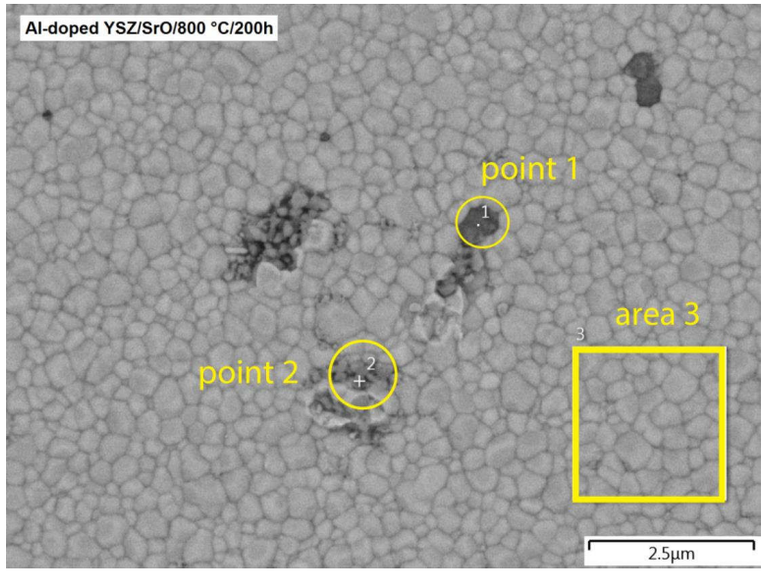

(a)

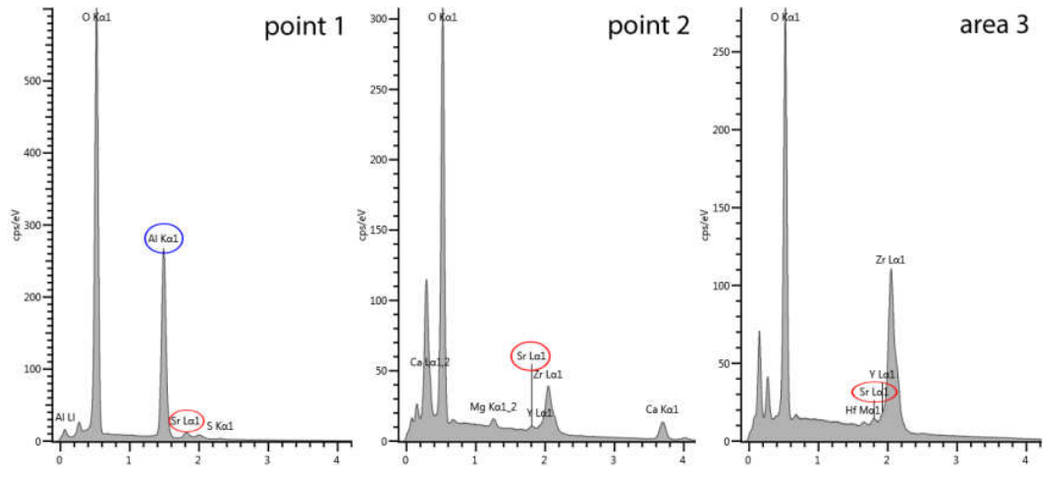

(b)

Figure 4.17: EDS spectra of Al-doped YSZ sheet after heat treatment at 800 °C for 200h when SrO powder was the Sr source.

4.3 Measuring ZrO_2 activity in 8YSZ

From a thermodynamic point of view, the reaction between Sr species and 8mol-%Y_2O_3-ZrO_2 (8YSZ) electrolyte depends on the ZrO_2 activity in 8YSZ. The ZrO_2 activity in 8YSZ is measured by Knudsen Effusion Mass Spectrometry (KEMS).

4.3.1 Experiment set up

KEMS experiments to determine the ZrO_2 activity in 8YSZ were carried out in a single-focusing magnetic mass spectrometer CH5 (Varian MAT, Bremen). The general procedures were: 1) pyrometer calibration; 2) measuring the temperature dependence of the ion current intensity of ZrO_2^+ ($I_{ZrO_2^+}(T)$) from 8YSZ powder and the ion current intensity of ZrO_2^+ ($I^\circ_{ZrO_2^+}(T)$) from pure ZrO_2 powder, respectively; and 3) Calculating the thermodynamic activity according to Eq. 3.27.

The optical pyrometer (Dr. Georg Maurer GmbH, Kohlberg, Germany) was firstly calibrated by measuring the melting points of pure metals such as Ag, Cu, Ni, Pt, and Rh to get the linear relationship between the pyrometer readings and the true melting temperatures in a very large temperature range. Second, to get the systematical periodical deviation from linearity on a short temperature range scale, the pyrometer was calibrate by comparing experimental data 'ln(IT) vs. 1/T' for pure substances (Pt, Rh, Ir and ZrO_2) with a corresponding model function. The model function can be constructed by using the ion current intensity measured at the melting point of the substance and its reference slope found from the IVTANTHERMO database [98] for the mean temperature of the measurement range. A temperature correction was obtained by a numerical procedure and was applied to recalculate the pyrometer readings into true temperatures. 8YSZ powder (from Tosch) and pure ZrO_2 powder (from Sigma Aldrich) were sublimed in the temperature range from 1900 °C to 2200 °C. The sample (8YSZ powder or pure ZrO_2 powder) was loaded in a tungsten liner (inner cell) with the inner dimensions of 7~8 mm and then was placed inside a massive tungsten Knudsen cell which had an orifice with a diameter of 0.8 mm. 3 different runs were performed for

8YSZ powder and pure ZrO_2 powder, respectively. The ion currents of ZrO_2^+ were measured in cooling and heating cycles. The cell was baked after each experiment with ZrO_2 followed by one with 8YSZ to avoid a memory effect. The temperature of the cell was monitored in a black body hole at the bottom of the Knudsen cell using the automatic optical pyrometer. The gaseous species effusing from the cell were ionized by the electrons with energy of 70 eV and an emission current of 0.1 mA. The ions formed in the ionization chamber were focused by an ion-optical system and accelerated with a negative potential of 8000 V to a 90º magnetic sector field, where they were separated according to their mass-to-charge ratio. The ion current intensity of ZrO_2^+ from respective 8YSZ ($I_{ZrO_2^+}(T)$) and pure ZrO_2 ($I^\circ_{ZrO_2^+}(T)$) was recorded by a universal frequency counter TF830 1.3 GHz (TTi) or by a secondary electron multiplier MC12/17 (MasCom). Then the ZrO_2 activity in 8YSZ was calculated according to Eq. 3.27.

4.3.2 Results and discussion

After the experiments, the residuls of the samples in the Knudsen cells were examined by XRD-analysis. The samples were stable under the experimental conditions and there was no reaction with the cell material. The temperature dependence of the ZrO_2 activity in 8YSZ is shown in Fig. 4.18. The data obtained from these 3 runs are consistent with each other. Within the limits of errors, the data demonstrates nearly no temperature dependence of the ZrO_2 activity in 8YSZ. The average value is around 0.85. Therefore, it is reasonable to estimate the same ZrO_2 activity in 8YSZ under SOCF operation conditions (700 °C to 900 °C). A high ZrO_2 activity in 8YSZ facilitates the reaction between Sr species and 8YSZ from the thermodynamic point of view.

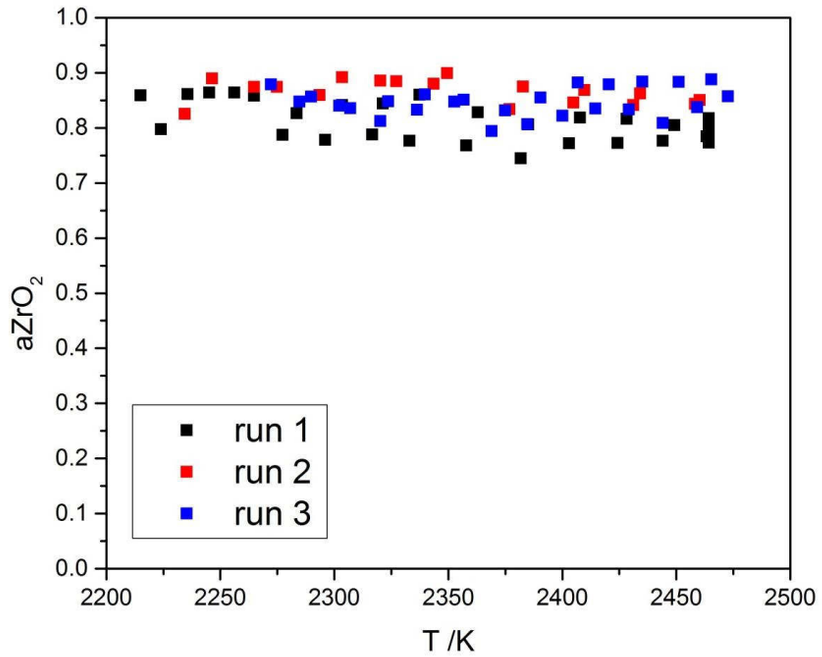

Figure 4.18: Temperature dependence of the ZrO_2 activity ($aZrO_2$) in 8YSZ.

4.4 Conclusion

In chapter 4, Sr related degradation issues, Cr poisoning and formation of volatile Sr species have been studied. Cr poisoning is considered as a two-step process: Cr species evaporation and Cr species deposition. CrO_3 and $CrO_2(OH)_2$ are the dominant gaseous Cr species in dry air and humid air, respectively. $pCrO_3$ has a stronger temperature dependence than $pCrO_2(OH)_2$. The thermodynamic calculations suggest that dry air is optimal as cathode gas to minimize the Cr species evaporation, together with a reduced operation temperature of the SOFC. Additionally, since the stack sealing process is carried out at high temperature, e.g. ~700 °C for glass-based sealants and ~1000 °C for air brazing technique. To prevent Cr species evaporation, dry air atmosphere is also preferred. SrO from the LSCF cathode is a reaction partner for the evaporated Cr species. Depending on different pO_2, $pCrO_3$, aSrO and temperature, the reaction products between SrO(s) and CrO_3(g) could either be $SrCrO_4$, $SrCrO_3$, $Sr_3Cr_2O_8$ or Sr_2CrO_4. The thermodynamic calculations demonstrate that the $SrCrO_4$ is the primary Cr poisoning product which is always found on the top of the cathode surface. Sometimes due to the drop of local pO_2 in the cathode, the formation of Sr-Cr-O inside the LSCF cathode can be possible, e.g. at the cathode/electrolyte interface. Both the thermodynamic calculations and experiments show, that in presence of humidity in the air, volatile Sr species (mainly $Sr(OH)_2$) can be formed, which is a reaction partner for ZrO_2-based electrolytes and results in subsequent formation of the ionic insulating $SrZrO_3$ precipitates. To minimize the influence of volatile Sr species on the performance of SOFC stacks, dry air is optimal as cathode gas. A dense GDC diffusion barrier layer is preferred between the cathode and electrolyte, as it can block volatile Sr species diffusion to the electrolyte. Additionally, an appropriate grain size of ZrO_2-based electrolyte could also contribute to hindering the reaction with gaseous Sr species. From a thermodynamic point of view, the reaction between volatile Sr species and the ZrO_2-based electrolyte depends on the ZrO_2 activity in the ZrO_2-based electrolyte. As an example, the ZrO_2 activity in 8mol-%Y_2O_3-ZrO_2 (8YSZ) has been measured as around 0.85. A high ZrO_2 activity facilitates the reaction between volatile Sr species and 8YSZ.

5. First principles based determination of the thermal expansion of $La_{0.5}Sr_{0.5}Co_{0.25}Fe_{0.75}O_3$[2]

In this chapter, first principles phonon calculations combined with the quasi-harmonic approximation (QHA) are demonstrated to predict thermal expansion coefficient of the LSCF cathode, and then the prediction is compared to the results from experimental investigations. The composition $La_{0.6}Sr_{0.4}Co_{0.2}Fe_{0.8}O_{3-\delta}$ is preferentially used as cathode materials in SOFCs. However, the structure size of $La_{0.6}Sr_{0.4}Co_{0.2}Fe_{0.8}O_{3-\delta}$ is so large that the computation would be much more expensive. Therefore, to reduce the structure size and simplify the calculation, a similar composition $La_{0.5}Sr_{0.5}Co_{0.25}Fe_{0.75}O_3$ (LSCF55) is studied.

5.1 Computational approach

5.1.1 Structure

$La_{1-x}Sr_xCo_{1-y}Fe_yO_{3-\delta}$ perovskites have a rhombohedral symmetry at low temperature, and transform at higher temperature to a cubic symmetry by a second order phase transition [26, 27]. Here, $La_{0.5}Sr_{0.5}Co_{0.25}Fe_{0.75}O_3$ (LSCF55) with the rhombohedral structure is studied. Starting from the rhombohedral structure of $LaCoO_3$ (Fig. 5.1), space group R-3cr, Sr and Fe substitute La and Co, respectively. In order to reach the composition of $La_{0.5}Sr_{0.5}Co_{0.25}Fe_{0.75}O_3$ (LSCF55), i.e. the atom ratios of La to Sr being 1:1 and Co to Fe being 1:3, a 2×1×1 extension of the primitive cell (Fig. 5.1) is required. Four potential structures of LSCF55 are shown in Fig. 5.2.

[2] Section content published. X. Yin et al., J. Am. Ceram. Soc., 2018; 1-8. https://doi.org/10.1111/jace.15430

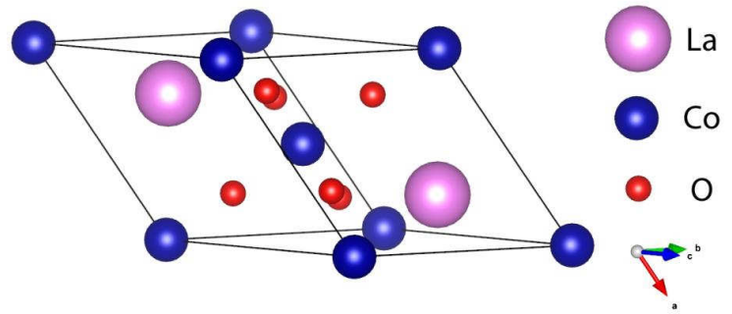

Figure 5.1: $LaCoO_3$ (space group R-3cr) with rhombohedral structure.

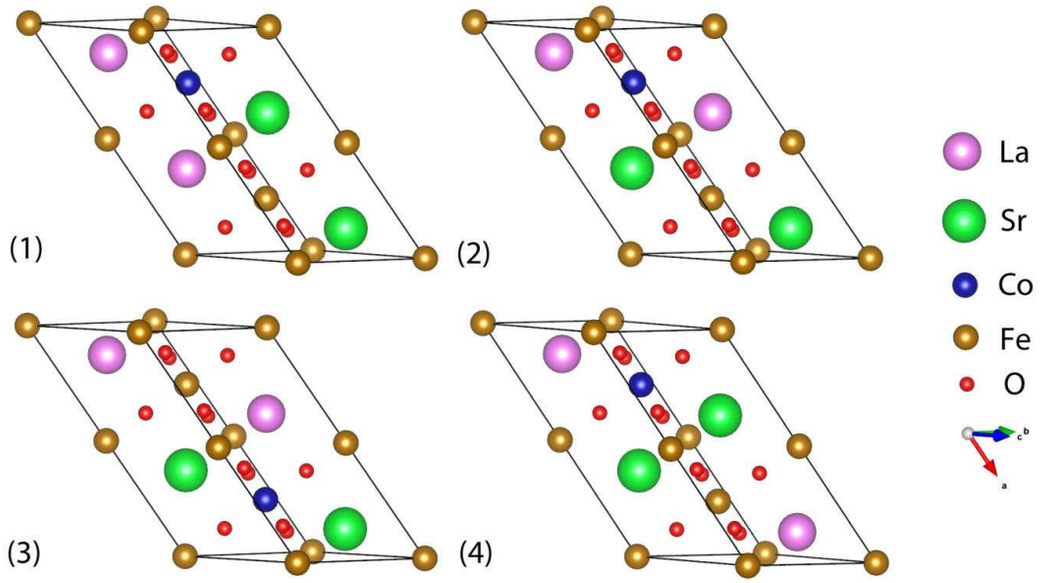

Figure 5.2: Four potential structures of LSCF55.

5.1.2 Computational details

Structure relaxations of these four different LSCF55 were carried out in the Vienna Ab Initio Simulation Package (VASP) [76]. The generalized gradient approximation (GGA) exchange-correlation (XC) functional of Perdew, Burke and Ernzerhof (PBE) [83] was employed. The interaction between the valence electrons and nuclei plus frozen core electrons was represented by the projector augmented-wave (PAW) method [87]. The PBE potential was employed from the VASP library [99] with labels: La (core=Kr4d), Sr_sv (4s4p5s), Co (d8s1), Fe (d7s1) and O (s2p4). The plane wave basis energy cutoff was 520 eV. The first-order Methfessel-Paxton smearing with the width of 0.1 eV was employed to perform the first Brillouin zone integration. A 4×4×4 Γ-point-centered k-points mesh was used. All calculations were spin polarized. Ferromagnetic states were considered in this work, and the convergence with respect to the magnetic moments was checked. The electronic energy convergence was set to 10^{-9} eV. During the structure relaxation, force and stress tensor were calculated, ions, cell shape and cell volume were allowed to change. A full structure relaxation was carried out with forces converged to 10^{-5} eV $Å^{-1}$. Ground state energies of the four different fully relaxed structures were compared. The structure with the most negative energy was chosen as the energetically most favorable structure for LSCF55. Based on it different volumes were introduced by changing all lattice vectors and all atomic coordinates isotopically with factors in the range from 0.995 to 1.02. Likewise, these structures with different volumes were fully relaxed with the same criteria as the initial structure (apart from the volume relaxation).

Phonon calculations were performed on each volume by the supercell approach. 1×2×2 supercells of fully relaxed structure with symmetry-distinct displacements were generated by the PHONOPY code [79]. The generated supercells were acting as inputs for the first principle calculations in VASP to calculate the atomic forces as a response to the displacements. In these sets of force calculations, a 4×2×2 Γ-point-centered k-points mesh was used. The other parameters were the same as the structure relaxation. The Helmholtz free energy of LSCF55 was obtained as a function of volume at specified

temperatures. For each temperature, the Vinet equation-of-state (EOS) [100] was used to fit the curve of volume dependent Helmholtz free energies, from which the volumetric thermal expansion coefficient was extracted, as explained in Chap. 3.5.

Additionally, the calculations for the same potential structure with local density approximation (LDA) exchange-correlation were performed. Except the potential file, the other input files were kept the same as the calculations with the GGA exchange-correlation. The LDA potential was employed with the VASP library labels: La (core=Kr4d), Sr_sv (3s3p4s), Co (d8s1), Fe (d7s1) and O (s2p4). The calculated volumetric thermal expansion coefficients based on GGA exchange-correlation and LDA exchange-correlation were compared with experimental measurements.

5.2 Experimental approaches

LSCF55 powder was synthesized by the Pechini method [101]. The raw powder was calcined in stationary air at 973 K for 3 hours and subsequently at 1373 K for 3 hours (heating and cooling rate 2 K min^{-1}), to obtain a single perovskite phase. To confirm the phase composition, X-ray diffraction (XRD) was applied. As expected, only one perovskite phase with rhombohedral structure was found, with small amounts of secondary phases, 5 wt% (La,Sr)(Co,Fe)O_4 and 1 wt% Fe_3O_4. Two complementary methods are used to determine the thermal expansion: 1) measuring the temperature dependent lattice parameters and volume of LSCF55 grains via an in-situ high temperature X-ray diffractometer (HT-XRD), and 2) measuring the linear thermal expansion of an LSCF55 bar specimen by a thermo-mechanical analyzer.

5.2.1 In-situ high temperature X-ray diffractometer

The lattice parameters and volume of the perovskite LSCF55 grains were measured by in-situ HT-XRD (PANalytical EMPYREAN) from 298 K up to 973 K in air with a heating and cooling rate of 2 K min^{-1}. Hexagonal lattice parameters a_{hex} and c_{hex} were used to

illustrate the rhombohedral structure. When $a_{hex}/\sqrt{2} = c_{hex}/2\sqrt{3}$ is reached, the LSCF55 transforms from the rhombohedral structure to the cubic structure.

5.2.2 Thermo-mechanical analyzer

Complementary, the linear thermal expansion of an LSCF55 bar specimen was measured by a vertical high-performance thermo-mechanical analyzer (Setsys Evolution, Setaram, France). First, the LSCF55 powder was first put into a cuboid mold with underside area of 5×10 mm^2 and pressed under a uniaxial pressure of 100 MPa at room temperature. The bar specimen was then sintered at 1523 K for 5 hours with heating and cooling rate 2 K min^{-1}. Then, the linear thermal expansion was measured in the shorter direction of the porous bar specimen in a temperature range from room temperature up to 673 K in air (heating rate: 2 K min^{-1}). Before measurement the initial length of the bar sample was measured by the equipment, which was l_0 = 2219.21 µm and a 5 N pre-load was applied.

5.3 Results and discussion

5.3.1 Structure of LSCF55

The temperature dependence of $a_{hex}/\sqrt{2}$ and $c_{hex}/2\sqrt{3}$ that obtained from HT-XRD is shown in Fig. 5.3. Above 723 K, the difference between $a_{hex}/\sqrt{2}$ and $c_{hex}/2\sqrt{3}$ is less than 0.0002 Å, hence LSCF55 transforms to the cubic structure around this temperature.

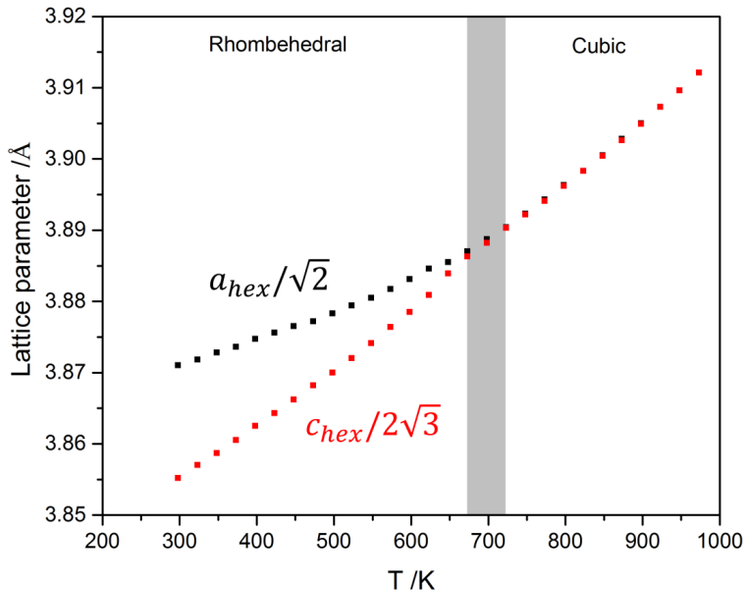

Figure 5.3: Temperature dependence of the lattice parameters of LSCF55 (in hexagonal setting).

Table 5.1: Structure information for the four fully relaxed structures of LSCF55.

structure	a /Å	b /Å	c /Å	α /°	β /°	γ /°	V /Å^3	E_0 /eV
1	10.87983	5.47205	5.47205	60.0004	59.8042	59.8042	229.677	-148.0169
2	10.88345	5.47741	5.47741	60.0001	59.7828	59.7828	230.128	-148.1829
3	10.90092	5.47368	5.47350	60.0035	59.8599	59.8577	230.449	-148.0921
4	10.89050	5.47494	5.47496	60.0003	59.8192	59.8195	230.199	-148.1147

Within the framework of GGA exchange–correlation, the lattice parameters, volume and ground state energies (E_0) of the four fully relaxed rhombohedral LSCF55 structures are obtained and compared in Table 5.1. The lattice parameters of these four fully relaxed structures are comparable. Structure 2 (Fig. 5.2-(2)) has the most negative ground state energy and is considered as the energetically most favorable structure for LSCF55. At finite temperature, all these four configurations may appear. The probability to find each structure can be estimated as:

$$P(E) = \frac{1}{Z} exp\left(-\frac{E_n}{k_B T}\right), \quad n = 1, 2, 3, 4 \tag{5.1}$$

Where, $Z = \sum_{n=1}^{4} exp\left(-\frac{E_n}{k_B T}\right)$ and k_B is the Boltzmann constant. $P(E)$ is the probability in a system to find a state at temperature T with energy E. Then the ratio of the probability to find structure 2 to the probability to find the other three structures can be calculated according to Eq. 5.2, respectively:

$$\frac{P(E_2)}{P(E_n)} = \frac{exp\left(-\frac{E_2}{k_B T}\right)}{exp\left(-\frac{E_n}{k_B T}\right)} = exp\left(\frac{E_n - E_2}{k_B T}\right), \quad n = 1, 3, 4 \tag{5.2}$$

Based on Eq. 5.2, at 0 K, the probability to find structure 2 is significantly higher than structure 1, 3, and 4. With increasing temperature, $P(E_2)/P(E_n)$, (n=1, 3, 4) decreases. At 700 K, the probability to find structure 2 is still respectively 15 times, 4.5 times and 3 times as the probability to find structure 1, structure 3 and structure 4. Therefore, structure 2 was taken as the energetically most favorable structure of LSCF55 for the

further phonon calculations required to predict the thermal expansion. Subsequently, the volumetric thermal expansion coefficient of structure 2 was calculated. In structure relaxation of structure 2, the total magnetic moment of 11.8228 μ_B was obtained and mainly distributed between Co (intermediate spin, 1.1 μ_B) and Fe (high spin, 2.8-3.1 μ_B). Additionally, structure 2 was studied with LDA exchange-correlation, i.e. relaxation, phonon calculations and subsequently calculating the volumetric thermal expansion.

5.3.2 Comparison between GGA and LDA exchange-correlations

After full relaxation with GGA and LDA exchange-correlations, respectively, the lattice parameters of structure 2 are compared in Table 5.2. As expected the calculated lattice constants (a, b and c) using GGA are larger than those calculated by LDA. The same comparison was done for $LaCoO_3$ by X. Wang et al. [102]. They compared the lattice constants of relaxed $LaCoO_3$ with respective LDA and GGA with the experiment values. The calculated lattice constants using GGA were larger than those using LDA. Additionally, the lattice constants calculated by GGA were closer to the experimental values. They concluded that the gradient enhancement factor of GGA was more suitable to deal with the heterogeneity of the density of the system with transition metals (e.g. Co). Therefore, for the similar system LSCF55, which contains transition metals Co and Fe, it is reasonable to believe that GGA should provide a better structure prediction than LDA. This is supported by comparison to the XRD data extrapolated to 0 K, which gives b=c=5.43 Å.

Table 5.2: Structure information of structure 2 with respective GGA and LDA.

	a /Å	a/2 / Å	b /Å	c /Å	α /°	β /°	γ /°
GGA	10.88345	5.44172	5.47741	5.47741	60.0001	59.7828	59.7828
LDA	10.59854	5.29927	5.31063	5.31063	59.9992	59.9289	59.9291

5.3.3 Thermal expansion of LSCF55

5.3.3.1 Linear thermal expansion

According to the HT-XRD, the temperature dependences of the lattice expansions are shown in Fig. 5.4. Red squares are for the c-direction of the hexagonal cell and black squares are for the a-direction of the hexagonal cell. The lattice thermal expansion coefficients of the rhombohedral LSCF55 are obtained from the slope of the linear fits, which yield $\alpha_{a,hex} = 10.89 * 10^{-6}\ K^{-1}$ and $\alpha_{c,hex} = 21.18 * 10^{-6}\ K^{-1}$. Significant anisotropic of the rhombohedral LSCF55 is observed.

For the bar specimen, after sintering the density of LSCF55 bar was measured to be about 5.08 g cm^{-3}. For comparison, the theoretical density was calculated from first principles calculation which was about 6.30 g cm^{-3} at T=0 K. The porosity of the bar specimen can be estimated as:

$$P = \frac{\rho_t - \rho_m}{\rho_t} \tag{5.3}$$

where, *P* is the porosity, ρ_t is the theoretical and ρ_m is the measured mass density. This gives as estimate *P* ≈ 19%. The thermal expansion depends only on the local atomic bonding and is not affected by long-range disruption of it by pores [103]. Therefore, porosity does not influence the thermal expansion behavior. The temperature dependence of the relative length change ($\Delta l/l_0$, $\Delta l = l - l_0$) is plotted in Fig. 5.4 in green squares. A linear fit is performed, which gives a slope of $\alpha_{l,bar\ specimen} = 17.37 * 10^{-6}\ K^{-1}$. The LSCF55 bar specimen is comprised of numerous randomly distributed LSCF55 grains such that the apparent thermal expansion is effectively isotropic. Coherency constraints between adjacent grains in the polycrystalline sample effectively confine the thermal expansion to be uniform. It is noticeable that $\alpha_{l,bar\ speciemen}$ $(17.37 * 10^{-6}\ K^{-1})$ is comparable with the arithmetical average value of $\alpha_{a,hex}$ and $\alpha_{c,hex}$ $(16.04 * 10^{-6}\ K^{-1})$.

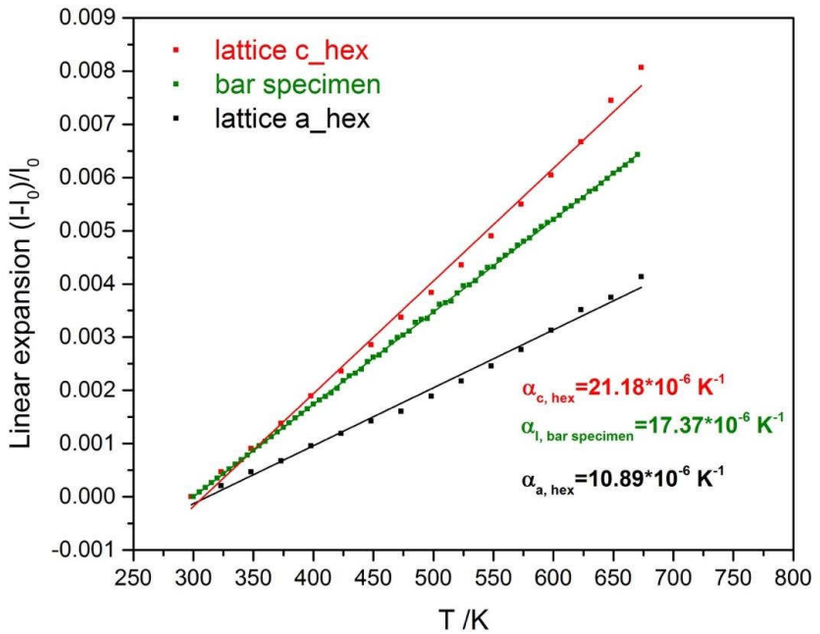

Figure 5.4: Linear expansion of rhombohedral LSCF55 with $l_0=l_{300K}$ and in the temperature range from 300 K to 670 K.

The linear expansion coefficient (α_l) of (La,Sr)(Co,Fe)$O_{3-\delta}$ bar specimens with different compositions has been widely investigated by experiments previously, apart from the stoichiometry studied here. As shown in Table 5.3, for $La_{0.6}Sr_{0.4}Co_xFe_yO_{3-\delta}$, with increasing of Fe-concentration in the B-site, the value α_l decreases. It is reasonable that in the present experimental findings, the value α_l of $La_{0.5}Sr_{0.5}Co_{0.25}Fe_{0.75}O_3$ is about $17*10^{-6}$ K^{-1}, which is smaller than the value α_l of $La_{0.5}Sr_{0.5}CoO_{3-\delta}$ ($21.37*10^{-6}$ K^{-1}) and larger than the value α_l of $La_{0.5}Sr_{0.5}FeO_{3-\delta}$ ($14*10^{-6}$ K^{-1}).

Table 5.3: Comparison of α_l between the literatures and this work.

Composition	α_l (*10^{-6} K^{-1})	T range	Source
$La_{0.6}Sr_{0.4}CoO_{3-\delta}$	15.80	298 K – 723 K	[45]
$La_{0.6}Sr_{0.4}Co_{0.2}Fe_{0.8}O_{3-\delta}$	14.92	303 K – 973 K	[44]
$La_{0.6}Sr_{0.4}FeO_{3-\delta}$	13.40	303 K – 873 K	[26]
$La_{0.5}Sr_{0.5}CoO_{3-\delta}$	21.37	298 K – 923 K	[104]
$La_{0.5}Sr_{0.5}Co_{0.8}Fe_{0.2}O_{3-\delta}$	20.62	298 K – 923 K	[104]
$La_{0.5}Sr_{0.5}Co_{0.25}Fe_{0.75}O_{3-\delta}$	17.37	300 K – 670 K	this work
$La_{0.5}Sr_{0.5}FeO_{3-\delta}$	14.00	303 K – 473 K	[26]

5.3.3.2 Volumetric thermal expansion

After phonon calculations, the Helmholtz free energy of LSCF55 as function of volume at temperatures from 0 K to 700 K (Fig. 5.5, (a) is for GGA exchange-correlation and (b) is for LDA exchange correlation) is obtained and depicted by blue solid squares. At each temperature, the volume dependent Helmholtz free energy is fitted by the solid curves (EOS). Crosses mark the energy minima at each temperature and the connecting line simultaneously shows the temperature dependent equilibrium volumes, from which the volumetric thermal expansion is extracted.

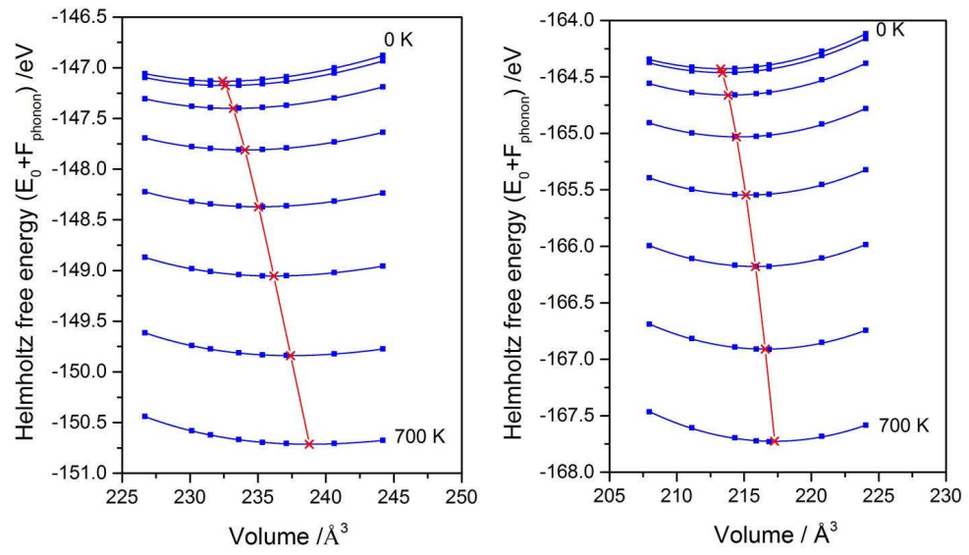

(a) GGA (b) LDA

Figure 5.5: Volume dependent Helmholtz free energy of LSCF55.

The temperature dependent volume expansion of LSCF55 from the first principle phonons calculations combined with the QHA is presented in Fig. 5.6 in comparison with the results from HT-XRD and the estimation based on the measurement of the LSCF55 bar specimen. The volumetric thermal expansion coefficients (α_V) of LSCF55 from both calculation and HT-XRD are found by the slope of the linear fits to the data in

the given temperature intervals (Fig. 5.6), giving $\alpha_{V,GGA} = 50.34 * 10^{-6}\ K^{-1}$, $\alpha_{V,LDA} = 33.34 * 10^{-6}\ K^{-1}$ and $\alpha_{V,HT-XRD} = 43.17 * 10^{-6}\ K^{-1}$. Under the isotropy assumption, the value α_V of the LSCF55 bar specimen can be estimated as $\alpha_{V,isotropic} = 3 * \alpha_{l,bar\ specimen} = 52.11 * 10^{-6}\ K^{-1}$. All the results in this work are summarized and compared in the Table 5.4.

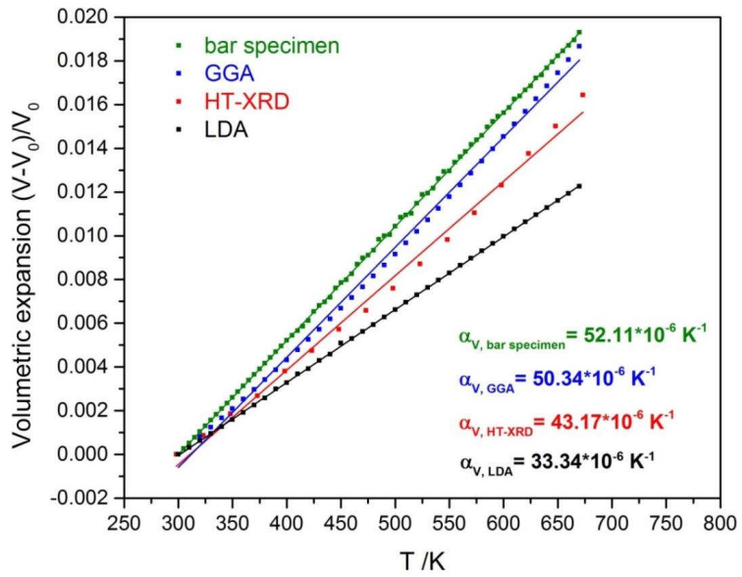

Figure 5.6: Volumetric thermal expansion of LSCF55 with V_0=V_{300K} and in the temperature range from 300 K to 670 K.

Table 5.4: Summary of the experimental and the calculated results.

Method	α_V (*10^{-6} K^{-1})	α_l (*10^{-6} K^{-1})
HT-XRD	43.17	a_{hex}: 10.89
		c_{hex}: 21.18
Measurement by thermo-mechanical analyzer of bar specimen	52.11	17.37
First principles phonon calculations + QHA	GGA: 50.34	
	LDA: 33.34	

The calculated value $\alpha_{V,GGA}$ is significantly larger than $\alpha_{V,LDA}$, and the GGA result is closer to the experimental values. The differences between the calculated $\alpha_{V,GGA}$ and measured $\alpha_{V,HT-XRD}$ and estimated $\alpha_{V,bar\ specimen}$ may come from the following aspects: i) The enforced simplification of equal expansion in all directions reduces the computational effort but excludes anisotropy effects, still leading to a reasonably good prediction for the volumetric thermal expansion. ii) The small amount (~6 wt.%) of secondary phases in the LSCF55 powder may influence the measured value α_l and the estimated value α_V for the bar specimen. iii) In the calculation, the generalized gradient approximation (GGA) method was used. The system LSCF55 contains transition metal, Co and Fe. Therefore, by using GGA method, the LSCF55 system may suffer from the self-interaction errors and get an overestimated ground-state energy, which could influence the calculated value α_V. However, according to Mastrikov et al. [105], who focused on the oxygen vacancy formation and migration in the LSCF system, the possible GGA inaccuracies may cancel. The GGA method in their calculations reliably reproduced the basic structural and electronic properties of both $Ba_{1-x}Sr_xCo_{1-y}Fe_yO_{3-\delta}$ and $La_{1-x}Sr_xCo_{1-y}Fe_yO_{3-\delta}$ related compounds. In future work, the GGA+U approach shall be performed to see how the calculated value α_V changes. iv) The other structures 1, 3 and 4 may contribute differently in the thermal expansion at elevated temperature. Also e.g. electronic excitation and anharmonicities can contribute at higher temperatures. v) In the calculation, the oxygen stoichiometric composition ($\delta=0$) $La_{0.5}Sr_{0.5}Co_{0.25}Fe_{0.75}O_3$ was considered, however, in the real case the oxygen-deficiency ($La_{0.5}Sr_{0.5}Co_{0.25}Fe_{0.75}O_{3-\delta}$, $\delta>0$) may influence the value.

5.4 Conclusion

In chapter 5, the thermal expansion of LSCF55 at finite temperatures was studied by first principles phonon calculations combined with the quasi-harmonic approximation (QHA). Calculations with both GGA and LDA exchange-correlations were performed. GGA gave a better prediction for the LSCF55 structure and LDA. In the frame work of the QHA, the volumetric expansion coefficient of LSCF55 was calculated as $\alpha_{V,GGA} = 50.34 * 10^{-6}\, K^{-1}$. For comparison, the lattice and volume expansions of LSCF55 grains were measured by HT-XRD and the linear expansion of an LSCF55 bar specimen was measured by a thermo-mechanical analyzer. The results of HT-XRD indicated that the thermal expansions of rhombohedral LSCF55 ($\alpha_{a,hex} = 10.89 * 10^{-6}\, K^{-1}$ and $\alpha_{c,hex} = 21.18 * 10^{-6}\, K^{-1}$) was anisotropic and the volumetric expansion coefficient of rhombohedral LSCF55 was $\alpha_{V,HT-XRD} = 43.17 * 10^{-6}\, K^{-1}$. The linear expansion coefficient of the LSCF55 bar specimen was measured to be $\alpha_{l,bar\ specimen} = 17.37 * 10^{-6}\, K^{-1}$. The value $\alpha_{V,bar\ specimen}$ of the LSCF55 bar specimen was $\alpha_{V,bar\ specimen} = 52.11 * 10^{-6}\, K^{-1}$. A good agreement between the calculated and measured values of α_V was obtained. Hence, the first principles phonon calculations combined with the QHA are a potential method to predict the volumetric expansion of LSCF55 as well as for other LSCF compositions.

6. Summary

The present thesis is focused on studying the degradation issues of the LSCF cathode in SOFCs and consists of two research topics: i) studying the Sr-related degradation issues in SOFCs and measuring ZrO_2 activity in 8mol-%Y_2O_3-ZrO_2 electrolyte; ii) determining the thermal expansion coefficient of $La_{0.5}Sr_{0.5}Co_{0.25}Fe_{0.75}O_3$ by first principles phonon calculations combined with the quasi-harmonic approximation.

During the operation of SOFCs, the Cr_2O_3-containing scale forms on the ferritic interconnect (e.g. Crofer® 22 APU), which results in the evaporation of gaseous Cr species. CrO_3 and $CrO_2(OH)_2$ is the dominant gaseous Cr species in dry air and humid air, respectively. $pCrO_3$ shows a stronger temperature dependence than $pCrO_2(OH)_2$. According to the thermodynamic calculations, to minimize Cr species evaporation, dry air is optimal as cathode gas and a reduced operation temperature is preferred. Sr is a reactive element in (La,Sr)(Co,Fe)$O_{3-\delta}$ (LSCF) cathode. It tends to diffuse out from the LSCF cathode and enrich at the LSCF cathode surface, becoming a reaction partner for the evaporated Cr species and leading to the Cr poisoning of the LSCF cathode. By considering dry air as the cathode gas, CrO_3 is the dominant gaseous Cr species. Depending on different pO_2, $pCrO_3$ and temperature, the reaction products between segregated SrO(s) and CrO_3(g) could either be $SrCrO_4$, $SrCrO_3$, $Sr_3Cr_2O_8$ or Sr_2CrO_4. Both thermodynamic calculations and experiments confirm that normally the Cr poisoning product is $SrCrO_4$ and is always found on the top of the cathode surface. Sometimes, due to the drops of local pO_2 in the cathode, the Sr-Cr-O could also form at the LSCF/GDC interface. Besides as a Cr getter, according to the thermodynamic calculations and experiments, by presence of humidity in the air, volatile Sr species (mainly $Sr(OH)_2$) can be formed, which could be in the same order of magnitude as

$pCrO_2(OH)_2$. $pSr(OH)_2$ strongly depends on temperature and SrO activity in the LSCF cathode. SrO segregation and higher temperature facilitate pronounced $Sr(OH)_2$ evaporation. During the long-term operation of SOFCs, the volatile $Sr(OH)_2$ may react with ZrO_2-based electrolytes and form ionic insulating $SrZrO_3$ precipitates. To minimize the influence of volatile Sr species on the performance of SOFC stacks, dry air is optimal as cathode gas. A dense GDC diffusion barrier layer is preferred between the cathode and electrolyte, as it can block volatile Sr species diffusion to the electrolyte. Additionally, an appropriate grain size of ZrO_2-based electrolyte could also contribute to hindering the reaction with gaseous Sr species.

The reaction between the volatile $Sr(OH)_2$ and ZrO_2-based electrolytes depends on the ZrO_2 activity ($aZrO_2$) in the ZrO_2-based electrolytes. As an example, the $aZrO_2$ in 8mol-%Y_2O_3-ZrO_2 (8YSZ) was measured by Knudsen Effusion Mass Spectrometry (KEMS). The measurements were carried out in temperature range from 1900 °C to 2200 °C. The obtained $aZrO_2$ showed no temperature dependence, which was around 0.85. Therefore, the $aZrO_2$ in 8YSZ at SOFC operating temperature (between 700 °C and 900 °C) was estimated as 0.85. A high ZrO_2 activity in 8YSZ facilitates the reaction between volatile $Sr(OH)_2$ and 8YSZ from a thermodynamic point of view.

Besides Sr-related degradation issues of the LSCF cathode, the mechanical stability of the LSCF cathode also influences the life time of SOFCs. The planar designed SOFC has a configuration of layered morphological structure, and therefore the thermal expansion behaviors of different layers are significant for structure design. The thermal expansion coefficients of LSCF with different compositions have been widely measured experimentally in the literatures. In this thesis, the first principles phonon calculations combined with quasi-harmonic approximation (QHA) was used to reliably predict the thermal expansion of $La_{0.5}Sr_{0.5}Co_{0.25}Fe_{0.75}O_3$ (LSCF55). Both GGA and LDA exchange-correlations were performed. GGA gave a better prediction than LDA, yielding the volumetric expansion coefficient of LSCF55 as $\alpha_{V,GGA} = 50.34 * 10^{-6}\, K^{-1}$. For comparison, the lattice and volume expansions of an LSCF55 grain were measured by HT-XRD and the linear expansion of an LSCF55 bar specimen was measured by a

thermo-mechanical analyzer. The results of HT-XRD indicated that the thermal expansion of rhombohedral LSCF55 ($\alpha_{a,hex} = 10.89 * 10^{-6}\ K^{-1}$ and $\alpha_{c,hex} = 21.18 * 10^{-6}\ K^{-1}$) was anisotropic and the volumetric expansion coefficient of rhombohedral LSCF55 was $\alpha_{V,HT-XRD} = 43.17 * 10^{-6}\ K^{-1}$. The linear expansion coefficient of the LSCF55 bar specimen was measured to be $\alpha_{l,bar\ specimen} = 17.37 * 10^{-6}\ K^{-1}$. The value $\alpha_{V,bar\ specimen}$ of the LSCF55 bar specimen was $\alpha_{V,bar\ specimen} = 52.11 * 10^{-6}\ K^{-1}$. A good agreement between the calculated and measured values for α_V was obtained. Hence, the first principles phonon calculations combined with the QHA is a potential method to predict the volumetric expansion of LSCF55 as well as for other LSCF compositions. Additionally, this method can also be used to predict thermodynamic properties of LSCF cathodes.

Bibliography

[1] B. Emonts, L. Blum, T. Grube, W. Lehnert, J. Mergel, M. Müller and R. Peters, Chap. 1 page 4 in Fuel Cell Science and Engineering Vol.1, edited by D. Stolten and B. Emonts, Wiley-VCH verlag&Co. KGaA, Boschstr.12, 69469 Weinheim, Germany, 2012.

[2] L. Blum, W. A. Meulenberg, H. Nabielek and R. Steinberger-Wilckens, Worldwide SOFC Technology Overview and Benchmark, International Journal of Applied Ceramic Technology **2**[6] 482–492, 2005.

[3] From Website: http://www.fz-juelich.de/portal/EN/Research/EnergyEnvironment/Fuelcells/SOFC/_node.html.

[4] W. J. Quadakkers, J. Piron-Abellan, V. Shemet, L. Singheiser, Metallic interconnectors for solid oxide fuel cells – a review, Materials at High Temperatures **20**[2] 115-127, 2003.

[5] E. Konysheva, H. Penkalla, E. Wessel, J. Mertens, U. Seeling, L. Singheiser and K. Hilpert, Chromium poisoning of perovaskite cathodes by ODS alloy Cr5Fe1Y2O3 and high chromium ferritic steel Crofer22APU, Journal of the Electrochemical Society **153**[4] A765-A773, 2006.

[6] L. Blum, L.G.J. de Haart, J. Malzbender, N. H. Menzler, J. Remmel and R. Steinberger-Wilckens, Recent results in Jülich solid oxide fuel cell technology development, Journal of Power Sources **241** 477-485, 2013.

[7] S. P. Jiang, S. Zhang and Y. D. Zhen, Deposition of Cr species at (La,Sr)(Co,Fe)O_3 cathodes, Journal of the Electrochemical Society **153** A127-A134, 2006.

[8] M. Stanislowski, E. Wessel, K. Hilpert, T. Markus and L. Singheiser, Chromium vaporization from high-temperature alloys I. chromia-forming steels and the influence of outer oxide layers, Journal of the Electrochemical Society **154** A295-A306, 2007.

[9] R. Trebbels, T. Markus, L. Singheiser, Investigation of chromium vaporization from interconnector steels with spinel coatings, Journal of Fuel Cell Science and Technology **7** 011013-011018, 2009.

[10] K. Hilpert, D. Das, M. Miller, D. H. Peck and R. Weiß, Chromium vapor species over solid oxide fuel cell interconnect materials and their potential for degradation processes, Journal of the Electrochemical Society **143** 3642-3647, 1996.

[11] X. Chen, P. Y. Hou, C. P. Jacobson, S. J. Viscao and L. C. De Jonghe, Protective coating on stainless steel interconnects for SOFCs: oxidation kinetics and electrical properties, Solid State Ionics **176** 425-433, 2005.

[12] Z. G. Yang, G. G. Xia, X. H. Li and J. W. Stevenson, $(Mn,Co)_3O_4$ spinel coatings on ferritic stainless steels for SOFC interconnect applications, International Journal of Hydrogen Energy **32** 3648-3654, 2007.

[13] N. Grünwald, D. Sebold, Y. J. Sohn, N. H. Menzler and R. Vaßen, Self-healing atmospheric plasma sprayed $Mn_{1.0}Co_{1.9}Fe_{0.1}O_4$ protective interconnector coatings for solid oxide fuel cells, Journal of Power Sources **363** 185-192, 2017.

[14] T. Ishihara, N. M. Sammes and O. Yamamoto, Electrolyte, Chap.4 in book 'High Temperature and Solid Oxide Fuel Cells, fundamental, design and application', edited by S. C. Singhal and K. Kendal, Elsevier, the Boulevard, Langford Lane, Kidlington, Oxford 0X5 1GB, UK, 2003.

[15] J. B. Goodenough, Ceramic solid electrolytes, Solid State Ionics **94** 17-25, 1997.

[16] P. K. Schelling, S. R. Phillpot and D. Wolf, Mechanism of the cubic-to-tetragonal phase transition in zirconia and ytttia-stabilized zirconia by molecular-dynamics simulation, Journal of the American Ceramic Society **84**[7] 1609-1919, 2001.

[17] N. Mahato, A. Banerjee, A. Gupta, S. Omar and K. Balani, Process in material selection for solid oxide fuel cell technology: A review, Process in Material Science **72** 141-337, 2015.

[18] Z. Shao and M. O. Tadé, Anodes for IT-SOFCs, chap. 4 in book Intermediate-temperature Solid Oxide Fuel Cells, materials and applications, edited by Z. Shao and M. O. Tadé, Springer-Verlag Berlin Heidelberg, 2016.

[19] S. P. Jiang and S. H. Chan, A review of anode material development in solid oxide fuel cells, Journal of Materials Science **39** 4405-4439, 2004.

[20] B. Shri Prakash, S. Senthil Kumar and S. T. Aruna, Properties and development of Ni/YSZ as an anode material in solid oxide fuel cell: A review, Renewable and Sustainable Energy Reviews **36** 149-179, 2014.

[21] D. W. Dees and T. D. Claar, Conductivity of porous Ni/ZrO_2-Y_2O_3 cermet, Journal of the Electrochemical Society, **134** 2141-2146, 1987.

[22] S. J. Skinner, Recent advances in perovskite-type materials for solid oxide fuel cell cathodes, International Journal of Inorganic Materials, **3** 113-121, 2011.

[23] C. W. Sun, R. Hui and J. Roller, Cathode materials for solid oxide fuel cells: a review, Journal of Solid State Electrochemistry, **14** 1125-1144, 2010.

[24] K. A. Müller, W. Berlinger and F. Waldner, Characteristic structural phase transition in perovskite-type compounds, Physical Review Letter **21**[12] 814-817, 1968.

[25] K. S. Alexandrov, B. V. Besnosikov and L. A. Posdnjakova, Successive phase transition in perovskites II. Structure of distorted phases, Ferroelectrics **12** 197-198, 1976.

[26] A. Fossdal, M. Menon, I. Waernhus, K. Wiik, M. A. Einarsrud and T. Grande, Crystal Structure and Thermal Expansion of La1−*x*Sr*x*FeO3−δ Materials, Journal of the American Ceramic Society **87**[10] 1952–1958, 2004.

[27] B. Huang, Thermo-Mechanical Properties of Mixed Ion-Electron Conducting Membrane Materials, page 11, PhD thesis, RWTH Aachen, 2010.

[28] S. P. Jiang, Issues on development of (Ls,Sr)MnO_3 cathode for solid oxide fuel cells, Journal of Power Sources **124** 390-402, 2003.

[29] J. M. Palph, A. C. Schoeler and M. Krumpelt, Materials for lower temperature solid oxide fuel cells, Journal of Materials Science **36** 1161-1172, 2001.

[30] J. Mizusaki, Y. Yonemura, H. Kamata, K. Ohyama, N. Mori, H. Takai, H. Tagawa, M. Dokiya, K. Naraya, T. Sasamoto, H. Inaba and T. Hashimoto, Electronic conductivity, Seebeck coefficient, defect and electronic structure of nonstoichiometric $La_{1-x}Sr_xMnO_3$, Solid State Ionics 132 167-180, 2000.

[31] G. Stochniol, E. Syskakis and A. Naoumidis, Chemical compatibility between strontium-doped lanthanum manganite and yttria-stabilized zriconia, Journal of the American Ceramic Society **78**[4] 929-932, 1995.

[32] M. J. Jørgensen and M. Mogensen, Impedance of solid oxide fuel cell LSM/YSZ composite cathodes, Journal of the Electrochemical Society **148**[5] A433-A442, 2001.

[33] S. B. Adler, J. A. Lane and B. C. Steele, Electrode kinetics of porous mixed-conducting oxygen electrodes, Journal of the Electrochemical Society **143** 3554-3564, 1996.

[34] S. P. Jiang, A comparison of O_2 reduction reactions on porous $(La,Sr)MnO_3$ and $(La,Sr)(Co,Fe)O_3$ electrodes, Solid State Ionics **146** 1-22, 2002.

[35] A. Esquirol, N. P. Brandon, J. A. Kilner, M. Mogensen, Electrochemical characterization of $La_{0.6}Sr_{0.4}Co_{0.2}Fe_{0.8}O_3$ cathodes for intermediate-temperature SOFCs, Journal of the Electrochemical Society **151** A1847-A1855, 2004.

[36] E. N. Armstrong, K. L. Duncan, D. J. Oh, J. F. Wayver and E. D. Wachsman, Determination of surface exchange coefficients of LSM, LSCF, YSZ, GDC constituent materials in composite SOFC cathodes, Journal of the Electrochemical Society **158** B492-B499, 2011.

[37] L. W. Tai, M. M. Nasrallah, H. U. Anderson, D. M. Sparlin and S. R. Sehlin, Structure and electrical properties of $La_{1-x}Sr_xCo_{1-y}Fe_yO_3$. Part 2. The system $La_{1-x}Sr_xCo_{0.2}Fe_{0.8}O_3$, Solid State Ionics **76** 273-283, 1995.

[38] S. Kanae, Y. Toyofuku, T. Kawabata, Y. Inoue, T. Daio, J. Matsuda, J. T. Chou, Y. Shiratori, S. Taniguchi and K. Sasaki, Microstructural Characterization of $SrZrO_3$ formation and the influence to SOFC performance, ECS Transactions **68** 2463-2470, 2015.

[39] R. Kiebach, W. W. Zhang, W. Zhang W, M. Chen, K. Norrman, H. J. Wang, J. R. Bowen, R. Barfod and P. V. Hendriksen, Stability of $La_{0.6}Sr_{0.4}Co_{0.2}Fe_{0.8}O_3/Ce_{0.9}Gd_{0.1}O_2$ cathodes during sintering and solid oxide fuel cell operation, Journal of Power Sources **283** 151-161, 2015.

[40] R Knibbe, J Hjelm, M. Menon, N. Pryds, M. Søgaard, H. L. Wang and K. Neufeld, Cathode-electrolyte interfaces with CGO barrier layers in SOFC, Journal of the American Ceramic Society **93** 2877-2883, 2010.

[41] N. Jordan, W. Assenmacher, S. Uhlenbruck, V. A. C. Haanappel, H. P. Buchkremer, D. Stöver and W. Mader, $Ce_{0.8}Gd_{0.2}O_{2-\delta}$ protecting layers manufactured by physical vapor deposition for IT-SOFC, Solid State Ionics **179** 919-923, 2008.

[42] A. Mai, V. A. C. Haanappel, F. Tietz and D. Stöver, Ferrite-based perovskite as cathode materials for anode-supported solid oxide fuel cell Part II. Influence of CGO interlager, Solid State Ionics **177** 2103-2107, 2006.

[43] V. Haaappel, Advances in solid oxide fuel cell development between 1995 and 2010 at Forschungszentrum Jülich GmbH, Germany, Chap.9 page 260 in Fuel Cell Science and Engineering Vol.1, edited by D. Stolten and B. Emonts, Wiley-VCH verlag&Co. KGaA, Boschstr.12, 69469 Weinheim, Germany, 2012.

[44] C. Mongkolkachit and S. Wanakitti, Characterization of $(La,Sr)(Co,Fe)O_{3-\delta}$ ferrite-based cathodes for intermediate-temperature SOFCs, Journal of Metals, Materials and Minerals **18**[2] 33-36, 2008.

[45] X. Chen, J. Yu and S. B. Adler, Thermal and chemical expansion of Sr-doped lanthanum cobalt oxide ($La_{1-x}Sr_xCoO_{3-\delta}$), Chemistry of Materials **17** 4537-4546, 2005.

[46] V. V. Kharton, F. M. Figueiredo, L. Navarro, E. N. Naumovich, A. V. Kovalevsky, A. A. Yaremchenko, A. P. Viskup, A.Carneiro, F. M. B. Marques and J. R. Frade, Ceria-based materials for solid oxide fuel cells, Journal of Materials Science **36** 1105-1117, 2001.

[47] H. Yokokawa, H. Tu, B. Iwanschitz and A. Mai, Fundamental mechanisms limiting solid oxide fuel cell durability, Journal of Power Sources **182** 400-412, 2008.

[48] S. P. Simner, M. D: Anderson, M. H. Engelhard and J. W. Stevenson, Degradation Mechanisms of La-Sr-Co-Fe-O3 SOFC cathode, Electrochemical and Solid-State Letters, **9**[10] A478-A481, 2006.

[49] Z. H. Pan, Q. L. Liu, L. Zhang, X. W. Zhang and S. H. Chan, Effect of Sr surface segregation of $La_{0.6}Sr_{0.4}Co_{0.2}Fe_{0.8}O_{3-\delta}$ electrode on its electrochemical performance in SOC, Journal of the Electrochemical Society **162**[12] F1316-F1323, 2015.

[50] D. Oh, D. Gostovic and E. D. Wachsman, Mechanism of $La_{0.6}Sr_{0.4}Co_{0.2}Fe_{0.8}O_{3-\delta}$ cathode degradation, Journal of Materials Research **27**[15] 1992-1999, 2012.

[51] L. Zhao, J. Drennan, C. Kong, S. Amarasinghe and S. P. Jiang, Insight into surface segregation and chromium deposition on $La_{0.6}Sr_{0.4}Co_{0.2}Fe_{0.8}O_{3-\delta}$ cathode of solid oxide fuel cells, Journal of Materials Chemistry A **2** 11114-11123, 2014.

[52] L. Zhao, J. Zhang, T. Becker and S. P. Jiang, Raman spectroscopy study of chromium deposition on $La_{0.6}Sr_{0.4}Co_{0.2}Fe_{0.8}O_{3-\delta}$ cathode of solid oxide fuel cells, Journal of the Electrochemical Society **161**[6] F687-F693, 2014.

[53] C. C. Wang, T. Becker, K. Chen, L. Zhao, B. Wei and S. P. Jiang, Effect of temperature on the chromium deposition and poisoning of $La_{0.6}Sr_{0.4}Co_{0.2}Fe_{0.8}O_{3-\delta}$ cathode of solid oxide fuel cells, Electrochimica Acta **139** 173-179, 2014.

[54] N. H. Menzler, P. Batfalsky, S. M. Groß, V. Shemet, F. Tietz, Post-Test Characterization of an SOFC short stack after 17000 hours of steady operation, ECS Transactions **35**[1] 195-206, 2011.

[55] N. H. Menzler, D. Sebold, E. Wessel, Interaction of $La_{0.58}Sr_{0.4}Co_{0.2}Fe_{0.8}O_{3-\delta}$ cathode with volatile Cr in a stack test – Scanning electron microscopy and transmission electron microscopy investigations, Journal of Power Sources **254** 148-152, 2014.

[56] A. Mai, M. Becker, W. Assenmacher, F. Tietz, D. Hathiramani, E. Ivers-Tiffee, D. Stöver and W. Mader, Time-dependent performance of mixed-conducting SOFC cathodes, Solid State Ionics **177** 1965-1968, 2006.

[57] S. Uhlenbruck, T. Moskalewicz, N. Jordan, H. J. Penkalla and H. P. Buchkremer, Element inter diffusion at electrolyte-cathode interfaces in ceramic high-temperature fuel cells, Solid State Ionics **180** 418-423, 2009.

[58] R. Knibbe, J. Hjelm, M. Menon, N. Pryds, M. Søgaard, H. J. Wang and K. Neufeld, Cathode-electrolyte interfaces with CGO barrier layers in SOFC, Journal of the American Ceramic Society **93**[9] 2877-2883, 2010.

[59] F. F. Wang, M. Nishi, M. E. Brito, H. Kishimoto, K. Yamaji, H. Yokokawa and T. Horita, Sr and Zr diffusion in LSCF/10GDC/8YSZ triplets for solid oxide fuel cells (SOFCs), Journal of Power Sources **258** 281-289, 2014.

[60] J. DeVero, K. Develos-Bagarinao, D. H. Cho, H. Kishimoto, K. Yamaji and H. Yokokawa, Effect of LSCF microstructure on GDC interlayer stability and cation diffusion in porous and dense LSCF/GDC/YSZ triplets, ECS Transaction 68 1943-1952, 2015.

[61] N. Sakai, H. Kishimoto, K. Yamaji, T. Horita, M. E. Brito and H. Yokokawa, Interface stability of perovskite cathodes and rare-earth doped ceria interlayer in SOFCs, Journal of the Electrochemical Society **154** B1331-1337, 2007.

[62] F. Tietz, A. Mai and D. Stöver, From powder properties to full cell performance – A holistic approach for SOFC cathode development, Solid State Ionics **179** 1509-1515, 2008.

[63] Z. Lu, S. Darvish, J. Hardy, J. Templeton, J. Stevenson and Y. Zhong, $SrZrO_3$ formation at the interlayer/electrolyte interface during $(La_{1-x}Sr_x)_{1-\delta}Co_{1-y}Fe_yO_3$ cathode sintering, Journal of the Electrochemical Society **164** F3097-F3103, 2017.

[64] J. Malzbender, T. Wakui and R. W. Steinbrech, Curvature of planar solid oxide fuel cells during sealing and cooling of stacks, Fuel Cells **6**[2] 123-129, 2006.

[65] L. Blum, An analysis of contact problems in solid oxide fuel cell stacks arising from differences in thermal expansion coefficients, Eletrochimica Acta **223** 100-108, 2017.

[66] R. Steinberger-Wilckens, I. C. Vinke, L. Blum, J. Remmel, F. Tietz, W. J. Quadakkers, Progress in SOFC stack development at Forschungszetrum Jülich, Proceeding of 6th European SOFC Forum, Luzern/CH, 2004, pp.11-19.

[67] L. Blum, S. M. Groß, J. Malzbender, U. Pabst, M. Peksen, R. Peters, I. C. Vinke, Investigation of solid oxide fuel cell sealing behavior under stack relevant conditions at Forschungszentrum jülich, Journal of Power Sources **196** 7175-7181, 2011.

[68] A. Petric, P. Huang and F. Tietz, Evalulation of La-Sr-Co-Fe-O perovskites for solid oxide fuel cells and gas separation memebranes, Solid State Ionics **135** 719-725, 2000.

[69] H. Ullmann, N. Trofimenko, F. Tietz, D. Stöver, A. Ahmad-Khanlou, Correlation between thermal expansion and oxide ion transport in mixed conducting perovskite-type oxide for SOFC cathode, Solid State Ionics **138** 79-90, 2000.

[70] F. Schulze-Küppers, S. Baumann, F. Tietz, H. J. M. Mouwmeester, M. A. Meulenberg, Towards the fabrication of $La_{0.98-x}Sr_xCo_{0.2}Fe_{0.8}O_{3-\delta}$ perovskite-type oxygen transport membranes, Journal of the European Ceramic Society **34** 3741-3748, 2014.

[71] F. Tietz, I. A. Raj, M. Zahid, D. Stöver, Electrical conductivity and thermal expansion of $La_{0.8}Sr_{0.2}(Mn,Fe,Co)O_{3-\delta}$) perovskites, Solid State Ionics **177** 1753-1756, 2006.

[72] J. L. Burgot, chap.9 ‘Definitions of an activity’, in book ‘The Notion of Activity in Chemistry’, pp.84, Springer International Publishing Switzerland, 2017.

[73] C. W. Bale, E. Bélisle, P. Chartrand, S. A. Decterov, G. Eriksson, A. E. Gheribi, K. Kack, I. H. Jung, Y. B. Kang, J. Melançon, A. D. Pelton, S. Petersen, C. Robelin, J. Sangster, P. Pencer, M. A. Van Ende, FactSage Thermochemical Software and Databases, 2010-2016, Calphad **54** 35-531 2016.

[74] T. Markus, Potential of Knudsen Effusion Mass Spectrometry (KEMS) for Thermal Chemical Studies in Materials Science, 224th ECS Meeting, 2013.

[75] K. Hilpert, Potential of mass spectrometry for the analysis of inorganic high temperature vapors, Fresenius' Journal of Analytical Chemistry, **370**[5] 471-478, 2001.

[76] G. Kresse, M. Marsman, J. Furthmüller, Vasp the Guide. Univ. Vienna: Vienna, Austria 2016.

[77] V. L. Deringer, R. P. Stoffel and R. Dronskowski, Vibrational and thermodynamic properties of GeSe in the quasiharmonic approximation, Physical Review B **89** 094303 1-9, 2014.

[78] R. Wang, S. Wang and X. Wu, Ab initio study of the thermodynamic properties of rare-earth-magnesium intermetallics MgRE (RE=Y, Dy, Pr, Tb), Physica Scripta **83** 065707 1-7, 2011.

[79] A. Togo and I. Tanaka, First principles phonon calculations in materials science, Scripta Materialia **108** 1-5, 2015.

[80] M. Born and R. Oppenheimer, Zur Quantentheorie der Molekeln, Annalen der Physik, **389** [20] 457-484, 1927.

[81] P. Hohenberg and W. Kohn, Inhomogeneous electron gas, Physical Review **136** [3B] B864–B871, 1964.

[82] W. Kohn and L. J. Sham, Self-consistent equation including exchange and correlation effects, Physical Review **140** [4A] A1133-1138, 1965.

[83] J. P. Perdew, K. Burke and M. Ernzerhof, Generalized Gradient Approximation made simple, Physical Review Letter **77**[18] 3865-3868, 1996.

[84] Appendix A: Electronic structure calculations: the density functional theory, page 326 in book 'Introduction to Graphene-Based Nanomaterials, From Electronic Structure to Quantum Transport' edited by L. E. F. Foa Torres, S. Roche and J. C. Charlier, Cambridge University Press, 2014.

[85] H. J. Monkhorst and J. D. Pack, Special points for Brillouin-zone integrations, Physical Review B **13** 5188-5192, 1976.

[86] Website: https://commons.wikimedia.org/wiki/File:Sketch_Pseudopotentials.png

[87] P. E. Blöchl, Projector augmented-wave method, Physical Review B **50** 17953-17979, 1994.

[88] C. Gindorf, L. Singheiser, K. Hilpert, Vaporization of chromia in humid air, Journal of Physics and Chemistry of Solids **66** 384-387, 2005.

[89] K. Hilpert, Erratum to "Vaporization of chromia in humid air" [Journal of Physics and Chemistry of Solids 66 (2–4), (2005) 384–387] by C. Gindorf, L. Singheiser and K. Hilpert. Journal of Physics and Chemistry of Solids **66** 1851, 2005.

[90] B. B. Ebbinghaus, Thermodynamics of gas phase chromium species: The chromium oxides, the chromium oxy-hydroxides, and volatility calculations in waste incineration processes, Combustion and Flame **93** 119-137, 1993.

[91] M. Stanislowski, Evaporation processes during operation of solid oxide fuel cell, PhD thesis, RWTH Aachen, page 94, 2006.

[92] W. W. Zhang, Investigation of degradation mechanisms of LSCF based SOFC cathodes — by CALPHAD modeling and experiments, PhD thesis, Department of Energy Conversion and Storage, Technical University of Denmark, page 138, 2010.

[93] A. Beez A, X. Y. Yin, N. Menzler, R. Spatschek and M. Bram, Insight into the reaction mechanism of $(La_{0.58}Sr_{0.40})(Co_{0.20}Fe_{0.80})O_{3-\delta}$ cathode with volatile chromium species at high current density in a solid oxide fuel cell stack, Journal of Electrochemical Society **164** F3028-F3034, 2017.

[94] M. Kuhn, Y. Fukuda, S. Hashimoto, K. Sato, K. Yashiro and J. Mizusaki, Oxygen nonstoichiometry and thermo-chemical stability of perovskite type $La_{0.6}Sr_{0.4}Co_{1-y}Fe_yO_{3-\delta}$ (y=0, 0.2, 0.4, 0.5, 0.6, 0.8, 1) materials, Journal of the Electrochemical Society **160** F34-F42, 2013.

[95] S. Kim, H. J. Avila-Paredes, S. Z. Wang, C. T. Chen, R. A. De Souza, M. Martin and Z. A. Munir, On the conduction pathway for protons in nanocrystalline yttria-stabilized zirconia, Physical Chemistry Chemical Physics **11** 3035-3038, 2009.

[96] J. Jiang and J. L. Hertz, Intermediate temperature surface proton conduction on dense YSZ thin films, Journal of Materials Chemistry A **2** 19550-19555, 2014.

[97] M. Takayanagi, S. Furuichi, W. Namiki, T. Tsuchiya, M. Minohara, M. Kobayashi, K. Horiba, H. Kumigashira and T. Higuchi, Proton conduction on YSZ electrolyte thin films prepared by RF Magnetron Sputtering, ECS Transactions **75**[42] 115-120, 2017.

[98] G .V. Belov, V. S. Iorish, V. S. Yungman, Ivtanthermo for windows – database on thermodynamic properties and related software, Calphad: Computer Coupling of Phase Diagrams and Thermochemistry 23 (1999) 173–180.

[99] G. Kresse, D. Joubert, From ultra-soft pseudopotentials to the projector augmented-wave method, Physical Review B **59** 1758-1775, 1999.

[100] P. Vinet, J. H. Rose, J. Ferrante, J. R. Smith, Universal features of the equation of state of solids, Journal of Physics: Condensed Matter **1** 1941-1963, 1989.

[101] M. P. Pechini, Method of preparing lead and alkaline earth titanates and niobates and coating method using the same to form a capacitor, U. S. Patent 3330697, 1967.

[102] X. Wang, Y. Han, X. Song, W. Liu and H. Cui, Phonon spectrum and thermodynamic properties of $LaCoO_3$ based on first-principles theory, Computational Materials Science **136** 191-197, 2017.

[103] R. W. Rice, Evaluation of the porosity dependence of properties, Chapter 2 in Porosity of Ceramics. New York: Marcel Dekker. Inc. 1998, page 44.

[104] Y. Fu, A. Subardi, M. Hsieh and W. Chang, Electrochemical properties of $La_{0.5}Sr_{0.5}Co_{0.8}Mn_{0.2}O_{3-\delta}$ (M=Mn, Fe, Ni, Cu) perovskite cathodes for IT-SOFCs, Journal of the American Ceramic Society **99** 1345-1352, 2016.

[105] Y. A. Mastrikov, R. Merkle, E. A. Kotomin, M. M. Kuklja and J. Maier, Formation and migration of oxygen vacancies in $La_{1-x}Sr_xCo_{1-y}Fe_yO_{3-\delta}$ perovskites: insight from ab initio calculations and comparison with $Ba_{1-x}Sr_xCo_{1-y}Fe_yO_{3-\delta}$, Physical Chemistry Chemical Physics **15** 911-918, 2013

List of Publications

A. Beez, **X. Yin**, N. Menzler, R. Spatschek and M. Bram, Insight into the reaction mechanism of $(La_{0.58}Sr_{0.40})(Co_{0.20}Fe_{0.80})O_{3-d}$ cathode with volatile chromium species at high current density in a solid oxide fuel cell stack, Journal of Electrochemical Society **164**: F3028-F3034, 2017.

X. Yin, L. Bencze, L. Motalov, R. Spatschek and L. Singheiser, Thermodynamic perspectives of Sr-related degradation issues in SOFCs, International Journal of Applied Ceramic Technology **15**:380-390, 2018.

X. Yin, A. Beez, N. Menzler and R. Spatschek, Combined experimental and ab initio based determination of thermal expansion of $La_{0.5}Sr_{0.5}Co_{0.25}Fe_{0.75}O_3$, Journal of the American Ceramic Society 2018;1-8.

N. Grünwald, Y. Sohn, **X. Yin**, N. Menzler, O. Guillon and R. Vaßen, Microstructure and phase evolution of atmospheric plasma sprayed Mn-Co-Fe oxide protection layers for solid oxide fuel cells, submitted for publication.

Schriften des Forschungszentrums Jülich
Reihe Energie & Umwelt / Energy & Environment

Band / Volume 432
Laser Treatment of Silicon Thin-Films for Photovoltaic Applications
C. Maurer (2018), vii, 165 pp
ISBN: 978-3-95806-347-1

Band / Volume 433
Mentalitäten und Verhaltensmuster im Kontext der Energiewende in NRW
K. Schürmann & D. Schumann (Hrsg.) (2018), 236 pp
ISBN: 978-3-95806-349-5

Band / Volume 434
Adhäsionsverhalten von wässrigen Nafion-Lösungen an dispersen Phasengrenzen
A. Schulz (2018), xii, 129 pp
ISBN: 978-3-95806-354-9

Band / Volume 435
Alterungs- und fehlertolerante optimale Betriebsführung eines Direktmethanol-Brennstoffzellensystems
R. Keller (2018), XX, 175 pp
ISBN: 978-3-95806-355-6

Band / Volume 436
Chamber study of biogenic volatile organic compounds: plant emission, oxidation products and their OH reactivity
Y. Zhujun (2018), ix, 139 pp
ISBN: 978-3-95806-356-3

Band / Volume 437
Characterization of High Temperature Polymer Electrolyte Fuel Cells
Y. Rahim (2018), iii, 162 pp
ISBN: 978-3-95806-359-4

Band / Volume 438
Lattice Boltzmann Simulation in Components of Polymer Electrolyte Fuel Cell
J. Yu (2018), ii, 173 pp
ISBN: 978-3-95806-360-0

Band / Volume 439
Quantitative Luminescence Imaging of Solar Cells
V. Huhn (2018), 155 pp
ISBN: 978-3-95806-363-1

Schriften des Forschungszentrums Jülich
Reihe Energie & Umwelt / Energy & Environment

Band / Volume 440
Characterization of Phosphoric Acid Doped Polybenzimidazole Membranes
Y. Lin (2018), II, IV, 140 pp
ISBN: 978-3-95806-364-8

Band / Volume 441
Degradation Study of SOC Stacks with Impedance Spectroscopy
Y. Yan (2018), 135 pp
ISBN: 978-3-95806-367-9

Band / Volume 442
Future Grid Load of the Residential Building Sector
L. Kotzur (2018), xxi, 213 pp
ISBN: 978-3-95806-370-9

Band / Volume 443
Yttriumoxid-Dünnschichten als Tritium-Permeationsbarriere
J. Engels (2018), 252 pp
ISBN: 978-3-95806-371-6

Band / Volume 444
Inverse conditioning of a high resolution integrated terrestrial model at the hillslope scale: the role of input data quality and model structural errors
S. Gebler (2018), xxii, 160 pp
ISBN: 978-3-95806-372-3

Band / Volume 445
Cathode Stability and Processing in Inert Substrate-Supported Solid Oxide Fuel Cells
E. Matte (2018), viii, 178 pp
ISBN: 978-3-95806-373-0

Band / Volume 446
Aging and Degradation Behavior of Electrode Materials in Solid Oxide Fuel Cells (SOFCs)
X. Yin (2018), x, 103 pp
ISBN: 978-3-95806-374-7

Energie & Umwelt / Energy & Environment
Band / Volume 446
ISBN 978-3-95806-374-7

Mitglied der Helmholtz-Gemeinschaft

JÜLICH
Forschungszentrum